Sustainable Energy & Fuels

ROYAL SOCIETY OF CHEMISTRY

REVIEW

View Article Online
View Journal | View Issue

Cite this: *Sustainable Energy Fuels*, 2025, **9**, 3458

UiO-66-NH_2 and its functional nanohybrids: unlocking photocatalytic potential for clean energy and environmental remediation

Nagma Sultana, Priyanka Priyadarshini and Kulamani Parida *

UiO-66-NH_2, an amino-functionalized zirconium-based metal–organic framework, presents great promise as a photocatalyst owing to its superior thermal and chemical stability, tunable structure, and high surface area. More importantly, strategic design and optimization can significantly enhance the photo response range of UiO-66-NH_2 (UNH) and charge carrier separation efficiency. This review aims to offer a comprehensive overview of UiO-66-NH_2 and its hybrid nanomaterials, focusing on their synthesis methods, properties, and photocatalytic applications in environmental remediation and energy production. This article explores the progress made in green and efficient synthesis methods, including solvothermal, microwave-assisted, sonochemical, and mechanochemical methods, which are recognized for their scalability and environmental sustainability. Strategies for enhancing the photocatalytic efficiency of UiO-66-NH_2 hybrid nanomaterials, including heterojunction formation, metal doping, and linker modifications, are explored to improve charge separation, light absorption, and stability. Applications discussed include toxic Cr(VI) reduction, CO_2 photoreduction, dye and antibiotic degradation, and H_2 & O_2 evolution. It also discusses key challenges, such as maintaining stability under operational conditions, enhancing recyclability, and optimizing hybrid systems. Additionally, the review emphasizes the potential of UiO-66-NH_2 as a highly adaptable and promising material, offering valuable perspectives to advance research in photocatalytic applications.

Received 31st January 2025
Accepted 11th May 2025

DOI: 10.1039/d5se00150a

rsc.li/sustainable-energy

1. Introduction

Due to the rapid increase in modernization and industrialization, the challenges of energy depletion and environmental degradation from excessive fossil fuel use have persistently troubled humanity.[1] Mainly, the release of CO_2 and volatile organic compounds by using fossil fuels causes air pollution, in contrast, various organic pollutants like antibiotics, organic dyes, and other metals are the root cause of water pollution, severely damaging the ecological system and human health, leading researchers to pursue renewable, clean energy sources. An advancing technology that can help realize this vision is photocatalysis, which has gained recognition as an environmentally friendly approach thanks to its potential to harness renewable solar energy. For example, atmospheric CO_2 can be transformed into chemicals like methane (CH_4), formic acid (HCOOH), and methanol (CH_3OH) through photocatalytic methods, without adding any further pollution to the environment.[2,3] Additionally, to meet the high energy demands, photocatalytic water splitting for the hydrogen evolution reaction (HER) has been a very effective approach. Essentially, an effective photocatalyst should possess several key characteristics: (i) a high surface area to adsorb reactant molecules and facilitate redox reactions, (ii) strong light absorption along with efficient electron–hole separation across the conduction band (CB) and valence bands (VB), (iii) an appropriate band edge potential, (iv) prolonged exciton (electron–hole) lifespan with minimal recombination, and (v) robust thermal and chemical stability. These attributes of a photocatalyst make it a robust material for diverse applications.[4,5]

There has been exponential growth in the research field in recent years discussing the role of different heterogeneous photocatalysts, but properties like fast charge recombination and low light absorption due to their wide band gaps limit their roles in photocatalysis.[6,7] Among them, MOFs emerge as very effective photocatalysts due to their well-organized framework structure, excellent porosity, and large surface area.[8,9] They are easily tunable, so it is easy to augment the photocatalytic efficiency by modifying their chemical and structural properties.[10,11] Despite these, there are also some limitations like toxicity, lower chemical and water stability, recyclability, poor photocatalytic activity, *etc.*, when used in pure form.[12,13] To overcome the following challenges, various modifications with MOF, like doping, heterojunction/composite formation, defect engineering, photosensitization, *etc.*, have gained a lot of interest more recently.[14–16]

Centre for Nano Science and Nano Technology, S 'O' A (Deemed to be University), Bhubaneswar 751030, Odisha, India. E-mail: kulamaniparida@soauniversity.ac.in; paridakulamani@yahoo.com

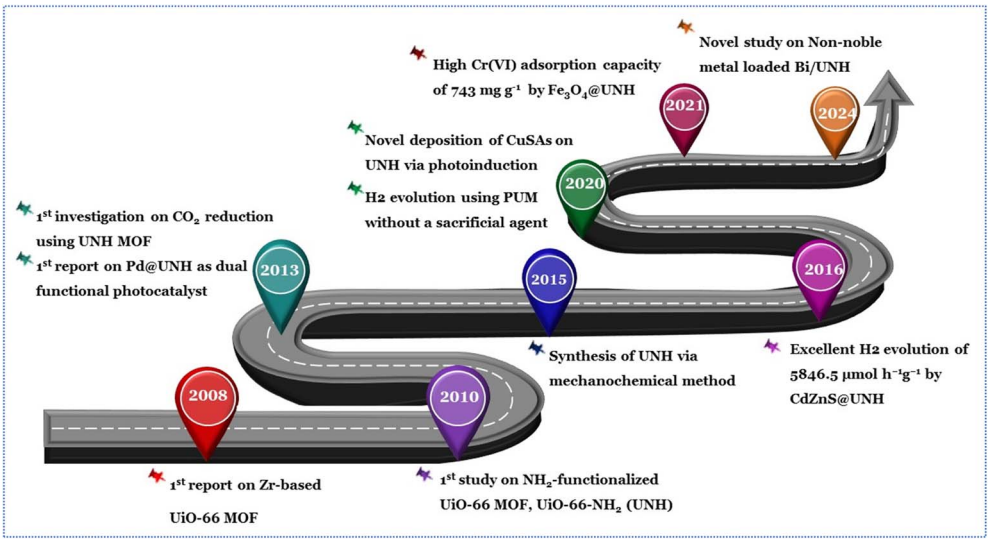

Fig. 1 Timeline of the advancement of UiO-66-NH_2 and its functional hybrid materials in photocatalysis till date.

Among the various types of MOFs, Lillerud's group discovered the UiO-66 MOF with Zr-based metal clusters and terephthalic acids $(H_2BDC)_6$ linkers, and it has gathered a lot of interest in the material science field, especially in the photocatalysis field.[17] UiO-66's higher chemical and thermal stability than other MOFs makes it more useful for various applications. The stronger Zr–O bond can explain thermal stability, and higher chemical stability is due to the high oxygenophilic capability of Zr^{4+}.[18,19] Despite these qualities, UiO-66's photoactivity isn't that commendable compared to other semiconductor materials. Therefore, Silva *et al.* modified the UiO-66 MOF by using the $-NH_2$ group to synthesize UiO-66-NH_2 (UNH) for the H_2 generation process that comprises a Zr-metal cluster and 12 NH_2-H_2BDC as the linker.[20] UiO-66 ($E_g = 3.8$ eV) absorbs light in the UV region, which limits its applications in various fields, whereas UiO-66-NH_2 ($E_g = 2.89$ eV) absorbs light effectively in the visible light spectrum. The $-NH_2$ group is assumed to be accountable for UNH's improved photocatalytic performance. Due to its easy tunable nature, further modifications with different functional metal nodes/linkers or defect engineering can be helpful in enhancing the photocatalytic performance of UNH without majorly changing its structure and stability. Thus, UNH is an incredibly fascinating material with limitless potential for photocatalytic applications.

Until now, most reviews on Zr-based MOFs have focused on synthesis, modification strategies, and various photocatalytic applications.[21,22] Some have centered on the parent UiO-66 structure, while others have explored the synthesis and energy or environmental applications of UiO-66-based composites.[1,18,23] However, UiO-66-NH_2 is often briefly mentioned as a subtopic, lacking detailed analysis of its growing role in photocatalysis. Additionally, to date, no review has systematically explored the UiO-66-NH_2 MOF and its hybrid materials that cover both energy and environmental aspects of photocatalysis. In light of the urgent global need for sustainable energy production and effective environmental remediation solutions, and UiO-66-NH_2's growing relevance as a visible-light-active material with excellent photocatalytic performance, a focused review on this MOF is both timely and necessary. This review fills that gap by offering the first holistic evaluation of UiO-66-NH_2's dual-role in both energy and environmental fields, positioning it as a multifunctional platform to address global energy and environmental challenges. The review begins by discussing the structure–property relationships of UiO-66-NH_2 to establish a foundation for its behavior. It then covers both traditional and emerging green synthesis methods, outlining their benefits and drawbacks, followed by key applications including H_2 & O_2 evolution, CO_2 and Cr(VI) reduction, and degradation of dyes and antibiotics. Finally, the review outlines the key challenges and future research directions in the field, aiming to guide the

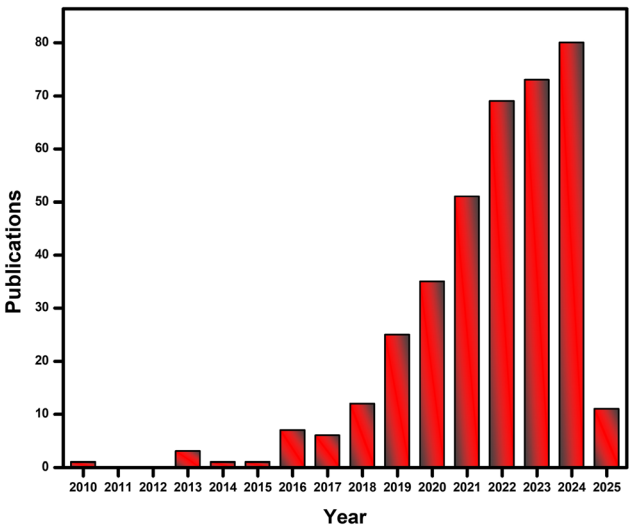

Fig. 2 A survey of the number of publications in recent years based on the Web of Science database for topic keywords "UiO-66-NH_2" and "photocatalysis".

development of more efficient and multifunctional UiO-66-NH_2-based photocatalysts. Overall, this work serves as a comprehensive resource for researchers and offers strategic insights into the design of next-generation UNH-MOF-based materials for sustainable photocatalysis. The progression of UiO-66-NH_2-based materials in the field of photocatalysis is illustrated in the timeline below (Fig. 1), showcasing key milestones and the development of various functional hybrid materials over the years. Additionally, Fig. 2 presents a survey of the number of publications related to UiO-66-NH_2 in photocatalytic applications in recent years, based on data retrieved from the Web of Science database.

2. Overview of UiO-66-NH_2 MOF

UiO-66-NH_2 consists of Zr-based metal clusters ($Zr_6O_4(OH)_4$) that act as nodes and organic linkers, *i.e.*, 2-amino-1,4-benzenedicarboxylate (H_2BDC-NH_2), which is nothing but NH_2-modified terephthalic acid. As shown in (Fig. 3c), it is composed of an inner $Zr_6O_4(OH)_4$ core where μ_3-O and μ_3-OH groups alternately cap the triangular faces of the Zr_6 octahedron. The Zr_6 cluster and NH_2-BDC linkers are coordinated through the carboxylate ($-COO^-$) groups of the ligand, and these clusters can coordinate with up to 12 carboxylate groups, providing a highly stable framework-like structure with exceptional thermal and chemical stability.[20,27] UNH MOF contains octahedral and tetrahedral cages (Fig. 3b) constructed by aligning the metal clusters and ligands. The diameter of octahedral and tetrahedral cages is about 11–12 Å and 8 Å, respectively, which provides enough space for the guest molecules incorporation,[28] as the presence of the $-NH_2$ group slightly reduces the pore size compared to the parent UiO-66 due to steric hindrance and interaction with guest molecules. The Brunauer–Emmett–Teller (BET) surface area of UiO-66-NH_2 typically lies in the range of 700–1000 $m^2\ g^{-1}$, slightly less than that of the non-functionalized UiO-66.26 The $-NH_2$ group in UiO-66-NH_2 reduces surface area and pore diameter by partially occupying pore space due to its bulky size. The $-NH_2$ groups enhance MOF hydrophilicity by forming hydrogen bonds with framework functional groups or polar molecules like H_2O and CO_2. This interaction can obstruct pores, reducing the effective pore diameter and accessible surface area. Moreover, amino functionalization enhances the material's ability to selectively interact with specific guest molecules through hydrogen bonding or electrostatic interactions.[29] UiO-66-NH_2 demonstrates excellent thermal stability, withstanding temperatures up to 300–500 °C under inert conditions. It is stable in a wide pH range (from acidic to basic conditions), owing to the strong Zr–O bonds.[30] The amino group can be further utilized through post-synthetic modifications in various catalytic and adsorption-related applications, making UiO-66-NH_2 an excellent candidate for material developments in heterogeneous catalysis, gas separation, and environmental remediation fields.

Under light illumination, UiO-66 generates photoexcited electron–hole (e^-/h^+) pairs, and the photogenerated electrons are transported from the excited organic linker (H_2BDC) to Zr-oxo clusters, resulting in the formation of Zr^{3+} through a linker to metal charge transfer (LMCT) mechanism. However, the photocatalytic performance of UiO-66 faces a significant challenge: the Zr-oxo clusters have a higher redox potential than the LUMO level of the H_2BDC linker. This energy mismatch hinders effective electron transfer from H_2BDC to Zr-oxo

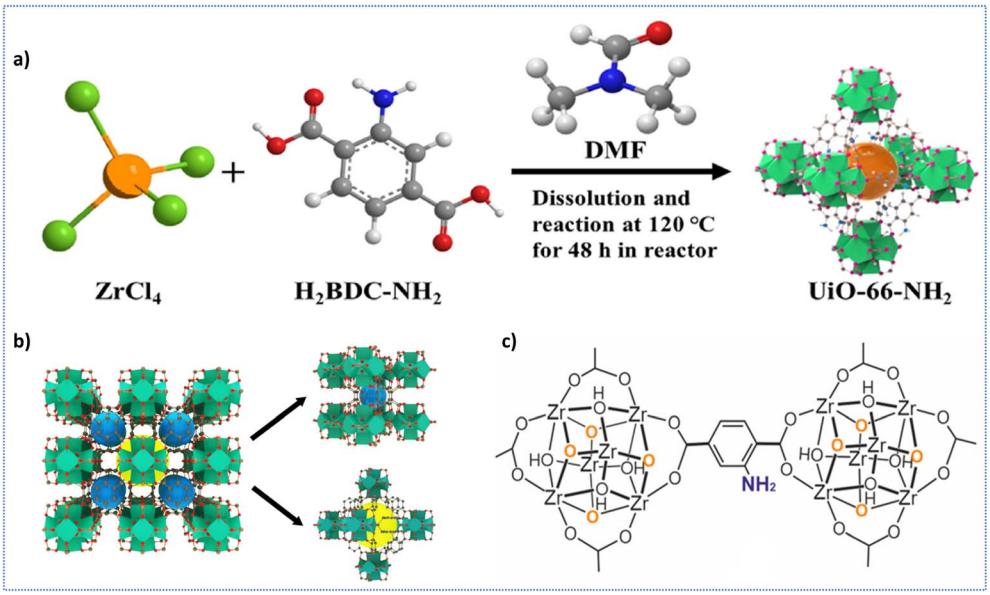

Fig. 3 (a) The schematic illustration of UiO-66-NH_2 synthesis, reproduced with permission from Elsevier. Copyright © 2021.[24] (b) Crystal structure of UiO-66(Zr) & its cavities, *i.e.*, (i) Td cavity, and (ii) Oh cavity. The void areas within the Td and Oh cages are represented by blue and yellow spheres, respectively, reproduced with permission from Elsevier. Copyright © 2022.[25] (c) Visual representation of basic sites in UiO-66-NH_2: the basic sites in $Zr_6O_4(OH)_4$ clusters and $-NH_2$ group of amino terephthalate linker are indicated by orange and blue, respectively, reproduced with permission from MDPI. Copyright © 2023.[26]

clusters. Additionally, the relatively wide bandgap of UiO-66 restricts its capacity to capture visible light. Thus, the energy gap of UiO-66 can be adjusted from 3.8 eV to 2.7 eV by the incorporation of $-NH_2$ group, which enables the LUMO's position to remain unchanged while the HOMO band shifts upwards due to the e^-- donating group's contribution. This results in a fully occupied and significantly reduced energy gap state. Silva *et al.*[20] further discovered that the inclusion of the $-NH_2$ group in the UiO-66-NH_2 MOF is crucial for the shifting of the absorption spectrum toward the visible light, peaking at 360 nm (with a strong absorption band spanning 300–440 nm) compared to UiO-66's absorption range of 270–300 nm. In a separate study, Sun *et al.*[27] introduced an additional $-NH_2$ group to the BDC-NH_2 linker to create a mixed UiO-66-NH_2/UiO-66-2,5-NH_2 framework. This new framework exhibited improved light absorption ability and photocatalytic activity over UiO-66-NH_2. This study emphasizes that boosting light absorption is possible by amplifying the no. of functional groups in the organic linker or opting for a mixed-linker strategy. UiO-66-NH_2 exhibits remarkable thermal and chemical stability, tunable optical properties, and enhanced photocatalytic activity due to amino functionalization. These attributes, combined with its ability to interact with guest molecules and facilitate post-synthetic modifications selectively, underscore its potential as a versatile material for advanced photocatalytic applications.

Having established the basic structural and chemical characteristics of UiO-66-NH_2, it is necessary to investigate how functionalization further improves its photocatalytic activity. The following section discusses the contribution of $-NH_2$ groups in adjusting electronic properties, enhancing charge separation, and broadening light harvesting capacity, which are key to improving the efficiency of UiO-66-NH_2-based photocatalysts.

3. Significance of $-NH_2$ functionalization

Amine functionalization is a highly effective approach to improve the stability and visible-light activity of MOFs. The inclusion of amino groups ($-NH_2$) in the MOF structure alters their electronic properties by introducing new energy states that decrease the band gap and extend light absorption into the visible spectrum, thereby improving the MOF's light capture and energy utilization ability.[31] The lone pair of N-atom in $-NH_2$ groups plays a critical role by raising the Fermi level, adjusting the conduction band, and facilitating efficient charge transfer. This reduces the photogenerated e^-–h^+ recombination, ensuring better charge separation. Additionally, amino groups assist in transferring charges between organic linkers and metal–oxo clusters, enhancing the excitation process.[32] The Lewis acidic nature of amines supports the generation of free electrons by facilitating their transfer into the conduction band and reduces charge recombination through extended conjugation.[33] In some cases, they can be used to trap the photogenerated electrons and create active reaction sites efficiently. By improving metal–ligand interactions, $-NH_2$ groups shift light absorption from the UV to the Visible range, further optimizing photocatalytic performance by improving π-conjugation and electron donation.[34]

Localized electronic states introduced by $-NH_2$ groups further affect the optical properties, *i.e.*, by amplifying visible-light absorption and enabling MOFs to utilize lower-energy photons more effectively. Strong bonds between metals and $-NH_2$ groups add to the framework's structural stability, safeguarding it during catalytic reactions. These groups also play a protective role by neutralizing harmful reactive oxygen species like $^{\bullet}OH$ and $^1O_2$ (singlet) and providing resistance toward the pH fluctuations that could otherwise degrade the MOF's structure.[35] In aqueous conditions, $-NH_2$ groups provide extra stability by making the MOF either hydrophilic or hydrophobic, depending on the type of amine used.[36,37] This versatility, combined with enhanced light absorption, reactive site formation, efficient charge separation, and improved resistance to chemical damage, draws attention to the potential of amine-functionalized MOFs for various applications in photocatalysis and beyond.

With a good grasp of how NH_2 functionalization improves the photocatalytic activity of UiO-66-NH_2, the next step is to investigate the different synthesis methods employed to prepare this MOF. The following section elaborates on traditional and advanced synthesis methods, emphasizing their influence on structural integrity, efficiency, and scalability.

4. Synthesis techniques

Different synthesis methods for UNH MOFs may include hydrothermal methods, solvothermal methods, microwave-assisted methods, mechanochemical, electrochemical, and sonochemical methods (Fig. 4). In this section, a detailed analysis of different synthesis methods has been discussed.

4.1. Solvothermal synthesis

Solvothermal and hydrothermal synthesis are the most common methods for preparing UiO-66-NH_2 MOFs. In

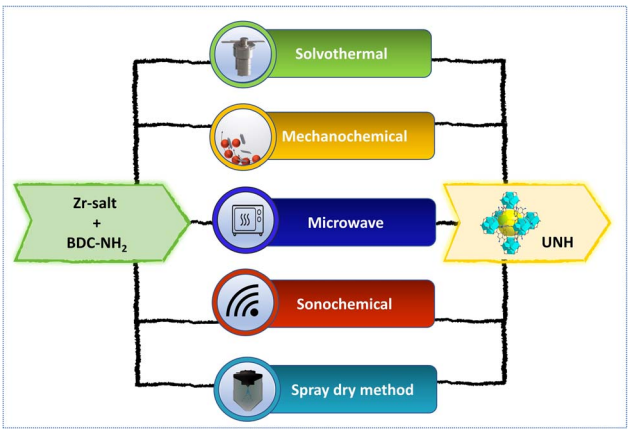

Fig. 4 Schematic representation of different synthesis methods of UiO-66-NH_2 (UNH).

solvothermal synthesis, the metal precursor (*e.g.*, $ZrCl_4$) and organic ligand (*e.g.*, $H_2BDC\text{-}NH_2$) are dissolved in a suitable solvent (Fig. 3a), then heated in a Teflon-lined autoclave. Typically, temperatures between 50–200 °C are used, and crystallization may take hours to days. Alternative Zr sources like zirconium oxychloride ($ZrOCl_2$) and zirconium butoxide ($Zr(OC_4H_9)_4$) can also be used. Depending on the metal and linker, solvents such as dimethylformamide (DMF), diethyl formamide (DEF), acetone ($(CH_3)_2CO$), acetonitrile (CH_3CN), ethanol (C_2H_5OH), and methanol (CH_3OH) are employed, as they significantly affect the crystallinity of the final products.[38–41] When H_2O is used as the solvent, the process is called hydrothermal synthesis. Solvent choice also influences reaction kinetics and the final crystal structures.[42,43] In some cases, modulating agents (such as acetic acid, formic acid, *etc.*) play a significant role in crystal nucleation and growth.[44]

In this regard, Zango *et al.* synthesized UiO-66 and UiO-66-NH_2, respectively, using the solvothermal method.[45] The mixture of $ZrCl_4$ and BDC was separately dissolved in DMF and stirred for 15 minutes to synthesize UiO-66. Similarly, for UiO-66-NH_2, BDC-NH_2 was used as the linker instead of BDC, which was dissolved in DMF, followed by stirring. The solutions containing salt and linker precursor were mixed and then heated at 120 °C for 16 hours in a 100 mL Teflon autoclave. After cooling, the precipitate was centrifuged and washed with ethanol and deionized water several times to rinse out the residual DMF and unreacted precursors. The resulting white UiO-66 and greenish yellow precipitate UiO-66-NH_2 were then dipped in methanol for pore size activation and were dried to get the final product. XRD analysis confirmed the formation and structural integrity of the MOFs, which is consistent with previous reports. FT-IR showed characteristic peaks at 1630 and 1378 cm^{-1} for C=O and C=C stretching in BDC and BDC-NH_2, while peaks at 1300 and 3500 cm^{-1} corresponded to carboxylate groups and O–H stretching from water molecules. A distinct peak at 3490 cm^{-1} in UiO-66-NH_2 indicated N–H stretching from the –NH_2 group. TGA revealed partial decomposition of organic linkers at 380 °C and complete degradation at 680 °C, confirming high thermal stability.

Following this, Priyadarshini *et al.* utilized the hydrothermal approach to synthesize UiO-66 and UiO-66-NH_2 MOFs.[46] The intense and sharp XRD diffraction peaks indicate the pure crystalline nature of the material.[19,47] Also, a little increase in UiO-66-NH_2's peak intensity is due to the functionalization of UiO-66, which further enhances the crystalline nature. The EDX analysis results show that UiO-66-NH_2 is made up of Zr, C, O, and N, whereas UiO-66 MOF comprises elements like Zr, C, and O, which further confirms the formation of MOFs. Similarly, Rahmidar *et al.* also used BDC and BDC-NH_2 linkers for UiO-66 and UiO-66-NH_2 MOF synthesis, respectively, and the resulting SEM images indicate that the structure of UiO-66-NH_2 is slightly agglomerated, which could be due to the introduction of the NH_2 group.[48] Similarly, Zr-BDC and Zr-BDC-NH_2 MOFs have respective surface areas of 714 and 757 $m^2\ g^{-1}$ based on the findings of BET analysis and have a cubic form and a homogeneous size of roughly 80 nm according to TEM images data.

In another study, Shen *et al.* synthesized UiO-66-NH_2 using a simple one-pot hydrothermal method by dissolving equimolar $ZrCl_4$ and BDC-NH_2 in DMF and heating the sealed mixture at 120 °C for 48 hours in a sealed Teflon autoclave.[49] After cooling, the product was washed with anhydrous CH_3OH and vacuum-dried for photocatalytic applications. XPS analysis showed Zr $3d_{5/2}$ and $3d_{3/2}$ peaks at 182.14 eV and 184.50 eV, confirming MOF formation. The N 1s peak at 399.21 eV indicated that –NH_2 groups remained intact and did not bond with Pd ions during synthesis. Similarly, Zhang *et al.* developed a greener synthesis route using ethanol and formic acid instead of DMF, producing UiO-66-NH_2, effective for the simultaneous reduction of Cr(VI) to the low-toxic Cr(III) and decontamination of Cr(VI) in the solution.[50]

Solvothermal synthesis has a major impact on the crystallinity, porosity, and concentration of defects in UiO-66-NH_2 and its composites, which in turn affect their photocatalytic activity. The solvent determines the growth kinetics and ultimate framework stability, with DMF favoring high crystallinity and ethanol-based synthesis favoring environmentally friendly routes with moderate porosity. Reaction time and temperature influence the creation of defects, wherein a more extended synthesis at higher temperatures increases structural order but can decrease active defect sites important for charge separation. Further, modulating agents such as acetic acid enhance porosity and surface area by regulating crystal growth, adsorption capacity, and catalytic efficiency in composite materials.

4.2. Microwave-assisted synthesis

Usually, the solvothermal synthesis method with conventional heating is used to synthesize UiO-66-NH_2 MOF. However, it has been observed that, in some cases, using modulating agents leads to longer crystallization times. Lately, microwave-assisted heating has gained attention as an alternative, promising method for synthesizing UiO-66-NH_2, offering higher yields and faster production rates within a shorter timeframe.[51] In the case of supersaturated solutions, it has been proven that microwave-assisted synthesis facilitates quick, homogeneous nucleation and crystallization.[52] Huang *et al.* prepared UiO-66-NH_2 using the solvothermal method by both conventional heating and microwave heating.[53] Using an 800 W microwave, uniform crystals (~600 nm) were formed within 30 minutes, whereas conventional heating required 20 hours to produce slightly smaller crystals (~500 nm) (Fig. 5a and b). The larger crystal size with microwave heating suggests suppressed homogeneous nucleation. Nitrogen adsorption isotherms showed a sharp uptake, indicating a microporous (type I) structure. FESEM and XRD results revealed enhanced crystallinity with increased AcOH content. Overall, microwave heating enabled faster and more efficient synthesis compared to conventional methods.

In another study, Solís *et al.* used the microwave-assisted synthesis to fabricate highly stable UiO-66-NH_2.[54] Here, for the first time, the effect of two Zr precursors: Zr oxychloride ($ZrOCl_2$) and organic Zr alkoxide ($Zr(OC_4H_9)_4$), across 120–180 °C, was explored. Even though for $Zr(OC_4H_9)_4$, temperature had little impact on the porosity, in the case of $ZrOCl_2$, it dramatically affects the porous structure, particularly at 160 and 140 °C,

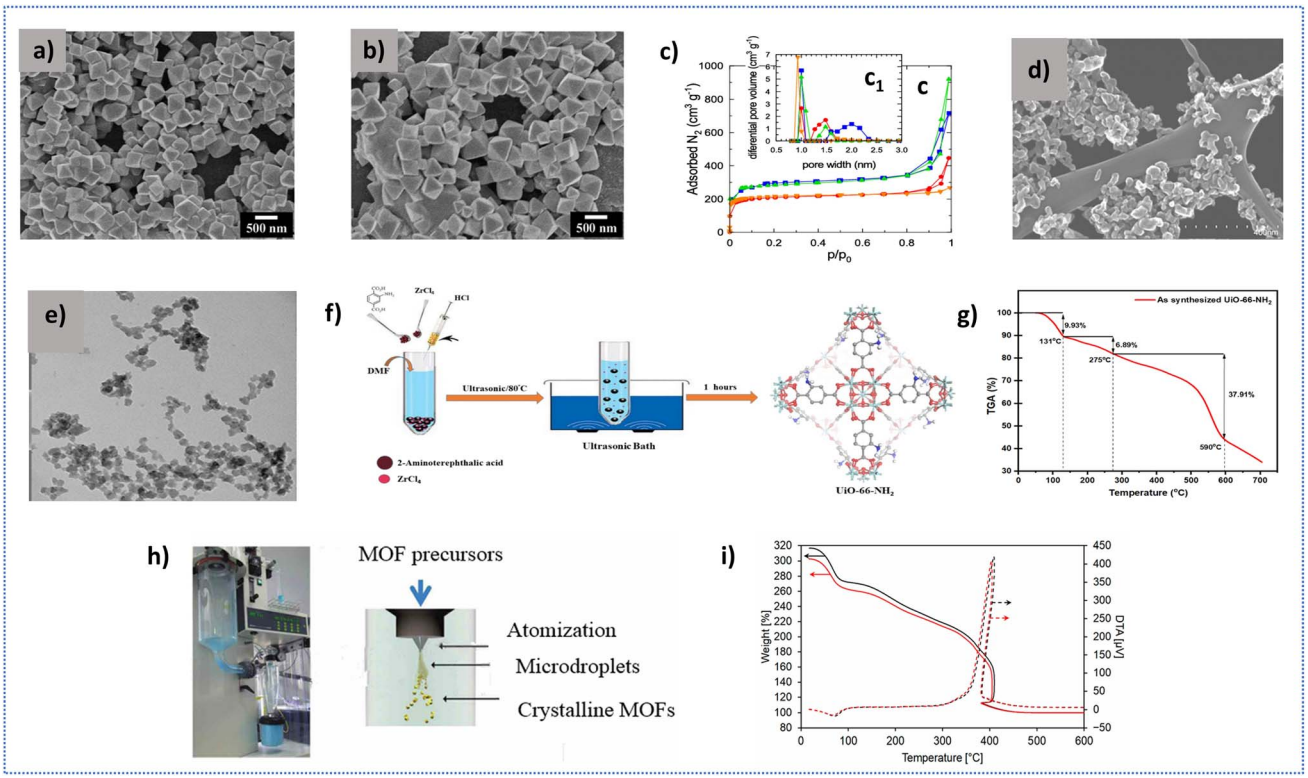

Fig. 5 (a) FESEM image of UiO-66-NH_2 synthesized *via* conventional heating at 150 °C for 20 hours and (b) synthesized using microwave heating at 150 °C for 30 minutes, reproduced with permission from Elsevier. Copyright © 2018.[53] (c) N_2 adsorption–desorption isotherms at −196 °C for UiO-66-NH_2 synthesized using $ZrOCl_2$ and (c1) Its corresponding pore size distribution, (d) STEM images of UiO-66-NH_2 synthesized at 140 °C using $ZrOCl_2$, (e) TEM images of UiO-66-NH_2 synthesized with $Zr(OC_4H_9)_4$, reproduced with permission from Elsevier. Copyright © 2022.[54] (f) Synthesis of UiO-66-NH_2 using the sonochemical method, (g) TGA curve of UiO-66-NH_2 synthesized *via* the sonochemical method, reproduced with permission from Nature. Copyright © 2023.[55] (h) Spray-drying technique for MOF synthesis, reproduced with permission from IOP Publishing. Copyright © 2017.[56] (i) TG (solid line) and DTA (dashed line) curves for b-UiO-66(Pr) (black) and sp-UiO-66(Pr) (red), reproduced with permission from MDPI. Copyright © 2024.[57]

in achieving the maximum for surface area (up to 900 $m^2\ g^{-1}$) and microporous volume, respectively. As shown in Fig. 5c, the pore size distribution was bimodal (1.5–2.0 nm) for $ZrOCl_2$ and unimodal (1.0–1.3 nm) for $Zr(OC_4H_9)_4$-based MOFs. The choice of Zr-precursor substantially affects the optical, structural, and morphological properties of UiO-66-NH_2. MOFs synthesized with $Zr(OC_4H_9)_4$ showed stronger visible-light absorption and smaller particle sizes (15–20 nm), while $ZrOCl_2$-based MOFs had larger particles (20–50 nm) and a UV-Vis absorption drop at 420–440 nm. Additionally, as shown in Fig. 5d and e, the smaller particles from the organic precursor formed larger, smoother aggregates due to rapid nucleation during microwave heating. This method not only accelerates synthesis but also offers better control over particle size and crystal growth compared to conventional techniques.

Compared to traditional solvothermal procedures, microwave heating yields highly crystalline MOFs with homogeneous particle sizes, often between 15 and 50 nm, depending on the Zr precursor employed. It leads to smaller, discrete particles with nucleation and growth under controlled conditions, enhancing surface area and micro-porosity. This procedure provides a more efficient, faster alternative to traditional synthesis and is well-suited to optimizing structural and functional properties.

4.3. Mechanochemical synthesis

To reduce environmental impact, mechanochemical synthesis offers a solvent-free, rapid alternative to conventional MOF synthesis. In this method, the synthesis of MOF can be done by reacting the reactants and applying mechanical force.[58] This approach enables UiO-66 and UiO-66-NH_2 formation at room temperature in 10–60 minutes, with water as the only byproduct.[59] Užarević *et al.* first demonstrated gram-scale, solvent-free synthesis without strong acids, high temperatures, or excess reactants.[60] MOFs were prepared by dry milling or exposing solid reactant mixtures to organic vapors using two main techniques: Liquid-Assisted Grinding (LAG) and Accelerated Aging (AA).

In the case of AA, a solid reactant mixture is exposed to a suitable temperature and atmosphere to enhance the aging process of MOF, which further helps to accelerate the photocatalytic activity. As per PXRD analysis, dry milling of precursor 1, *i.e.*, benzoate cluster $Zr_6O_4(OH)_4(C_6H_5CO_2)_{12}$ and H_2tpa, didn't result in a chemical reaction even after 90 minutes of milling. When the process was changed to LAG using DMF, it showed a broad PXRD peak corresponding to the (111) reflection of UiO-66, and the complete disappearance of X-ray

reflections of the reactant indicates the successful product formation. Similarly, when LAG with DMF is used to precursor 2, *i.e.*, methacrylic acid, $Zr_6O_4(OH)_4(C_6H_5CO_2)_{12}$, and H_2tpa, no significant improvement has been observed. In contrast, when MeOH was used, the product displayed some sharp PXRD patterns that well matched the UiO-66 structure. When precursor 2 and H_2atpa were milled in the presence of MeOH, after 90 minutes, PXRD analysis showed the formation of UiO-66-NH_2, which is isostructural to UiO-66. The BET surface areas were 945 $m^2\ g^{-1}$ for UiO-66-NH_2 when washed and activated, while it is 925 $m^2\ g^{-1}$ when synthesized from precursor 1 *via* LAG. MeOH was used only for milling and washing to avoid toxic DMF. In the AA method, minimal grinding of precursor 2 with H_2tpa or H_2atpa, followed by MeOH vapor exposure, yielded crystalline UiO-66 (after 1 week) and UiO-66-NH_2 (after 3 days). PXRD confirmed high crystallinity and BET surface area. This method eliminates the need for acidic reagents like HCl, $ZrCl_4$, or $ZrOCl_2$, while maintaining the high stability and performance of the resulting MOFs.

Mechanochemical synthesis is a green strategy for UiO-66-NH_2 preparation that avoids bulk solvents and shortens reaction time. It forms highly crystalline, high-surface-area materials with increased porosity and catalytic activity. Methods such as liquid-assisted grinding and accelerated aging enable controlled growth and nucleation, yielding sharply defined structures with increased stability. The absence of strong acidic reagents also maintains the structural stability of the material, making it a clean process compared to traditional synthesis.

4.4. Sonochemical synthesis

The sonochemical method is another method in which ultrasound waves accelerate the chemical reactions. When high-frequency ultrasonic waves pass through a liquid medium, micro-sized bubbles are generated, which then rapidly collapse. This collapse creates extreme conditions due to localized extreme temperatures (reaching up to 5000 K) and pressures (up to 1000 atm) that accelerate the chemical reactions. Sonochemical synthesis is advantageous due to its greater efficiency, shorter reaction times, and ability to synthesize materials with unique properties like high surface area, purity, and controlled particle size of different materials, particularly for MOFs.[61,62] In MOF synthesis, this method accelerates the nucleation and development of crystals, leading to shorter synthesis times than conventional techniques.

Kazemi *et al.* synthesized UiO-66-NH_2-MOF *via* a sonochemical method using $ZrCl_4$, NH_2-BDC, and DMF as MOF precursors.[55] After dissolving $ZrCl_4$ in DMF and adding HCl to clear the solution, NH_2-BDC in DMF was introduced into it. From Fig. 5f, it can be seen that the mixture underwent ultrasonic irradiation at 80 °C for 1 hour, where cavitation facilitated rapid heating and cooling cycles, promoting uniform nanoparticle formation. The resulting MOF had an average particle size below 100 nm, significantly smaller than those from solvothermal methods. XRD and FT-IR data matched simulated UiO-66-NH_2 patterns, confirming successful synthesis. A high BET surface area of 993.1 $m^2\ g^{-1}$ and increased pore volume indicated strong microporosity, outperforming solvothermal samples (876 $m^2\ g^{-1}$). TGA showed stability up to 590 °C, with minor weight loss due to moisture. This method offers a fast and efficient synthesis route, yielding materials ideal for environmental applications.

Sonochemical synthesis employs ultrasonic cavitation, creating microbubbles imploding under severe localized conditions. Such conditions enhance nucleation, resulting in the quick formation of smaller nanoparticles (<100 nm) and increased crystallinity. The synthesis yields UiO-66-NH_2 with greater BET surface areas (~993.1 $m^2\ g^{-1}$) and better microporosity, maximizing adsorption performance. The reduced synthesis time avoids overgrowth of the crystal, leading to a homogeneous morphology. Moreover, the material possesses superior thermal stability up to 590 °C. Thus, sonochemical synthesis proves to be a highly efficient and promising approach to designing MOFs for applications that demand high surface areas and increased adsorption.

4.5. Spray drying synthesis

Spray drying is a rapid, sustainable, and cost-effective method for synthesizing MOFs. The conventional synthesis methods require the continuous presence of heat and a certain amount of organic solvents, which can be challenging for large-scale synthesis. In contrast to traditional methods, this method offers several benefits, including excellent yields, continuous production in a single step, negligible moisture content in the product, a shorter reaction time, and no need to separate the product from the solvent. In this method, MOF precursor solution is sprayed in the form of droplets and then quickly dried by using hot air (150–250 °C) to form MOF nanoparticles. Fig. 5h illustrates the spray synthesis setup with a two-fluid nozzle spray chamber, heating tube, and filter frame. The precursor solution is introduced into the two-fluid nozzle *via* a syringe pump and sprayed with clean air. In a heating tube, the sprayed droplets were heated to 180 °C, then the samples were ultrasonically cleaned in DMF and ethanol to remove any remaining precursors. Following three rounds of washing, centrifugation, and drying for 6 h at 80 °C, the final product was obtained. However, the rapid evaporation time is insufficient for SBU formation, hence it is essential to preheat the precursor solution before spraying, as SBU formation takes place during the preheating stage.

UiO-66 and UiO-66-NH_2 were synthesized by Kubo *et al.* using spray synthesis with/without preheating with different precursors.[57] With $ZrCl_4$, preheating was essential, whereas $Zr(OnPr)_4$ combined with AcOH rapidly formed SBUs, eliminating the need for preheating. This is because of the ability of $Zr(OnPr)_4$ to form SBUs with AcOH rapidly. In UiO-66-NH_2 synthesis using $Zr(OnPr)_4$ and NH_2-BDC (NH_2-BDC/Zr ratio: 2.5–6.0), the H_2O/Zr ratio was maintained at 1 due to its crucial role in crystallization. XRD confirmed that UiO-66-NH_2 matched batch-synthesized (b-UiO-66-NH_2) MOFs. Notably, adding H_2O to the Zr solution (not NH_2-BDC) yielded high crystallinity due to Zr-acetate cluster formation. Further studies on b-UiO-66-NH_2 before and after washing using AcOH/Zr = 440 and H_2BDC-NH_2/Zr = 2.5 revealed that sp-UiO-66-NH_2(Pr) had a BET surface area of 1263 $m^2\ g^{-1}$ and total pore volume of 2.33 $cm^3\ g^{-1}$, both

Table 1 Comparison of UNH-MOF synthesis methods: key features, advantages, limitations, and property influence

Synthesis method	Key features	Advantages	Limitations	Influence on properties
Solvothermal	Precursors dissolved in solvent, heated in an autoclave	High crystallinity, well-defined morphology, and widely applicable	Time-consuming (several hours to days), uses large amounts of organic solvents	Large particles, tunable pore structures, controlled phase purity
Microwave-assisted	Rapid heating using microwave irradiation	Faster nucleation (minutes), uniform morphology, energy-efficient	Limited scalability, requires careful control of microwave power	Smaller, well-dispersed nanoparticles, enhanced surface area, and high crystallinity
Mechanochemical	Solvent-free, mechanical force-driven reaction	Eco-friendly, fast (10–60 min), no harsh solvents	Limited to specific MOFs, some reactions require liquid-assisted grinding (LAG)	High crystallinity, comparable porosity to solvothermal synthesis
Sonochemical	Ultrasound-induced cavitation accelerates the reaction	Rapid synthesis (<1 h), uniform nanoparticles (<100 nm), higher BET surface area	Requires optimization of ultrasonic parameters	Smaller particle size, enhanced surface area, increased thermal stability
Spray drying	Precursor solution is atomized and rapidly dried	Continuous, scalable, high-purity, controlled morphology	Requires preheating for some precursors; rapid evaporation may hinder SBU formation	Higher surface area (1319 m^2 g^{-1}), increased porosity (2.33 cm^3 g^{-1}), improved adsorption

higher than the unwashed sample and b-UiO-66-NH_2. Rough morphology of sp-UiO-66-NH_2(Pr) was attributed to NH_2-BDC disintegration, which further expanded the tiny pores of the UiO-66-NH_2 crystals, forming macropores. Fig. 5i explains the TG-DTA curves of b-UiO-66-NH_2(Pr) and sp-UiO-66-NH_2(Pr), which show similar weight losses for both samples. Accordingly, the evaporation of physically adsorbed solvents, the removal of hydroxyl groups from UiO-66-NH_2 structure ($Zr_6(OH)_4O_4(BDC\text{-}NH_2)_6 \rightarrow Zr_6O_6(BDC\text{-}NH_2)_6 + 2H_2O$), and dissolution of NH_2-BDC linkers are responsible for the weight losses in the 25–100 °C, 150–300 °C, and 300–450 °C ranges respectively. This suggests that there was consistent thermal stability between sp-UiO-66 NH_2 (Pr) and b-UiO-66-NH_2 (Pr). The above findings confirm that using the spray method, further advancements in the UiO-66-NH_2 and other MOF synthesis can be done for various applications.

Spray drying improves the synthesis of MOFs by providing greater yield, purity, and quicker production. Atomization of the precursor solution into droplets is followed by quick drying using hot air. Preheating the precursor solution facilitates the formation of SBUs. With $Zr(OnPr)_4$ as a precursor, efficient SBU formation is possible without preheating, whereas $ZrCl_4$ needs preheating for maximum crystallization. Spray-dried UiO-66-NH_2 possesses enhanced surface area (1319 m^2 g^{-1}) and pore volume (0.42 cm^3 g^{-1}) with spherical particles that collapse into rough surfaces, enhancing pore volume to 2.33 cm^3 g^{-1}. Such modifications enhance adsorption characteristics, whereas thermal stability is comparable to traditionally synthesized materials. Table 1, given below, provides an overview of various synthesis methods, highlighting their key features, advantages, limitations, and their influence on the properties of MOF.

With a thorough insight into the UiO-66-NH_2 synthesis and structural adjustments, the discussion advances to its vast photocatalytic uses. The following sections examine its activity in significant environmental and energy applications, highlighting its strengths and weaknesses in real-world contexts.

5. Photocatalytic applications

Photocatalysis refers to the acceleration of chemical reactions under light exposure (like visible, UV, or IR) in a suitable semiconductor that absorbs light and drives various transformation reactions. In this process, the first is the absorption of light with energy equal to or greater than the semiconductor's bandgap, promoting electrons from the VB to the CB and leaving behind holes. Secondly, these photogenerated charge carriers must efficiently separate and migrate to the surface in order to take part in redox reactions. Over recent years, UiO-66-NH_2 MOFs have emerged as promising strategies for environmental remediation and sustainable energy generation applications that offer ideal band alignment and optoelectronic properties, making them highly suitable for efficient solar-driven chemical conversions. In this section, we have discussed the fundamental principles, structural features, and their relationship to photocatalytic activity in key reactions such as H_2 production, CO_2 reduction, Cr(VI) reduction, dye and antibiotic degradation, and N_2 fixation. The Fig. 6, below, represents the general mechanism of various photocatalytic redox reactions in UNH-MOF.

5.1. H_2 and O_2 evolution reaction

Inspired by natural photosynthesis, photocatalytic overall water splitting (OWS) utilizes solar energy and water, along with photocatalysts, to generate hydrogen and oxygen in an environmentally friendly manner, without causing any harmful effects to the environment. However, this reaction requires a Gibbs free energy of 237.2 kJ mol^{-1} and a minimum photon energy of 1.23 eV to initiate the water splitting process.

Overall water splitting (OWS) reaction:

$$2H_2O + h\nu \rightarrow 2H_2 + O_2,\ \Delta G^\circ = 237.2\ \text{kJ mol}^{-1} \quad (1)$$

H_2 evolution reaction (HER):

$$4H^+ + 4e^- \rightarrow 2H_2,\ \Delta E^\circ = 0\ \text{V} \quad (2)$$

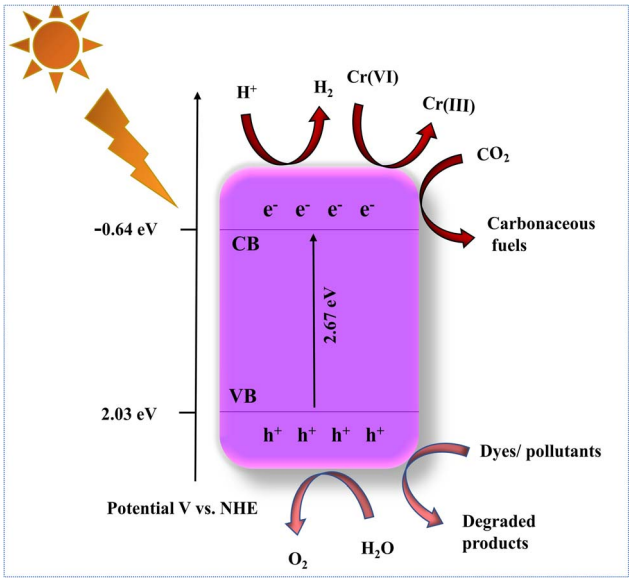

Fig. 6 Schematic illustration of various photocatalytic redox reactions driven by solar energy.

O_2 evolution reaction (OER):

$$2H_2O \rightarrow 4H^+ + 4e^- + O_2,\ \Delta E^\circ = 1.23\ V \quad (3)$$

As shown in the above equations, OWS reaction is a combination of 2 simultaneous reactions: HER and OER and feasibility of the reaction is determined by the redox potential involved; specifically, reduction can proceed only if the CB potential of the semiconductor is more −ve than the reduction potential of the proton ($H^+/H_2 = 0.00$ V *vs.* the normal hydrogen electrode (NHE) at pH 0), and for oxidation to occur, the VB potential should be more +ve than the oxidation potential of water (O_2/H_2O = +1.23 V *vs.* NHE at pH 0). As shown in eqn (1)–(3), the photocatalytic H_2O – splitting process involves the following key steps: (i) photon absorption and electron–hole (e^-/h^+) pairs separation, (ii) charge carriers migration and transport to the photocatalyst's surface, (iii) surface-adsorbed protons (H^+) get reduced to H_2 by CB – e^-, while holes in the VB facilitate water oxidation, leading to oxygen (O_2) formation.

In this regard, a no. of research has been extensively studied on MOF-based photocatalysts for H_2 and O_2 evolution. MOFs have open metal sites, unsaturated metal centers, and organic linkers that are catalytically active, enabling them to function as catalysts independently. UiO-66-NH_2 MOF is used for this investigation because of its higher stability, adjustability, and favorable photoactive characteristics for photocatalysis. There is a lot of potential for UiO-66-NH_2 and its composites for H_2 and O_2 evolution reactions. Noble metals such as Pd, Pt, and Ag possess properties like high electrical conductivity and efficient charge separation, making them promising candidates for HER and OER. Consequently, they are incorporated into composites with UiO-66-NH_2 to enhance the photocatalytic activity of the MOF further. Pt nanoparticles can act as electron acceptors to enhance the charge carrier separation efficiency, thereby improving the catalytic efficiency of the MOF material. For example, Xiao *et al.*[63] studied the impact of Pt nanoparticle location in two UiO-66-NH_2-based photocatalysts over H_2 production efficiency. In one, Pt nanoparticles were surface-deposited on UiO-66-NH_2 (Pt/UiO-66-NH_2), while in the other, they were encapsulated within its voids (Pt@UiO-66-NH_2). Both Pt-decorated photocatalysts exhibited greater efficiency compared to the pristine MOF. Still, the activity of Pt@UiO-66-NH_2 was much higher *i.e.*, 257.38 μmol g^{-1} h^{-1}, which is nearly 150 times greater than the parent MOF and 5 times greater rate than Pt/UiO-66-NH_2 (in Fig. 7a). This enhancement can be attributed to the unique structural properties of UiO-66-NH_2, which govern charge transfer dynamics and catalyst stability. The encapsulation of Pt nanoparticles within the MOF's voids ensures close contact with the framework, facilitating efficient proton access and significantly reducing e^-–h^+ recombination, as confirmed by ultrafast transient absorption (TA) spectroscopy. In contrast, Pt nanoparticles on the surface (Pt/UiO-66-NH_2) are more prone to aggregation and leaching, which compromises their catalytic stability. The strong confinement within UiO-66-NH_2 preserves the structural integrity and crystallinity of Pt@UiO-66-NH_2, enhancing its recyclability and sustained activity. This work highlights the critical role of Pd nanoparticle positioning in optimizing photocatalytic efficiency through improved charge carrier dynamics and structural stability. Similarly, Subudhi *et al.*[69] also studied the composite formation of gold-Au nanoparticles with UiO-66-NH_2 and observed that the rate of H_2 evolution follows the order of Au/UiO-66-NH_2 > UiO-66-NH_2 > UiO-66. The above rate order can be explained as the –NH_2 functionalized linker in UiO-66-NH_2 improves visible-light uptake capacity, while the deposition of Au nanoparticles (Au/UiO-66-NH_2) introduces strong LSPR effects. Under visible-light irradiation, Au nanoparticles generate excited electrons through the LSPR effect, and these excited electrons migrate from UiO-66-NH_2 to the Au nanoparticles until an equilibrium is reached. Au nanoparticles' ability to efficiently capture the photogenerated electrons improves the photo-stability of the photoexcited carriers and reduces the recombination of e^-–h^+ pairs. Consequently, the peak H_2 evolution rate for Au/UiO-66-NH_2 reached 387 μmol h^{-1}, surpassing the rates of 3 μmol h^{-1} for UiO-66 and 117.46 μmol h^{-1} for UiO-66-NH_2. To further improve the photocatalytic studies, two different nanoparticles (NPs) can be used to utilize the synergistic effects of both NPs. Following this approach, a noble bimetallic nanoparticle (Ag/Pd) loaded UiO-66-NH_2 was synthesized by Dash *et al.* using a simple adsorption–reduction method.[64] UiO-66-NH_2 was stirred in a water/methanol solution, followed by adding Ag and Pd salts and $NaBH_4$ at low temperatures. The highest H_2 evolution capacity of 448.2 μmol h^{-1} is observed in the case of (1 : 2) Ag/Pd@UiO-66-NH_2 composite, which is about four-fold higher than that of pure MOF. The black spots on the octahedral MOF's surface in the HRTEM images confirms the successful deposition of NPs that further leads to the gradual red shifting in the UV-vis absorption band indicating the improvement in photon receptiveness ability (Fig. 7b). The enhanced photocatalytic H_2 production by Ag/Pd@UiO-66-NH_2 stems from the synergistic interaction between the MOF and the embedded bimetallic nanoparticles.

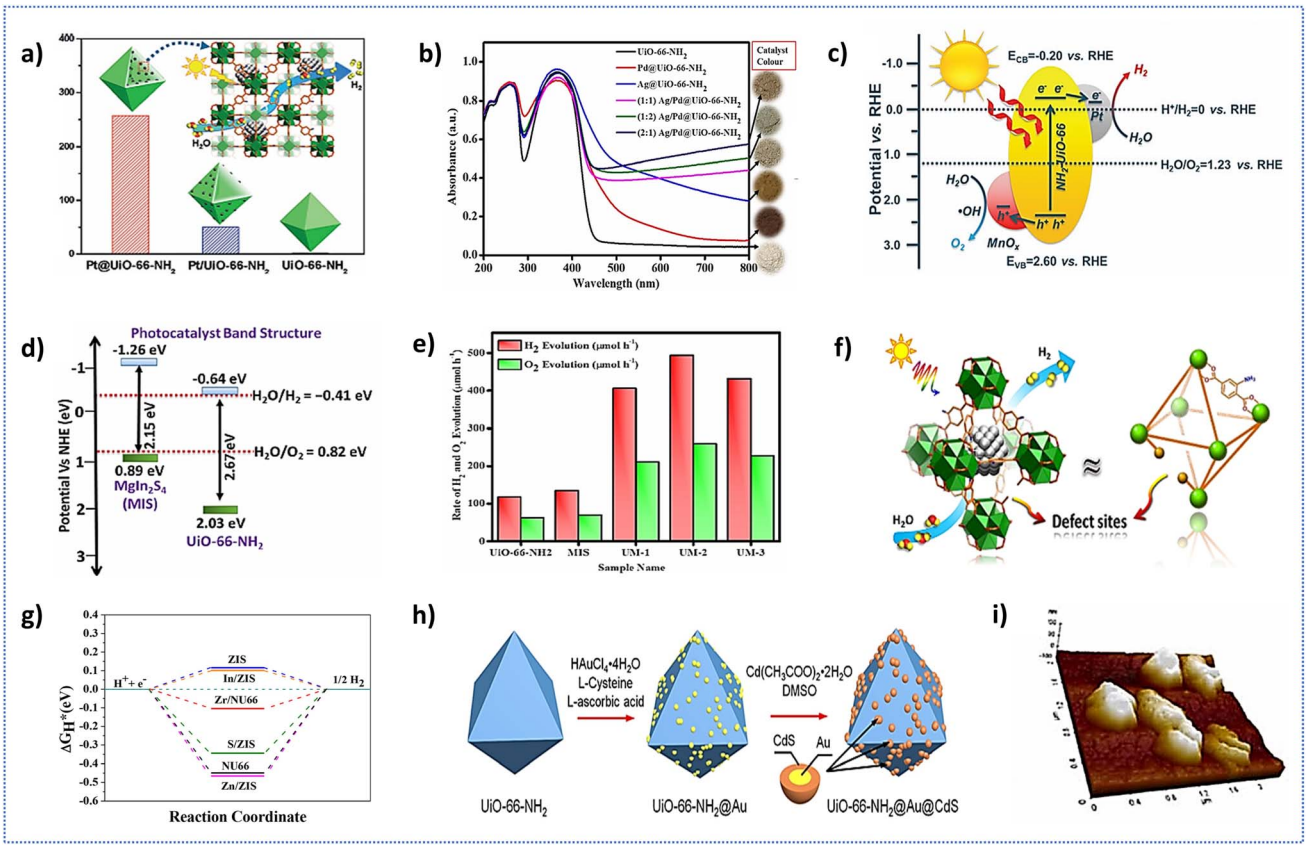

Fig. 7 (a) H_2 evolution rate of UiO-66-NH_2, Pt/UiO-66-NH_2, and Pt@ UiO-66-NH_2, reproduced with permission from Wiley. Copyright © 2016.[63] (b) UV-vis DRS spectra of the samples, reproduced with permission from The Royal Society of Chemistry. Copyright © 2024.[64] (c) Schematic illustration of overall water splitting reaction with PUM sample, reproduced with permission from Wiley. Copyright © 2020.[65] (d) Band structure of UiO-66-NH_2 and MIS, (e) H_2 and O_2 evolution performance of UiO-66-NH_2, MIS, UM-1, UM-2, UM-3, reproduced with permission from American Chemical Society. Copyright © 2023.[8] (f) Photocatalytic H_2 production by Pt@UiO-66-NH_2-X with structural defects, reproduced with permission from Wiley. Copyright © 2019.[66] (g) Calculated free energy diagram for HER based on the DFT method, reproduced with permission from American Chemical Society. Copyright © 2019.118 (h) Illustration of the synthesis process of the UiO-66-NH_2@Au@CdS, reproduced with permission from Springer. Copyright © 2023.[67] (i) AFM images of NiCo-LDH@NH_2-UiO-66, reproduced with permission from The Royal Society of Chemistry. Copyright © 2023.[68]

Under visible-light irradiation, electrons in the VB (2.03 eV) of UiO-66-NH_2 are excited to its CB (−0.64 eV), leaving behind holes. These excited electrons are swiftly transferred to the Ag/Pd surface due to the Schottky barrier at the MOF–metal interface, effectively suppressing electron–hole recombination, as confirmed by PL, TRPL, and EIS analyses. Additionally, the Ag component introduces a strong LSPR effect, enhancing light absorption and creating a localized electromagnetic field that promotes exciton generation and electron mobility. The accumulated electrons on the bimetallic surface act as reduction sites for protons, resulting in efficient H_2 evolution, while holes in the VB are scavenged by methanol, maintaining charge separation. Recyclability tests confirmed the material's stability over four cycles, and post-reaction XRD showed no structural degradation, validating the durability of the composite. The performance parameters of various UiO-66-NH_2-based photocatalysts have been summarized in Table 2.

Magnetic Fe_3O_4 can also be an ideal choice for making composites with other semiconductors due to its ability to enhance exciton separation, making the resulting photocatalysts efficient and cost-effective for energy applications. To this, a citrate-capped Fe_3O_4@UiO-66-NH_2 heterostructure composite (MU-2) was synthesized by Tripathy *et al.* *via* a solvothermal method, showcasing significant enhancement in photocatalytic H_2 evolution.[70] When Fe_3O_4 nanoparticles are stabilized with citrate ions, it prevents aggregation and provides functional carboxyl groups for further modification. The integration of magnetic Fe_3O_4 with UiO-66-NH_2 increased the composite's surface area (572.13 $m^2\ g^{-1}$) and this increased SA provides significant interfacial interaction between the materials, that leads to an efficient Z-scheme heterojunction and thereby improves the migration of charge carriers. Hence, MU-2 demonstrated a hydrogen evolution rate of 417 mmol h^{-1} under visible light, outperforming pristine UiO-66-NH_2. The apparent conversion efficiency (ACE) reached 3.12%, underscoring the synergistic effect of Fe_3O_4 and UiO-66-NH_2 in optimizing exciton dynamics and light-harvesting capabilities. The composite maintained structural integrity and catalytic performance over multiple cycles, highlighting its higher stability and potential for renewable energy applications.

Table 2 Summary of UiO-66-NH_2 based photocatalysts for H_2 and O_2 evolution reactions

Sl no.	Material	Synthesis method	S_{BET} [$m^2\ g^{-1}$]	Light source	ACE %	Photocatalytic activity	Reusability cycles	Ref.
1	Fe_3O_4@UiO 66-NH_2	*In situ* solvothermal (120 °C for 24 h)	572.13	300 W Xe lamp	3.12	417 μmol h^{-1}	3	70
2	α-MnO_2@UiO-66-NH_2	Solvothermal treatment (140 °C for 12 h)	709.34	300 W Xe lamp with $\lambda \geq 420$ nm filter	3.01	410.6 μmol h^{-1}	4	9
3	$MgIn_2S_4$/UiO-66-NH_2	Solvothermal (120 °C for 24 h)	364.74	300 W Xe lamp with $\lambda \geq 420$ nm filter	3.7 1.94	493.8 μmol h^{-1} (HER) 258.6 μmol h^{-1} (OER)	4	8
4	MoS_2/UiO-66-NH_2	Hydrothermal (120 °C for 24 h)	1017.36	300 W Xe arc lamp (cutoff filter >420 nm)	3.84 1.97	512.9 μmol h^{-1} (HER) 263.6 μmol h^{-1} (OER)	4	71
5	Au/UNH	Adsorption-reduction method	—	300 W Xe arc lamp (cutoff filter >420 nm)	—	387 μmol h^{-1}	3	69
6	Ag/Pd loaded UNH	Adsorption-reduction method	681.29	300 W Xe arc lamp (cutoff filter >420 nm)	3.30	448.2 μmol h^{-1}	4	64
7	Pt@UiO-66-NH_2	Solvothermal/ sonochemical	—	Visible light	—	257.38 μmol g^{-1} h^{-1}	4	63
8	UiO-66-NH_2-150@CdS	Reflux 80 °C for 10 h	107.6	300 W solar simulated Xe light source (350 nm < λ < 780 nm)	—	2303 μmol g^{-1} h^{-1}	6	72
9	Pt@UiO-66-NH_2-*X*	Room temp. Stirring for 20 h	1057	300 W Xe lamp with a UV cut-off filter (>400 nm)	3.02	381.2 μmol g^{-1} h^{-1}	10	66
10	$Cd_{0.2}Zn_{0.8}S$@UiO-66-NH_2	Facile solvothermal method (160 °C for 4 h)	266	300 W Xe arc lamp (cutoff filter >420 nm)	—	5846.5 μmol g^{-1} h^{-1}	4	73
11	Pt@NH_2-UiO-66/MnO_x (PUM)	Solvothermal (120 °C for 24 h)	493	Visible light	—	19.6 μmol g^{-1} h^{-1} (HER) 10.1 μmol g^{-1} h^{-1} (OER)	—	65
12	UiO-66-NH_2@Au@CdS	*In situ* growth of Au on MOF, then solvothermal deposition of CdS (180 °C for 12 h)	—	300 W Xe arc lamp (cutoff filter > 420 nm)	—	39.5 μmol h^{-1}	—	67
13	$CoTiO_3$/UiO 66 NH_2	Hydrothermal (120 °C for 24 h)	413.027	250 W lamp with λ > 400 nm filter	3.97	530.87 μmol h^{-1}	4	74
14	Mxene Ti_3C_2	Solvothermal (24 h at 120 °C)	72.05	—	9.1	570 μmol h^{-1}	3	75
15	PTPA/UiO-66-NH_2	Solvothermal method (120 °C for 24 h)	333.5	300 W Xe lamp, λ > 400 nm	—	—	—	76
16	Pd/UN/$ZnIn_2S_4$	Solvothermal (180 °C for 10 h)	165.2	300 W Xe arc lamp with a cutoff filter (λ > 420 nm)	3.2	5.26 mmol g^{-1} h^{-1}	5	77
17	TiO_2	Solvothermal (120 °C for 16 h)	238	300 W Xe lamp, λ > 420 nm	4	2.82 μmol h^{-1}	3	78

Additionally, due to its magnetic properties, this material can be easily separated and recovered from the solution mixture using an external magnet. This work exemplifies a noble-metal-free approach, leveraging defect engineering and heterostructure formation to enhance UiO-66-NH_2-based photocatalytic H_2 evolution. Similarly, another work to enhance the e^-/h^+ separation is done in which two cocatalysts are used to improve the redox process in the photocatalysis. Zhang *et al.*[65] demonstrated efficient electron–hole separation using Pt and MnO_x as co-catalysts in the Pt@NH_2-UiO-66/MnO_x (PUM) photocatalyst. When a comparative study is done in the case of Pt@NH_2-UiO-66/MnO_x (PUM), pure NH_2-UiO-66, Pt@NH_2-UiO-66 (PU), and NH_2-UiO-66@MnO_x (UM), PUM showed the best H_2 production activity among them. As shown in Fig. 7c, the photocatalytic water-splitting mechanism in the Pt@NH_2-UiO-66@MnO_x (PUM) composite is driven by the spatial separation of redox cocatalysts, Pt as a reduction site and MnO_x as an oxidation site, anchored on the UiO-66 MOF matrix. Upon visible-light irradiation, NH_2-UiO-66 absorbs photons and generates electron–hole pairs. The photogenerated electrons are efficiently extracted by embedded Pt nanoparticles *via* a Schottky junction, enabling directional electron transfer and suppressing recombination. These electrons drive the reduction of water to H_2 on the Pt surface, while holes migrate to MnO_x nanoparticles on the MOF exterior. MnO_x, acting as an effective hole acceptor, accelerates the oxidation of water to generate $^{\bullet}OH$ radicals, as evidenced by EPR analysis, where $^{\bullet}OH$ signal intensity followed the trend: NH_2-UiO-66 < PU < UM < PUM. This spatial configuration prolongs charge carrier lifetimes, as confirmed by PL and transient absorption studies, and supports directional redox activity. The porous MOF framework plays a pivotal role in separating Pt and MnO_x domains, minimizing recombination, and enhancing charge transport. Overall, this architecture significantly improves interfacial charge dynamics and boosts hydrogen and oxygen evolution efficiency in water splitting. In summary, the photocatalytic mechanism facilitated electron–hole separation, extended their lifetime, and enhanced redox reactions, boosting hydrogen production.

Next to oxides, metal sulfides are also promising candidates for photocatalytic water splitting due to their light absorption ability and chemical stability. Among them, ternary metal chalcogenides like $MgIn_2S_4$ stand out due to their narrow bandgap, excellent light absorption ability, and superior optoelectronic properties, making them ideal for forming heterojunctions with UiO-66-NH_2 (UNH) to further enhance its photocatalytic activity. To leverage these advantages, Tripathy *et al.*[8] synthesized a $MgIn_2S_4$/UiO-66-NH_2 nanohybrid photocatalyst using an *in situ* solvothermal method, achieving significantly improved photocatalytic performance for water redox reactions compared to the individual components. The decrease in BET surface area of the composite is attributed to interfacial contact between UiO-66-NH_2 and $MgIn_2S_4$, which facilitates charge transfer. Additionally, the aggregated morphology of the composite further contributes to this decline. However, the rigidity of the UNH framework remains intact even after composite formation that explains the composite's stability. As shown in Fig. 7d, the band structure alignment of both materials is well-suited for hydrogen evolution (HER) and oxygen evolution (OER) reactions. Furthermore, EPR analysis confirmed the generation of $^{\bullet}O_2^-$ and $^{\bullet}OH$ radicals under light irradiation, indicating a double charge transfer pathway. Among the composites tested, the 5 wt% UM-2 variant exhibited the highest efficiency, achieving 493.8 μmol h^{-1} of H_2 and 258.6 μmol h^{-1} of O_2, approximately four times higher than the pristine materials (Fig. 7e). This remarkable improvement is attributed to strong interfacial contact, efficient charge separation, and favorable band-edge alignment, enhancing its light absorption and catalytic efficiency.

Alternatively, incorporating UiO-66-NH_2 into other semiconductors can significantly enhance their H_2 generation activity. For example, Zhao *et al.* developed a visible-light-active UiO-66-NH_2@$ZnIn_2S_4$ photocatalyst by integrating UiO-66-NH_2 with flower-like $ZnIn_2S_4$ nanosheets.[79] Morphological analysis revealed that increasing the UiO-66-NH_2 content enhances the composite's surface area and pore volume, which exposes more active sites and facilitates the reactant adsorption, which ultimately boosts photocatalytic performance. The NU66/ZIS composite exhibits a noticeable red shift, indicating heterojunction formation that extends light absorption and reduces photogenerated e^-/h^+ recombination. This composite exhibited improved charge separation efficiency and achieved a hydrogen evolution rate of up to 2199 μmol h^{-1} g^{-1}. The hydrogen evolution reaction (HER) involves two main steps: hydrogen adsorption (Volmer step), followed by hydrogen formation *via* either the Heyrovsky ($H^* + H_3O^+ + e^- \rightarrow H_2 + H_2O$) or Tafel ($H^* + H^* \rightarrow H_2$) pathway. The strength of hydrogen bonding critically influences these steps, *i.e.*, if it is too weak, it slows down the adsorption process, while if it is too strong, it hampers the hydrogen formation process. To understand the superior HER performance of NU66/ZIS, DFT calculations were used to evaluate the hydrogen adsorption free energy (ΔG_{H^*}), a key descriptor for HER activity. Due to NU66's preference for proton dissociation over direct hydrogen adsorption, a proton-based model was used. The adsorption free energy of H* (G_{H^*}) on different surfaces can be calculated as,

$$\Delta G_{H^*} = \Delta E_{H^*} + \Delta ZPE - T\Delta S$$

As shown in Fig. 7g, the calculated ΔG_{H^*} on the Zr-element of NU66 and Zn, In, S elements indicates that Zr-sites in NU66 and In-sites in ZIS are the main active centers. Hence, DFT confirms this interface is favourable to help align the energy levels, and the results are consistent with HER experimental data, highlighting their pivotal role in boosting HER efficiency. Another visible light active metal sulphide, MoS_2 (MS), nanoflakes were embedded with UiO-66-NH_2 MOF by Subudhi *et al.* for H_2 and O_2 evolution under visible light exposure.[71] XPS analysis indicates that the binding energies (B.E.) of Zr, N, and O in UNH shifted to lower values, while Mo and S in MS moved to higher B.E., suggesting increased electron density on UNH and decreased density on MS, confirming electron transfer from MS to UNH after heterojunction formation. The SEM study confirms that the MS nanoflake is wrapped around the surface

of pristine UNH because of strong interfacial interaction. This configuration promotes the rapid transfer of charge carriers while concurrently lowering the charge recombination rate. The nanocomposite with 3 wt% MoS_2/UiO-66-NH_2 showed the best photocatalytic performance. This performance was significantly higher than that of the pure components, demonstrating higher surface reactive sites and the synergistic effect of the composite.

Similarly, to continue the sulfides systems, another type of Sulfide-base photocatalyst, such as CdZnS, refers to a solid solution of cadmium sulfide (CdS) and zinc sulfide (ZnS), which is a visible-light active photocatalyst with a tunable bandgap. However, it requires further modification to overcome poor charge separation ability. To address this, Yun Su's group studied the photocatalytic activity for CdZnS@UiO-66-NH_2 composites with different amounts of UNH-MOF (10, 20, 30, and 40 wt%).[73] With the increase in UNH content, the nanocomposite exhibits higher surface area and pore volume than CdZnS because of the inherent large pores of MOF, which makes reactive sites readily available for reactant adsorption. With the excellent H_2 evolution rate of 5846.5 μmol h^{-1} g^{-1}, it can be observed that improved light capture, effective charge separation, and transfer towards the surface of MOF and CdZnS are accountable for the improvement of photocatalytic activity. In another work, Hou *et al.*[67] developed a ternary UiO-66-NH_2@Au@CdS Z-scheme photocatalyst (Fig. 7h) for H_2 evolution, achieving a rate of 39.5 μmol h^{-1}, which is 2.18 times higher than UiO-66-based Z-scheme catalysts and also surpasses UiO-66-NH_2@CdS and pure CdS. The stability of the composite is confirmed by unchanged XRD patterns after 24 hours of H_2 generation. PL quenching indicates suppressed electron–hole recombination, while TRPL data reveal a significantly increased carrier lifetime (0.709 ns for UiO-66-NH_2@Au@CdS). Additionally, surface photovoltage spectroscopy reveals a much higher response for UiO-66-NH_2@Au@CdS, highlighting the Z-scheme system's effectiveness in electron–hole separation.

Defect engineering is one of the widely applicable methods in which these defects cause the property changes of the material. Since we are discussing UNH-MOFs, by creating structural defects in UNH's structure, the band structure and electronic properties can be influenced, which can be beneficial to improve photocatalytic performance. For example, Defect-engineered UiO-66-NH_2 MOFs are developed by Ma *et al.*[66] using acetic acid both as a linker and a modulator, thereby resulting in UiO-66-NH_2-*X* with different contents of structural defects. Here, *X* symbolizes the molar ratio of the modulator, with values of 0, 50, 100, 150, and 200. Pt NPs were incorporated into UNH to form Pt@UNH-*X* composite (shown in Fig. 7f). These defects enhance MOF's both specific surface area (SSA) (705 to 1057 m^2 g^{-1}) and pore volume (0.53 to 0.62). However, its pore size distribution remained retained that provide more active sites for charge carrier transport. Here, Pt acts as a co-catalyst that enhances the charge transfer and reduces e^-–h^+ recombination. The Pt@UiO-66-NH_2-100 variant achieved the maximum H_2 production rate of 381.2 μmol h^{-1} g^{-1} and retained structural stability over 10 cycles without Pt nanoparticle aggregation. In another interesting study, defect engineering is utilized by Sk *et al.* to enhance the photocatalytic efficiency of a composite consisting of NH_2-UiO-66 and ultra-thin NiCo-LDH.[68] Surface defects were introduced through controlled decarboxylation, creating NH_2-UiO-66-D (Fig. 7i). The spatial separation of NiCo-LDH nanosheets facilitated efficient electron transfer, leading to a HER catalytic performance of ~2458 μmol h^{-1} g^{-1} under visible light, 1.4 times greater than NiCo-LDH@NH_2-UiO-66. X-ray absorption spectroscopy and EPR analyses revealed that Zr^{3+} coordination on NiCo-LDH surfaces *via* NH_2 groups played a key role. Additionally, the structure showed a feasible OER overpotential of 0.96 eV, further highlighting its potential as a noble metal-free catalyst for many renewable-energy applications. Qian *et al.*[72] explored defect engineering by employing acetic acid as a modulator and subsequently carrying out post-synthetic modification. The introduced defects improved photocatalytic activity by adjusting the energy band structure, providing chelation sites to strengthen UiO-66-NH_2-*X* and CdS nanoparticle interactions, and serving as electron–hole separation sites. Among the other UiO-66-NH_2@CdS composites, the UiO-66-NH_2-150@CdS variant achieved the highest water-splitting performance, with 2.36 times greater activity than pure CdS nanoparticles.

Though UiO-66-NH_2 has shown great promise in hydrogen and oxygen evolution, its potential for photocatalytic CO_2 reduction is just as promising. The succeeding section details how various UiO-66-NH_2-based materials promote CO_2 conversion through the introduction of heterojunctions and co-catalysts.

5.2. CO_2 reduction

Increased CO_2 emissions from human activities contribute to environmental issues like global warming and atmospheric pollution.[80–82] Utilizing solar energy to convert CO_2 into value-added fuels presents a promising approach to achieving carbon neutrality and reducing emissions. However, this remains a challenging research area due to the stable linear structure of CO_2, which has a high bond enthalpy of 750 kJ mol^{-1}, hindering its adsorption and activation on the catalyst surface and thereby reducing photoconversion efficiency. Upon light irradiation, photoexcited charge carriers separate and migrate to the UNH-photocatalyst's surface, where adsorbed CO_2 interacts with photogenerated electrons (typically $2e^-$ to $8e^-$) to form CH_4, HCOOH, CO, CH_3OH, *etc.*, as shown in the eqn (4)–(7).

$$CO_2 + 2H^+ + 2e^- \rightarrow HCOOH,\ E^0\text{redox (V } \textit{vs.}\text{ NHE)} -0.61 \quad (4)$$

$$CO_2 + 2H^+ + 2e^- \rightarrow CO + H_2O,\ E^0\text{redox (V } \textit{vs.}\text{ NHE)} -0.53 \quad (5)$$

$$CO_2 + 4H^+ + 4e^- \rightarrow HCHO + H_2O,\ E^0\text{redox (V } \textit{vs.}\text{ NHE)} -0.48 \quad (6)$$

$$CO_2 + 6H^+ + 6e^- \rightarrow CH_3OH + H_2O,\ E^0\text{redox (V } \textit{vs.}\text{ NHE)} -0.38 \quad (7)$$

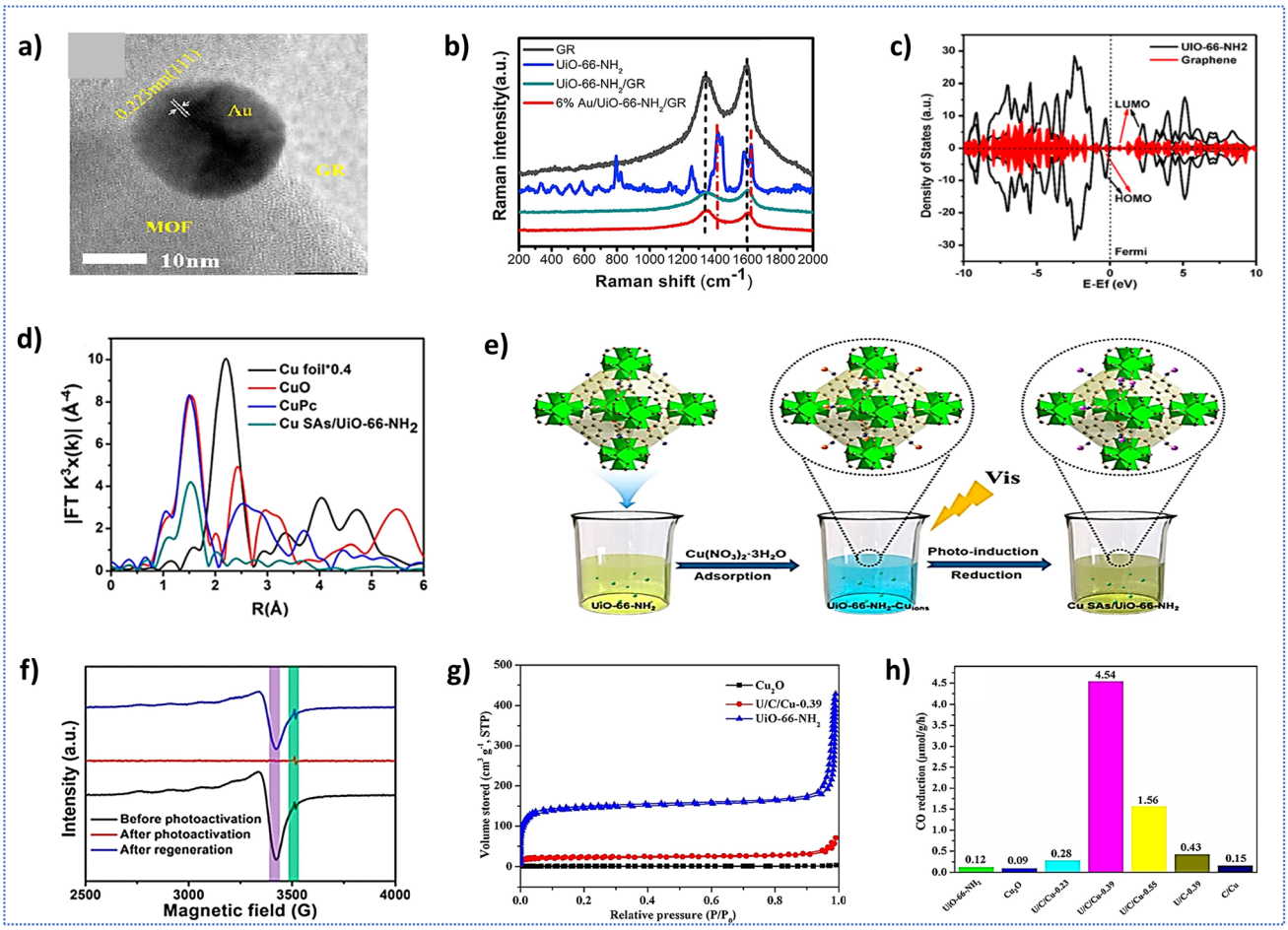

Fig. 8 (a) HRTEM of the composite Au/UiO-66-NH_2/GR, (b) Raman spectra of UiO-66-NH_2 and Au/UiO-66-NH_2/GR, (c) density of states of UiO-66-NH_2 and graphene, respectively, reproduced with permission from Elsevier. Copyright © 2021.[85] (d) EXAFS results of the composites. (e) Synthesis route of the Cu SAs/UiO-66-NH_2 photocatalyst. C (grey), O (red), Zr–O clusters (green), N (blue), Cu ions (orange), and Cu SAs (purple), (f) low-temperature X-band EPR spectra of Cu SAs/UiO-66-NH_2, reproduced with permission from American Chemical Society. Copyright © 2020.[86] (g) N_2 adsorption–desorption isotherms of Cu_2O, U/C/Cu-0.39 and UiO-66-NH_2, (h) the corresponding CO yields for different photocatalysts, reproduced with permission from Elsevier. Copyright © 2021.[87]

Following this mechanism, studies have focused on UNH MOF with other semiconductors and noble metal catalysts for converting CO_2 into gases like carbon monoxide and methane.[73,83–85] The presence of –NH_2 groups in UNH not only enhances the CO_2 adsorption capacity of the MOF but also contributes to a reduction in its band gap, thereby improving overall photocatalytic efficiency. Additionally, plasmonic noble metals such as Au have been reported to further enhance light absorption and show great potential as photocatalysts for CO_2 reduction. Hence, a hydrothermal approach was utilized by X. Wang group to generate Au/UiO-66-NH_2/GR ternary composite successfully.[85] Firstly, the GR was introduced, and then, for the deposition of Au-NPs, a photoreduction process was employed. The HRTEM image, as displayed in (Fig. 8a), clearly reveals lattice fringes with 0.223 nm of interplanar distance, corresponding to metallic Au nanoparticles' (111) lattice space and the particle size distribution reveals that spherical Au-NPs (3–33 nm in diameter) are anchored on UiO-66-NH_2 and GR's surfaces. Further information can be observed from the HRTEM and EDX images that effectively integrate Au, UiO-66-NH_2, and GR and distinctly demonstrate the successful formation of a nanocomposite that comprises the elements C, N, O, Zr, and Au. The Raman peak of UN/GR becomes broader and less intense as the Au content increases from 2% to 6%, as clearly observed in the Raman spectra (Fig. 8b). This can be attributed to the fact that higher Au content may disrupt the chemical environment of graphene, indicating stronger interfacial interaction and improved charge dispersion within the MOF composite. Density Functional Theory (DFT) is a vital computational method for exploring the electronic structure and charge dynamics in many-electron systems. Hence to understand electron transfer between UiO-66-NH_2 and graphene, DFT calculations of their density of states were done and as shown in Fig. 8c, both materials have HOMOs near the Fermi level, but graphene's LUMO is much closer that suggests preferential electron transfer from UiO-66-NH_2 to graphene. The close contact achieved from the *in situ* growth process significantly boosts photocatalytic activity by enhancing the interfacial

contact between UiO-66 NH_2 and GR. This leads to better charge separation and superior photocatalytic output. The mechanism of CO_2 reduction process involves with the e^- transfer from UiO-66-NH_2 to CO_2, forming a bent CO_2 bidentate. Next, an electron and proton transfer to C, forming $HCOO^-$, followed by a second proton transfer, breaking an O–Zr bond and protonating the O atom to give HCOOH as the final product. As indicated in the below eqn (8)–(10).

$$CO_2 + e^- \rightarrow CO_2^- \quad (8)$$

$$CO_2^- + H^+ + e^- \rightarrow HCOO^- \quad (9)$$

$$HCOO^- + H^+ \rightarrow HCOOH \quad (10)$$

Due to the distinctive SPR effect of Au NPs, the composite exhibited a significant absorption of visible light and a Raman spectral shift. Among the several samples, the 6% Au/UiO-66-NH_2/GR had the optimal CO_2 activity with selectivity. The increased photocatalytic efficiency was attributed to the high SSA and large pore volume of UiO-66-NH_2, and the plasma excitation of Au-NPs may increase the visible light harvesting intensity and prolong the visible light-absorption range. The GR sheets have exceptional electron acceptance and transfer capabilities, which could facilitate charge separation and speed up the movement of charge carriers on GR. In addition, GR could improve UiO-66-NH_2's dispersibility, which would improve CO_2 reduction.

Although noble metals efficiently enhance UiO-66-NH_2 photocatalysis by improving light absorption and charge transfer, their high-cost limits large-scale use. To address this, P. Zhu *et al.* fabricated a cost-effective bimetallic UiO-66-NH_2 (Zr/Ni) by integrating Ni^{2+} into the framework.[88] The Ni^{2+}-doped samples showed strong photocatalytic performance, producing CO at 9.01 μmol g^{-1} h^{-1}, which is 2.46 times higher than the CO yield of pristine UiO-66-NH_2. Characterization data revealed an average particle size of 93.50 nm for UN and 51.90 nm for 0.5Ni-UNH, and the 0.5Ni-UNH sample exhibited reduced crystallinity and irregular-shaped particles, likely due to aggregation affecting both crystallinity and particle size. The CO_2 adsorption isotherm indicates that the 0.5Ni-UNH exhibits a greater CO_2 adsorption capacity than UNH, which is attributed to the formation of unsaturated metal active sites resulting from Ni^{2+} doping. Furthermore, DFT studies were also conducted to investigate the effect of Ni^{2+} doping on the electronic structure of UNH. The PDOS results for both UN and 0.5Ni-UN reveal that, near the Fermi level, the density of electronic states in the doped system is significantly higher than that of pristine UN, which suggests improved conductivity and charge carrier availability. Additionally, the Ni^{2+} d-orbitals also contribute to both the HOMO and LUMO states. As a result, Ni^{2+} doping effectively modifies the band gap of UiO-66-NH_2, thereby tuning its electronic structure and enhancing its absorption of visible light. The proposed mechanism for photocatalytic CO_2 reduction using Ni^{2+}-doped UiO-66-NH_2 begins with the visible-light excitation of ATA and the photosensitizer $[Co(bpy)_3]^{2+}$, generating electrons. The photosensitizer extends the light absorption range and facilitates electron generation and transfer. These photogenerated electrons preferentially transfer from excited $[Co(bpy)_3]^{2+}$* and ATA to Ni^{2+} due to its higher electron affinity compared to Zr^{4+}, forming Ni^+–O–Zr^{4+} species within the $(Ni/Zr)_6O_4(OH)_4$ bimetallic cluster. A subsequent metal-to-metal charge transfer (MMCT) then occurs, where electrons move from Ni^+ to Zr^{4+}, reducing it to Zr^{3+}. These Zr^{3+} sites act as active centers for the reduction of CO_2 to CO. The oxidized $[Co(bpy)_3]^{3+}$ is regenerated by triethanolamine (TEOA), completing the redox cycle. Ni^{2+} serves as an effective electron mediator, enhancing charge separation and transfer throughout the MOF structure. The synergistic interaction between Ni and Zr in the bimetallic center promotes MMCT and facilitates selective CO_2 activation, significantly improving the photocatalytic performance of UiO-66-NH_2 for CO production under visible light. However, single-atom nanoparticles can reveal more active catalytic sites and use more atoms than typical metal particles, which can be helpful in enhancing the photocatalytic activity of MOF. Hence, G. Wang employed a photoinduction method to develop a composite of Cu single atoms (Cu SAs) with UiO-66-NH_2 (Fig. 8e), which serves as an efficient photocatalyst for CO_2 photoreduction.[86] EXAFS analysis (Fig. 8d) revealed a prominent peak at 1.50 Å that matches the first coordination sphere of Cu–N, with no peak for Cu–Cu interactions. Isolated Cu atoms were coordinated with 2 N-atoms with a 1.97 atomic distance in the UiO-66-NH_2 matrix. DFT studies revealed that Cu SAs which is coordinated with two vicinal amino groups in UiO-66-NH_2 reduce the band gap and lowers the Fermi level, promoting electron accumulation and significantly improved the photocatalytic CO_2 reduction performance. The Cu SAs/UiO-66-NH_2 composite successfully converted CO_2 into CH_3OH and C_2H_5OH using solar energy at rates of 5.33 and 4.22 μmol h^{-1} g^{-1}, respectively, outperforming both pristine UiO-66-NH_2 and Cu nanoparticle/UiO-66-NH_2 composites. Low-temperature X-band EPR spectra in Fig. 8f demonstrate the regeneration of Cu after light irradiation, supporting valence changes of Cu during photocatalysis. These findings underscore the remarkably improved transfer and separation capability attained with Cu SAs, which are essential for enabling CO_2 reduction. Cyclic tests confirm the stability of Cu SAs/UiO-66-NH_2 over 4 cycles without a drop in its activity or changes in crystal structure, emphasizing the catalyst's durability and potential for sustainable CO_2 reduction applications.

In another Cu-based system, by coupling Cu, Cu_2O, and UiO-66-NH_2, photodegradation of CO_2 was studied by Zhao *et al.*[87] to fabricate a UiO-66-NH_2/Cu_2O/Cu indirect Z-scheme heterojunction by a hydrothermal approach. XPS analysis revealed increased electron cloud for Zr and N and a decrease for Cu, which indicates strong electronic exchange between UiO-66-NH_2, Cu, and Cu_2O. Here, Cu and Cu_2O act as electron donors while Zr is the electron acceptor in the case of U/C/Cu-0.39 composite. The BET analysis (Fig. 8g) shows the specific surface areas of UiO-66-NH_2, Cu_2O, and the U/C/Cu-0.39 composite. The inherently large surface area of UiO-66-NH_2 contributes to the increased SSA of the composite compared to pristine Cu_2O, thereby enhancing CO_2 adsorption. Cu derived

from Cu_2O acts as an e- carrier in the indirect Z-scheme heterojunction. This heterojunction demonstrated superior photocatalytic capability in CO_2 reduction to CO, achieving a CO yield of 4.54 μmol g^{-1} h^{-1} (Fig. 8h). The improved activity was attributed to three key factors: suitable band structures enable the Z-scheme heterojunction, UiO-66-NH_2 reduces the photocorrosion of Cu_2O and enhances CO_2 adsorption, and Cu facilitates the charge carrier migration and supplies reactive sites for reduction of CO_2. Another novel Z-scheme heterostructure comprising oxygen-defective ZnO (O–ZnO), rGO, and UiO-66-NH_2 (denoted OZ/R/U) was synthesized by Meng *et al.* to enhance visible-light-driven photo reduction of CO_2.[89] This ternary composite leverages the high surface area and visible-light responsiveness of UiO-66-NH_2, the conductivity of rGO, and oxygen vacancies in O–ZnO to facilitate charge separation and improve activity. XRD confirmed the crystalline integrity of O–ZnO and UiO-66-NH_2, while Raman and ESR analyses verified oxygen vacancies and rGO incorporation. SEM and TEM showed uniform distribution of O–ZnO and UiO-66-NH_2 on rGO, enhancing interfacial contact and charge transfer pathways. Photocatalytic tests yielded methanol and formic acid at rates of 34.83 and 6.41 μmol g^{-1} h^{-1}, respectively, outperforming other combinations. The Z-scheme mechanism enabled efficient electron transfer from O–ZnO to UiO-66-NH_2 *via* rGO, reducing charge recombination while maintaining redox potential. This study highlights the potential of UiO-66-NH_2-based Z-scheme heterojunctions for sustainable CO_2 reduction and suggests further optimization of oxygen vacancies and rGO content to enhance performance.

Apart from composites with the above noble and transition metals, some researches also focused on integrating MOFs with organic semiconductors to further improve light absorption and charge transfer capabilities. In particular, graphitic carbon nitride (g-C_3N_4), a metal-free semiconductor with its π-conjugated structure and visible-light responsiveness, has emerged as a highly effective choice for constructing efficient photocatalytic systems. Wang *et al.* used the holey g-C_3N_4 (HGN) with a rich amino group (–NH_x) to hybridize with NH_2-UiO-66 (NUZ) by an *in situ* growth synthesis method that shows excellent CO_2 photoreduction efficiency of 31.6 μmol g^{-1} h^{-1}.[90] It is evident from FT-IR data that for NH_x-rich HGN, the peak N–H intensity significantly increased. A significant reduction in intensity was observed following hybridization, suggesting the existence of a chemical interaction between NUZ and HGN. NUZ/HGN heterostructures were created through NH_x–Zr–O bonding, which forms a bond between the –NH_x sites as hot spots and NUZ. These hot areas allowed NUZ nanocrystals to be anchored on the HGN surface, achieving uniform dispersion and limiting NUZ leaching. In the meantime, due to the bond interaction and multiple light scattering between NUZ and HGN, this distinct hybridization enhanced light absorption. In addition to their high activity, the nanocomposites exhibited good stability, which is consistent with CO_2 photoreduction stability because the strong association effectively fixed the NUZ nanoparticles, thus preventing NUZ from leaching. Photocatalytic performance summary of UiO-66-NH_2-based photocatalysts for CO_2 reduction has been detailed in Table 3.

Another highly active $CsPbBr_3$ QDs/UiO-66(NH_2) nanocomposites are successfully manufactured by S. Wan's group *via* an easy ultrasonic hybrid method.[91] The HRTEM confirms that the crystallinity and size of the $CsPbBr_3$ QDs remained unchanged, which reflects that it can absorb light efficiently and maintain optimal charge transport. Still, compared to pure $CsPbBr_3$-QDs and UiO-66(NH_2)-MOF, the resulting nanohybrids showed noticeably increased CO_2 photoreduction activity under visible light. It is found that 15 wt% is the ideal loading content for $CsPbBr_3$ QDs and that 98.57 mol g^{-1} is the appropriate CO product rate. The quick charge dissociation and migration at the junction between $CsPbBr_3$ QDs and UiO-66(NH_2) composites is responsible for the remarkably increased photocatalytic response. Furthermore, the elevated light absorption capacity and suitable specific surface area account for the high activity of the UiO-66(NH_2) nanojunction and $CsPbBr_3$ QDs. Additionally, the $CsPbBr_3$ QDs/UiO-66(NH_2) nanocomposites demonstrated strong recyclability when used in high-performance CO_2 reduction applications.

Polymers are widely used in various applications, including photocatalysis, due to their tunable properties, excellent conductivity, and stability. Their ability to integrate with other semiconducting materials makes them ideal for enhancing the overall composite's performance. Xiaojun Wang and team integrate poly(triphenylamine) (PTPA) with UiO-66-NH_2 to form a hybrid composite, designed to address the limitations of MOF-based photocatalysts in CO_2 reduction under visible light.[76] This composite synergistically combines the high porosity and catalytic activity of UiO-66-NH_2 with the electron-conductive properties of PTPA, resulting in a honeycomb-like structure as observed in SEM and TEM analyses. Photoluminescence studies revealed suppressed charge recombination, corroborated by extended carrier lifetimes and enhanced photocurrent response, with an 11-fold improvement over pristine UiO-66-NH_2. The composite achieved notable CO_2 reduction activity, with a maximum HCOOH yield of 3.06 μmol, and demonstrated exceptional stability over 6 cycles, *i.e.*, retaining 90% of its activity. The study highlights the potential of PTPA-functionalized UiO-66-NH_2 in photocatalytic applications while suggesting further research on optimizing polymer loadings and exploring alternative conjugated frameworks for improved scalability and efficiency. In a similar way, the PET@NH_2-UiO-66 composite was developed by Li *et al.* by hydrothermally anchoring NH_2-UiO-66 particles (~1.12 μm) onto polyethylene terephthalate (PET) fibers, transforming powdered MOFs into robust films with enhanced stability and reusability.[95] Characterization *via* SEM, PXRD, and FTIR confirmed uniform MOF coating, structural integrity, and strong hydrogen bonding at the interface, which mitigates particle detachment commonly seen in film systems. The composite demonstrated superior CO_2 photoreduction under visible light, achieving CO and CH_4 yields of 1485 μL g^{-1} and 390 μL g^{-1}, respectively, without requiring sacrificial agents. Notably, the composite maintained >90% activity over six cycles (60 hours), demonstrating excellent stability and adhesion, as confirmed by post-reaction SEM and XRD analyses. However, challenges such as scalability, cost of Zr-based MOFs, and

Table 3 Summary of UiO-66-NH_2-based photocatalysts for CO_2 reduction

Sl no.	Material	Synthesis method	S_{BET} ($m^2\ g^{-1}$)	Light source	Photocatalytic activity	Ref.
1	NH_2-UiO-66	Hydrothermal (120 °C for 24 h)	778	500 W Xe lamp, 800 nm > λ > 420 nm	1.32 μmol h^{-1} (HCOOH)	27
2	Ni-doped UN	Solvothermal (120 °C for 24 h)	782.49	300 W xenon lamp with a 420 nm cut-off filter	9.01 μmol g^{-1} h^{-1} (CO)	88
3	$Cd_{0.2}Zn_{0.8}S$@UiO-66-NH_2	Solvothermal (160 °C for 4 h)	266	300 W xenon lamp with a UV cut-off filter (λ > 420 nm)	6.8 μmol g^{-1} h^{-1} (CH_3OH)	73
4	$CsPbBr_3$ QD/UN	Ultrasonic hybrid approach (for 30 min)	465.68	300 W Xe lamp with a UV-cut filter (420 nm)	98.57 μmol g^{-1} (CO)	91
5	UN/HOLEY g-C_3N_4	Hydrothermal (120 °C for 12 h)	335	300 W Xe arc lamp, λ > 400 nm	31.6 μmol g^{-1} h^{-1} (CO)	90
6	UN/GO	Solvothermal method (120 °C for 24 h)	1052	—	6.41 mmol g^{-1} (CO_2 adsorption)	92
7	Au/UiO-66-NH_2/graphene	Photoinduction followed by hydrothermal	604	300 W Xe lamp, λ > 400 nm	49.9 μmol (CO_2 reduction) 40.4 μmol (HCOOH)	85
8	ZnO/reduced GO/UiO-66-NH_2	Solvothermal (120 °C for 48 h)	877.3	300 W Xe lamp, λ > 420 nm	34.83 μmol g^{-1} h^{-1} (CH_3OH) 6.41 μmol g^{-1} h^{-1} (HCOOH)	89
9	UiO-66-NH_2/Cu_2O/Cu	Hydrothermal (120 °C for 12 h)	68.62	300 W Xe lamp	4.54 μmol g^{-1} h^{-1}	87
10	Cu SAs/UN	Photoinduction method	856.5	300 W Xe lamp, λ > 400 nm	5.33 μmol g^{-1} h^{-1} (CH_3OH) 4.22 μmol g^{-1} h^{-1} (C_2H_5OH)	86
11	TiO_2/NH_2-UiO-66	Reflux method	202	150 W Xe arc lamp, λ > 325 nm	4.24 μmol g^{-1} h^{-1} (CO)	93
12	NH_2-UiO-66/Au/In_2O_3	Solvothermal method (120 °C for 12 h)	348.3	300 W Xe lamp, λ > 400 nm	8.56 μmol g^{-1} h^{-1} (CO)	94
13	PET@NH_2-UiO-66	Hydrothermal (100 °C for 4 h)	—	300 W Xe lamp, λ > 400 nm	1485 μL g^{-1} (CO) and 390 μL g^{-1} (CH_4)	95
14	PTPA/UIO-66-NH_2	Solvothermal method (120 °C for 24 h)	333.5	300 W Xe lamp, λ > 400 nm	3.06 μ mol (HCOOH)	76
15	TiO_2/NH_2–UiO-66	Microwave method (80 °C for 1 h)	170	λ > 325 nm, 150 W UV-vis light	1.8 μmol g^{-1} h^{-1} (CO)	83

intrinsic electrical resistance of NH_2-UiO-66 limit large-scale application, suggesting the need for conductive additives or alternative earth-abundant metal MOFs. Additionally, the impact of H_2O_2 accumulation on long-term selectivity and stability requires further investigation. This study establishes PET@NH_2-UiO-66 as a promising and durable photocatalyst for CO_2 reduction, emphasizing the potential of flexible MOF-based systems for sustainable energy applications.

5.3. Cr(VI) reduction

One of the most dangerous contaminants found in water bodies is hexavalent chromium (Cr(VI)), which has raised significant concern throughout the world. The primary cause of pollution is specifically Cr(VI) from the discharge of industrial wastewater, which can cause cancer when it enters human bodies. Thus, using photocatalysts to reduce the highly toxic Cr(VI) to low-toxic Cr(III) is one of the most efficient water treatment techniques. The photoreduction of Cr(VI) typically takes place in CB region of a semiconductor with more -ve potential than the Cr(VI)/Cr(III) redox potential. Thus, the main processes can be described as follows (eqn (11) and (12)):

$$\text{Photocatalyst} + h\nu \rightarrow h^+ + e^- \quad (11)$$

$$Cr_2O_7^{2-} + 14H^+ + 6e^- \rightarrow 2Cr^{3+} + 7H_2O \quad (12)$$

The use of noble metals with MOFs is an efficient method to enhance the photoactivity of the semiconductors. Pd improves the charge separation of the material because of its electron trapping ability that can be very helpful to improve MOFs photocatalytic efficiency. Following this, Shen *et al.* synthesized Pd@UiO-66-NH_2 *via* a facile one-pot hydrothermal method where Pd is uniformly dispersed over the MOF surface.[49] The XPS data (Fig. 9a–d) reveal that the binding energies for Zr 3d and Pd 3d in the used sample are almost identical to those in the fresh sample, demonstrating the sample's excellent chemical stability during the reaction process. Notably, the narrow scan spectra of Cr 2p display a weak peak at 577.1 eV, corresponding to Cr(III). Additionally, this weak Cr 2p peak indicates that Cr^{3+} can be effectively removed by simply washing the sample with deionized water. As shown in Fig. 9e, the transient photocurrent response of Pd@UiO-66(NH_2) signifies the improved separation efficiency of e^-/h^+ pairs and the lifetime of the photogenerated charge carriers, further confirmed by decreased PL peaks. In addition to that, this work shows that without any sacrificial agents, even after 3 cycles of use, the material retains its high reusability by showcasing the durability of the composite. Pd@UiO-66(NH_2) exhibits better performance than that of UiO-66(NH_2), achieving a 99% reduction within 90 minutes under visible light ($\lambda \geq 420$ nm). The robust Pd–UiO-66(NH_2) interface enhances charge separation, boosting the activity of Pd@UiO-66(NH_2). In conclusion, prolonged charge carrier lifespans, observed through photocurrent and PL analyses, along with improved light absorption, surface area, and charge separation, these properties explain its superior photoactivity. Similarly, Ag/UiO-66-NH_2 as a photocatalyst was developed by W. Zhang's group for the reduction of Cr(VI) driven by visible light.[96] The UV-vis DRS spectra

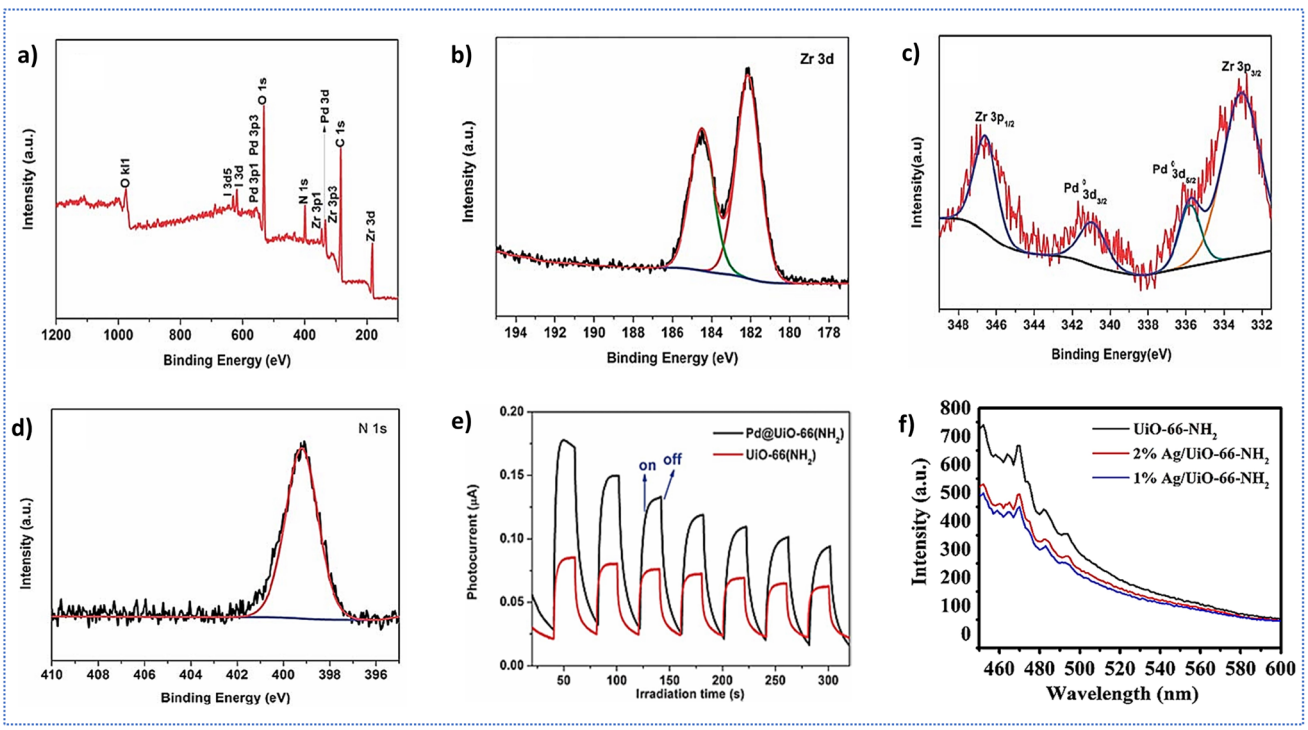

Fig. 9 (a)–(d) XPS spectra of Pd@UiO-66(NH_2), (e) transient photocurrent response of UiO-66(NH_2) and Pd@UiO-66(NH_2), reproduced with permission from The Royal Society of Chemistry. Copyright © 2013.[49] and (f) PL spectra of UiO-66-NH_2, 1% Ag/UiO-66-NH_2, and 2% Ag/UiO-66-NH_2, reproduced with permission from Springer. Copyright © 2019.[96]

highlighted that the addition of Ag nanoparticles results in a slight increase in absorption intensity within the visible region of the spectrum, indicating the formation of a modest LSPR absorption from Ag nanoparticles.

The decreased intensity of photoluminescence spectra produced at 350 nm after Ag loading indicated an enhanced charge separation capability (Fig. 9f). This is likely due to the creation of a Schottky junction between Ag and UiO-66-NH_2, which is crucial in preventing charge recombination. The lowest photocurrent intensity of pure UiO-66-NH_2 resulted in the fastest rate of e^-/h^+ recombination, which also explains its low photocatalytic activity. However, after adding Ag nanoparticles, the composite's photocurrent intensity significantly increased. The photocatalytic response of the composite is increased because the electrons in UiO-66-NH_2 are charged and move through a Schottky circuit to Ag under visible light exposure. An increased Cr(VI) reduction efficiency is the result of better electron–hole separation. It can be observed that excess Ag loading causes a decrease in separation efficiency due to complex formation between Cr(III) and $-NH_2$, but it also leads to a steady reduction rate of Cr(VI). In another study, a ternary Ag/AgCl/NH_2-UiO-66 heterojunction was designed by Zhang *et al.* to minimize Cr(VI) *via* a simple solvothermal technique.[97] The band gap of NH_2-UiO-66 and Ag/AgCl/NH_2-UiO-66 (Fig. 10a) reduces significantly to 2.91 and 2.83 eV, respectively, compared to UiO-66 MOF. Therefore, it can be said that the introduction of the $-NH_2$ group and Ag/AgCl improves the light absorption ability and stronger photoexcited charge carriers. TRPL data reveal average charge carrier lifetimes of 0.79 ns for UiO-66, 0.92 ns for Ag/AgCl/UiO-66, 0.89 ns for NH_2-UiO-66, and 2.98 ns for Ag/AgCl/NH_2-UiO-66 that suggests the e^- – trapping ability of Ag is responsible for suppressing the recombination process and thus improve the Cr(VI) photoreduction. The synthesized catalyst's Cr(VI) reduction efficiency under visible-light illumination was 1.7 times more than UiO-66 because of its stable structure and superior photocatalytic activity. Concurrently, Ag's SPR effect improved the e^-/h^+ separation efficiency and dramatically expanded the light response range.

Single MOFs suffer rapid electron–hole recombination, but metal doping addresses this *via* metal-to-metal charge transfer (MMCT), reducing recombination and increasing surface area for more active catalytic sites.[101] Y. Gao and his colleagues produced Ti_α–$Zr_{1-\alpha}$–UiO-66-NH_2 catalyst using a Ti-metal ion doping method.[102] The XRD and SEM results show that samples with the right amount of Ti-doping wouldn't cause morphology change, while the excess amount of Ti doping in the samples can lead to the structure adopting an irregular shape, which explains the successful doping of Ti on Zr-UiO-66-NH_2. Additionally, the findings of the DFT calculations indicate that the Ti_α–$Zr_{1-\alpha}$ cluster plays a major role in enhancing and facilitating the generation of optoelectronic properties. Electron transfer occurs from the 2p – orbitals of $Zr_{0.6}$–$Ti_{0.4}$ and nitrogen

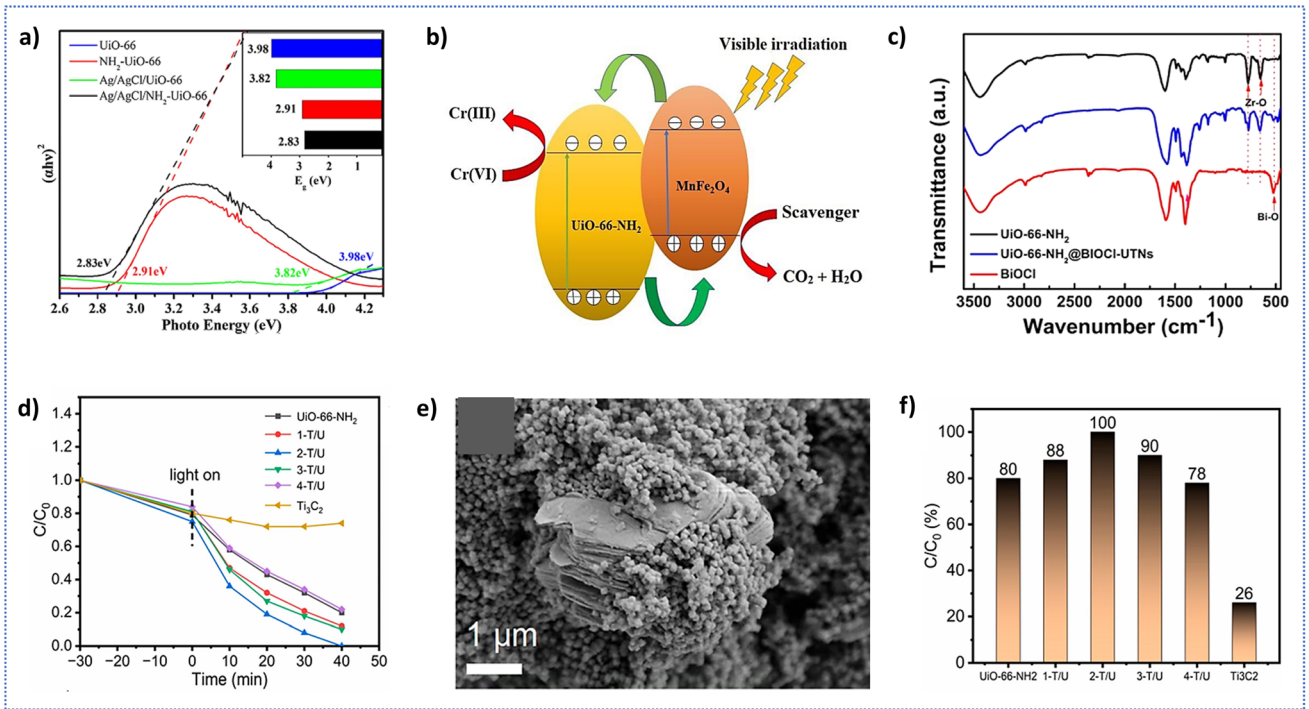

Fig. 10 (a) Band gap measurements of UiO-66, Ag/AgCl/UiO-66, NH_2-UiO-66, and Ag/AgCl/NH_2-UiO-66, reproduced with permission from Elsevier. Copyright © 2019.[97] (b) Schematic representation of the proposed photocatalytic mechanism for Cr(VI) reduction, reproduced with permission from Elsevier. Copyright © 2019.[98] (c) FTIR spectra of pure UiO-66-NH_2, BiOCl, and the UiO-66-NH_2@BiOCl-UTN composite, reproduced with permission from American Chemical Society. Copyright © 2021.[99] (d and f) Removal of $Cr_2O_7^{2-}$ by Ti_3C_2, UiO-66-NH_2, and composites 1-T/U, 2-T/U, 3-T/U, and 4-T/U, (e) SEM image of the 1-T/U composite. Reproduced with permission from MDPI. Copyright © 2023.[100]

atoms to the O-2p orbital, significantly boosting electron transport activity. The charge transfer mechanism involves two parts: metal-to-metal charge transfer (MMCT) and ligand-to-metal charge transfer (LMCT). Upon light absorption by the NH_2 group, electrons become excited and are transferred to the Zr–O bond *via* LMCT. Subsequently, a portion of the photoinduced electrons reduces Cr(VI) to Cr(III), while the remaining electrons migrate from Zr–O to Ti–O through the MMCT process. Hence, the Ti – doping effectively increases the normalized surface area and exposes more reactive sites for photocatalysis. In addition to encouraging the transfer of photogenerated carriers, the MMCT process from Zr to Ti also inhibits their recombination. In a polluted system, the adsorption of Ti–Zr–UiO-66-NH_2 towards Cr(VI) was 80.9%, which is greater than Zr-UiO-66-NH_2 alone. A detailed list of the photocatalytic performance of UiO-66-NH_2-based nanohybrids has been presented in Table 4.

Similarly, $MnFe_2O_4$ is an excellent choice for chromium separation from water because of its superior saturation magnetization compared to other ferrites. Its recovery is straightforward using an external magnetic field, and it boasts strong chemical stability, high symmetry, enhanced biocompatibility, electrical resistance, and distinct crystalline properties. Hence, Khosroshahi and coworkers used the solvothermal technique to study the photocatalytic Cr(VI) reduction activity with the UiO-66-NH_2/$MnFe_2O_4$ composite.[98] When $MnFe_2O_4$ was added the BET surface area was decreased to 531 $m^2\ g^{-1}$, which is less than that of UiO-66-NH_2. Despite the drop in surface area, its mesoporous nature with increased pore diameter (174.96 Å) allows easy diffusion of Cr(VI) ions into active sites, leading to better interaction between the pollutant and the catalyst. Zeta potential analysis indicates that at pH = 2, the composite shows a positive surface charge that enhances Cr(VI) adsorption *via* strong electrostatic attraction. Hence, the composite demonstrated 100% Cr(VI) reduction at pH = 2 within 75 min, and the magnetic property of $MnFe_2O_4$ allows the composite catalyst to be quickly and easily separated from water using an external magnet after the photocatalytic reaction. The photoreduction mechanism can be explained as follows: upon visible light exposure, the UiO-66-NH_2/$MnFe_2O_4$ composite absorbs photons and generates electron–hole (e^-/h^+) pairs on the surface of the photocatalyst. As shown in (Fig. 10b), due to the higher redox potential of $MnFe_2O_4$, electrons transfer from the CB of $MnFe_2O_4$ to the CB of UiO-66-NH_2, leading to e^- accumulation in UiO-66-NH_2. These electrons reduce $Cr_2O_7^{2-}$ to Cr^{3+}, thereby driving the Cr(VI) photoreduction process. Meanwhile, the holes (h^+) accumulated in $MnFe_2O_4$'s VB oxidize the H_2O molecules, producing reactive hydroxyl radicals ($2H_2O \rightarrow O_2 + 4H^+ + 4e^-$) and oxygen ($H_2O + h^+ \rightarrow {}^{\bullet}OH + H^+$). These highly reactive $^{\bullet}OH$ radicals attack organic hole scavengers (*e.g.*, pollutants), ultimately degrading them into CO_2 and H_2O. The $MnFe_2O_4$ plays a synergistic role, enhancing charge separation and promoting oxidation reactions, while the UiO-66-NH_2 ensures a high surface area and light absorption. This spatial charge separation minimizes recombination, leading to efficient photocatalytic performance. It is worth mentioning that the photoreduction reaction time and the straightforward

Table 4 Summary of UiO-66-NH_2-based photocatalysts for Cr(VI) degradation

Sl no.	Material	Synthesis method	S_{BET} ($m^2\ g^{-1}$)	Light source	Photocatalytic activity	Ref.
1	Pd@ UiO-66-NH_2	Hydrothermal (180 °C for 1.5 h)	836.6	300 W Xe lamp with a 420 nm cut-off filter	99% in 90 min	49
2	Ti-doped Zr-UiO-66-NH_2	Solvothermal (120 °C for 48 h)	661.87	300 W Xe lamp	99.8% in 120 min	102
3	g-C_3N_4/NH_2-UiO-66 (Zr)	Solvothermal (120 °C for 48 h)	—	300 W Xe lamp with 420 nm filter	100% within 90 min	103
4	UN/$MnFe_2O_4$ QD	Solvothermal (120 °C for 24 h)	531	300 W Xe lamp	100% in 75 min	98
5	UN@ BiOCl	Room temp. (25 °C for 5 h)	511	300 W Xe lamp with 420 nm filter	97% in 25 min	99
6	Ag/AgCl/UiO-66-NH_2	UV light reduction	—	300 W Xe lamp with 420 nm filter	74.2% in 150 min	97
7	Fe_3O_4@UiO 66-NH_2	*In situ* solvothermal (120 °C for 24 h)	572.13	300 W Xe lamp	Cr(VI) adsorption (743 mg g^{-1})	70
8	Ti_3C_2/UN	Solvothermal (120 °C for 24 h)	—	300 W Xe lamp, with a L42 light cutter for 40 min	100% in 40 min	100
9	Ag/UiO-66-NH_2	Room temp (120 °C for 12 h)	—	300 W Xe lamp with 420 nm filter	90%	96

synthesis method of the UiO-66-NH_2/$MnFe_2O_4$ catalyst outperform most of the other MOFs.

Layered materials can provide more accessible active sites for Cr(VI) adsorption. For example, Hussain *et al.* synthesized UiO-66-NH_2@BiOCl nanocomposite using BiOCl nanosheets over UiO-66-NH_2 MOF at room temperature *via* a simple *in situ* synthesis method.[99] HRTEM image confirms that each UiO-66-NH_2 nanoparticle was entirely encapsulated by BiOCl ultrathin nanoplates, maintaining mechanical and electrical integrity that facilitates the uniform dispersion of Cr(VI) for the effective photoreduction process to occur. The FT-IR (Fig. 10c) absorption band at 524 cm^{-1} confirms the presence of Bi–O bonds within the composite, while absorption peaks between 600−800 cm^{-1} indicate the Zr–O bonding in the MOF material. This suggests that BiOCl and UiO-66-NH_2 exist as separate entities but are securely integrated into the UiO-66-NH_2@BiOCl-UTNs composite. It can be attributed to BiOCl, which has a built-in electric field that facilitates the charge transport process, and its nanosheet morphology further provides an exposed surface area for the adsorption of pollutants. The heterogeneous nanocomposites performed better than individual BiOCl and UiO-66-NH_2 towards Cr(VI) reduction under the visible light spectrum. In particular, the composite (containing a Bi^{3+} mole ratio of 5 mM) demonstrated superior performance compared to other composites in photocatalytic Cr(VI) reduction, which was attributed to the combined influence of BiOCl and UiO-66-NH_2, which effectively separated photogenerated electron–holes while inhibiting their recombination.

MXenes are another type of 2D-class materials known for their excellent electrical conductivity and abundant uncoordinated metal sites that can form close contacts with UNH-MOFs, hence enhancing charge separation and enabling efficient photocatalytic applications. He and coworkers utilized an *in situ* solvothermal technique to create Ti_3C_2/UiO-66-NH_2 nanohybrids for the photoreduction process of Cr(VI) by varying the ratio between Ti_3C_2 and UiO-66-NH_2.[100] UiO-66-NH_2 nanoparticles were distributed across the surface and slits of Ti_3C_2, while the structure of both UiO-66-NH_2 and Ti_3C_2 was preserved in the as-synthesized nanocomposites (Fig. 10e) as shown in SEM images. The N_2 sorption isotherm indicates that the material is highly porous, which enhances its capacity to concentrate pollutants and collect light. The optimal Ti_3C_2/UiO-66-NH_2 with 10 wt% Ti_3C_2, 2-T/U, had the best photoreduction efficiency, eliminating 100% of the $Cr_2O_7^{2-}$ in 40 minutes (Fig. 10d and f). The photoreduction rate is found to be 0.0871 min^{-1} (almost 2.6 times higher than the pristine UiO-66-NH_2), and the photoreduction kinetics of $Cr_2O_7^{2-}$ by 2-T/U were also investigated by using the above-mentioned data. The formation of a heterojunction between Ti_3C_2 and UiO-66-NH_2 may be the cause of the significantly faster Cr(VI) reduction rate of 2-T/U, which may be attributed to the increased separation of charge carriers.

Yuan *et al.* successfully introduced porphyrin (TCPP) into UiO-66-NH_2 *via* a solvothermal method for Cr(VI) photodegradation.[104] The 15 mg TCPP-modified UiO-66-NH_2 (15-UNT) significantly improved light absorption and exhibited a 10-fold higher Cr(VI) reduction rate than pristine UiO-66-NH_2, achieving complete removal within 80 minutes. Due to its higher number of carboxyl groups in TCPP compared to ATA, it is more prone to protonation, facilitating the adsorption of negatively charged $Cr_2O_7^{2-}$. Under visible light, electron transfer from TCPP to the Zr–O cluster enhances charge carrier separation, promoting Cr(VI) reduction. FTIR analysis for the modified system confirmed the successful incorporation of TCPP into UiO-66-NH_2 (UNH), as indicated by the disappearance of the 1722 cm^{-1} peak due to coordination between –COOH and metal ions. In addition to that, XPS analysis of 15-UNT before and after Cr(VI) removal under visible light showed peaks for both Cr(III) (576.9, 586.7 eV) and Cr(VI) (580.2, 589.6 eV), confirming the photocatalytic reduction of Cr(VI) to Cr(III). The above results suggest that the TCPP is securely loaded on the UiO-66-NH_2 MOF, however, the lower PL intensity of 15-UNT signifies its improved charge transfer efficiency, making it more effective for Cr(VI) reduction. From the TRPL studies, the calculated carrier lifetimes (1.44 ns for UiO-66-NH_2 and 3.98 ns for 15-UNT) further confirm that TCPP is responsible for its longer-lived charge separation, which further reduces the recombination process and enhances photocatalytic activity. This study serves as a reference for modifying MOF photocatalysts through ligand engineering and offers new insights into the synergistic effects of adsorption and photosensitization in photocatalysis.

PDINH (3,4,9,10-perylenetetracarboxylic diimide) is a stable organic semiconductor with a suitable band gap and high electron mobility that facilitates long-range electron delocalization through strong π–π stacking. However, its photocatalytic efficiency is limited by insufficient light absorption, fast recombination, and low conductivity. To overcome these limitations, Zheng's group[105] developed a novel PDINH/NH_2-UiO-66 (PNU) Z-scheme heterojunction using a ball milling method and found that PNU-1 composite demonstrated superior Cr(VI) photoreduction efficiency than the pristine materials. Morphological studies confirmed that ball milling resulted in granular PDINH densely coating the octahedral NU-66 surface that suggests better interfacial contact, which helps in enhancing charge transfer between the two components. Thermogravimetric analysis further indicated that PNU exhibited greater thermal stability than UNH after loading PDINH, with a weight loss of 48% at 500 °C compared to 43% for NU-66, and it maintains its structural stability even after light irradiation. The red shift in the UV-vis absorption edge to 700 nm highlighted the composite's improved light absorption. Photocatalytic studies showed that PNU-1 achieved 97% Cr(VI) reduction within 60 minutes, with a rate constant of 0.063 min^{-1}. However, in the absence of the –NH_2 group, the rate dropped significantly to 0.0029 min^{-1}, confirming its crucial role in the photoreduction process. Beyond its exceptional photocatalytic performance, PNU-1 maintained high activity even after five cyclic runs, demonstrating excellent stability and reusability. This study offers valuable insights into designing highly efficient Z-scheme heterostructures between MOFs and organic semiconductors like PDINH for environmental remediation.

In addition to heavy metal reduction, UiO-66-NH_2-based photocatalysts are also highly efficient in the degradation of organic contaminants like dyes and antibiotics. The following sections explore these applications, contrasting the degradation mechanisms and the effect of different composite structures.

5.4. Dye degradation

Industrial processes like plastic production, textiles, cosmetics, and dyeing release wastewater containing harmful dyes such as Methyl Red, Methylene Blue, Rhodamine Blue, *etc.* These toxic dyes pose significant risks to human health and ecosystems if discharged untreated.[106] But treatment of these dyes with traditional methods often produces excess waste products. Hence, photocatalysis is considered to be a prominent approach for the efficient degradation of these toxic pollutants while reducing waste generation. After light irradiation, electron–hole pairs got separated and they participate in redox reactions with H_2O and dissolved oxygen (O_2). Firstly, the holes in VB react with H_2O to generate hydroxyl radicals ($^{\bullet}OH$), which are highly reactive and play a major role in the degradation process (eqn (13)).

$$h^+ + H_2O \rightarrow {}^{\bullet}OH + H^+ \quad (13)$$

Secondly, as shown in eqn (14)–(17), the photoexcited e^- s in CB reduce O_2 in order to form other reactive oxygen species (ROS) like superoxide radical ($^{\bullet}O_2$) and H_2O_2.

$$e^- + O_2 \rightarrow O_2^{\bullet -} \quad (14)$$

$$O_2^{\bullet -} + H^+ \rightarrow HO_2^{\bullet} \quad (15)$$

$$HO_2^{\bullet} + H^+ \rightarrow H_2O_2 \quad (16)$$

$$H_2O_2 \rightarrow 2{}^{\bullet}OH \quad (17)$$

Finally, these reactive species react with dye molecules to form degraded products (eqn (18)).

$$\text{Dye} + {}^{\bullet}OH \rightarrow CO_2 + H_2O + \text{other byproducts} \quad (18)$$

Research highlights Zr-based UiO-66-NH_2 MOFs as highly stable and versatile photocatalysts, making them effective for purifying contaminated water. Following this, UiO-66-NH_2 was synthesized by Qi Chen and team *via* a solvothermal method and characterized comprehensively to evaluate its potential for selective cationic dye adsorption from wastewater.[107] The material exhibited a BET surface area of 616.55 $m^2\ g^{-1}$ and a notable external surface area of 304.28 $m^2\ g^{-1}$, contributing to its high adsorption efficiency. The zeta potential of UiO-66-NH_2 was more negative (–4.91 mV) in comparison to UiO-66 (−3.65 mV) due to the protonation of –NH_2 groups, enhancing electrostatic interactions with cationic dyes such as methylene blue. Adsorption kinetics revealed that the uptake followed a pseudo-second-order model, suggesting chemisorption to be the rate-determining step. The maximum adsorption capacity for MB was 96.45 mg g^{-1} for UiO-66-NH_2, significantly higher than for anionic dyes like methyl orange (28.97 mg g^{-1}). The material demonstrated excellent stability and reusability while maintaining its adsorption efficiency over six cycles. This work provides a sustainable and reusable adsorbent for dye wastewater treatment, with a well-characterized mechanism involving surface electrostatic interactions and enhanced charge selectivity. To further enhance its activity, MOF-based composite Ag/UiO-66-NH_2 was synthesized by the impregnation of $AgNO_3$ on UNH, followed by reduction using $NaBH_4$, and then used for dye photodegradation by L. L. Zhang and his co-workers.[108] TEM images confirm the presence of spherical Ag NPs (<10 nm) uniformly distributed and tightly anchored within UiO-66-NH_2 host nanoparticles that prevent aggregation and enable uniform exposure of active sites. Fig. 11b explains as compared to UiO-66-NH_2, Ag/UiO-66-NH_2 composites show improved RhB photodegradation, which is primarily explained by two factors. Firstly, solid-state PL spectra (Fig. 11a) support the idea that the visible-light absorption of Ag/UiO-66-NH_2-*X* samples was dramatically boosted with an increase in $AgNO_3$ loading, as it helps to separate photogenerated electrons and holes effectively because of the LSPR effect of Ag NPs. Secondly, the inherent light absorption capability of UiO-66-NH_2 in the UV-vis region enables the generation of charge carriers. However, when combined with the Ag NPs, it results in synergistic charge transfer and reduced recombination. After that, Ag NPs (which have a lower Fermi level) trap the photogenerated electrons quickly, and these electrons, while reacting with peroxide, generate highly reactive hydroxyl radicals (*e.g.*, HO^-, HOO^-). These radicals decompose the RhB, and this peroxide, light irradiation, and photocatalyst are all essential for effective RhB photodegradation. Similarly, as previously discussed in the Cr(VI) section, Shen *et al.* examined the photocatalytic efficiency of Pd@UiO-66(NH_2), mainly to simultaneously eliminate a range of pollutants, such as Cr(VI) reduction, MB, and MO degradation, using a single system.[49] It is observed that, after 60 minutes of visible light irradiation, the single systems show a 70% reduction of Cr(VI), with MO and MB degradation ratios at 5% and 38%, respectively. Adding organic dyes (MB or MO) significantly enhances Cr(VI) reduction, with binary systems achieving 79% and 100% reduction for Cr(VI). The presence of Cr(VI) facilitates the photocatalytic oxidation of MB and MO. The boost in the photocatalytic activity of Pd@UiO-66(NH_2) within binary systems arises from the synergistic interaction between the reduction and oxidation processes, which prevents e^-–h^+ recombination. This bifunctional photocatalyst can simultaneously oxidize dyes and reduce Cr(VI) under visible light, with the synergistic effect evidenced during these processes.

A simple water bath deposition method is used by Wang's group to construct a series of CdS/UiO-66-NH_2 heterojunctions for the photodegradation of RhB dyes.[109] Among them, 1.5-CdS/UiO-66-NH_2 achieved the highest photodegradation rate of 92.5% in 40 minutes and maintained excellent photostability even after 4 cycles. It exhibits a cubic structure with a size of 170–180 nm, and UNH retains its structural integrity and is homogeneously decorated on CdS NPs, as confirmed by SEM analysis. The photocurrent intensity for 1.5-CdS/UiO-66-NH_2 (1.3 μA cm^{-2}) was notably higher than that of CdS (0.45 μA

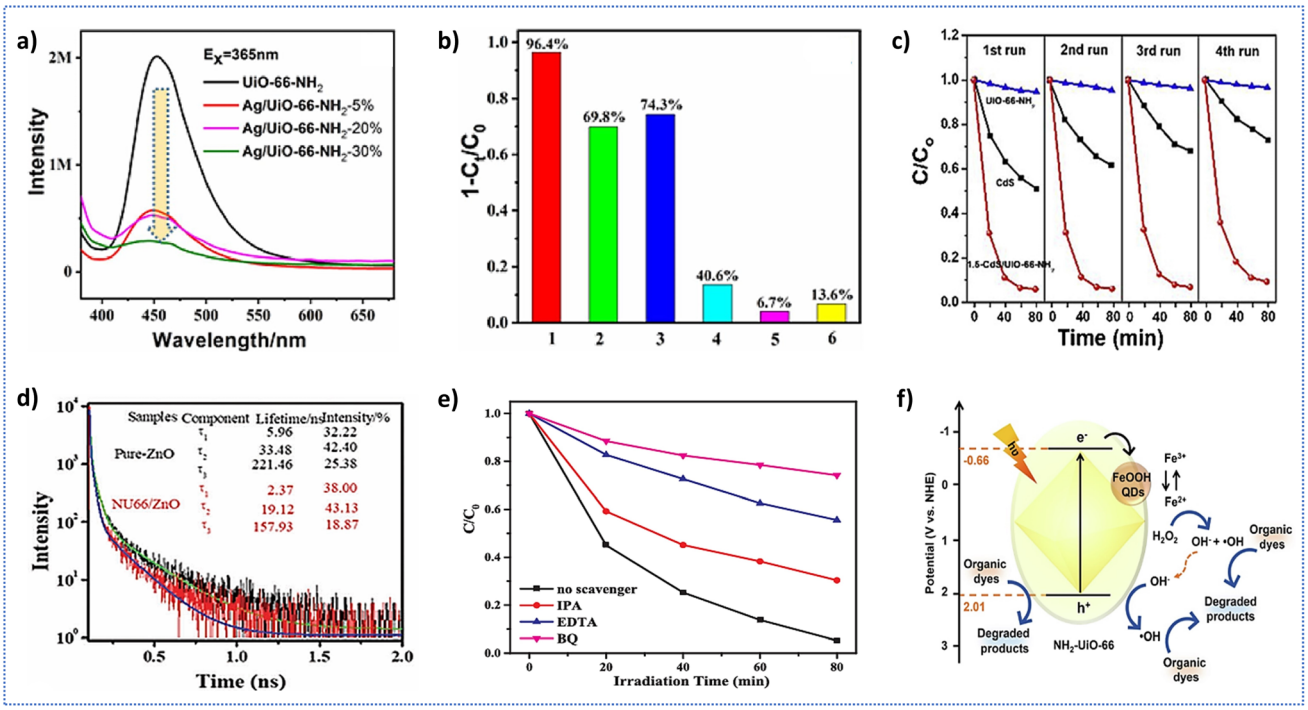

Fig. 11 (a) Solid-state PL spectra of UiO-66-NH_2 and Ag/UiO-66-NH_2-*X* (*X* = 5%, 20%, and 30%), (b) efficiency of photodegradation under various conditions ((i) Ag/UiO-66-NH_2-20%/UV-vis light/H_2O_2; (ii) Ag/UiO-66-NH_2-20%/UV-vis light; (iii) UiO-66-NH_2/UV-vis light/H_2O_2; (iv) UV-vis light/H_2O_2; (v) Ag/UiO-66-NH_2-20%/in the dark/H_2O_2; (vi) UV-vis light), reproduced with permission from Springer. Copyright © 2022.[108] (c) Recycling tests of CdS NPs, UiO-66-NH_2, and *x*-CdS/UiO-66-NH_2 for RhB degradation under visible light, reproduced with permission from Elsevier. Copyright © 2019.[109] (d) Time-resolved PL spectra of pure ZnO and 5% NU66/ZnO composite, (e) impact of scavengers on RhB degradation by BiOI@UNCN-40, reproduced with permission from Elsevier. Copyright © 2018.[110] (f) Proposed mechanism for dye degradation over NH_2-UiO-66/FeOOH (10%), reproduced with permission from Elsevier. Copyright © 2022.[111]

cm^{-2}) and UiO-66-NH_2 (0.21 μA cm^{-2}) that signifies improved photoelectronic response of the composite. This intensity is nearly 2.8 times and 6.2 times higher than CdS and UiO-66-NH_2, respectively, which reflects efficient electron–hole pair separation of the composite. In addition, its degradation rate constant was 56 times and 5 times greater than UiO-66-NH_2 and CdS nanoparticles, respectively. The enhanced photocatalytic activity and greater stability (Fig. 11c) of 1.5-CdS/UiO-66-NH_2 are attributed to its larger surface area, strong interfacial contact, the formation of an n–n type heterojunction, and improved charge separation.

Flower-like NH_2-UiO-66-ZnO nanocomposite was developed by D. Teng and colleagues and used for visible-light-driven photodegradation of MB and MG.[112] A simple hydrothermal method is used for the synthesis of the composite, and the TGA analysis confirmed the composite's thermal stability while structural studies showed uniform loading of NU66 (NH_2-UiO-66) nanoparticles onto flower-like ZnO without significant structural or chemical changes during MB degradation. The NU66/ZnO composites exhibited larger specific surface areas and micropore volumes than standalone NU66 or ZnO, and these structural changes facilitate the no. of reactive sites that enhance the light absorption capacity of the material, achieving removal efficiencies of 96.7% for MB and 98% for MG within 1 hour. Additionally, the shorter average lifetime of NU66/ZnO composite compared to ZnO (Fig. 11d) can be attributed to the efficient transfer of photoelectrons between NU66 and ZnO. The study proposed a Type II heterojunction mechanism, where photoinduced electrons and holes transfer under visible light, enhancing pollutant degradation into CO_2 and H_2O. Table 5 summarizes the photocatalytic performance of various UiO-66-NH_2-based hybrid photocatalysts for dye degradation.

Bismuth-oxohalides (BiOX) are known for their layered structure, suitable bandgap, excellent photocatalytic properties, and visible-light responsiveness. By coupling BiOCl and UNH, G. Xia and co-workers constructed a novel double Z-type heterojunction catalyst UiO-66-NH_2/BiOCl/Bi_2S_3 for the photodegradation of RhB dye.[114] The combined effect of the extensive visible light range and the Z-scheme charge transfer mechanism guarantees exceptional photocatalytic activity. ESR tests have also confirmed that h^+ and $^{\cdot}O_2^-$ are the primary active species involved in the photocatalysis. Similarly, Liang *et al.* developed a ternary BiOI@UIO-66(NH_2)@g-C_3N_4 Z-scheme heterojunction that achieved remarkable photocatalytic degradation of RhB under the exposure of visible light.[110] The integration of BiOI nanosheets with UIO-66(NH_2) and g-C_3N_4 created a sandwich-like structure and the narrow bandgap (~1.8 eV) of BiOI helps in efficient absorption of light and the 2D-semiconductor, g-C_3N_4 acts as e^- mediator for efficient charge migration to happen. The optimized BiOI@UNCN-40 composite achieved an impressive 95% RhB degradation within 80 minutes, significantly outperforming pure BiOI, UIO-

Table 5 Summary of UiO-66-NH_2-based photocatalysts for the degradation of different dyes

Sl no.	Material	Synthesis method	Band gap (E_g)	Light source	Efficiency% (dye)	Ref.
1	CdS/UiO-66-NH_2	Water bath deposition (60 °C for 30 min)	—	300 W Xe lamp with a 420 nm cutoff filter	92.5% in 40 min (RhB)	109
2	Ag/UiO@fabric	Ion exchange method	2.75 eV	150 W Xe lamp, $\lambda > 400$ nm	98% in 2 h (RhB)	113
3	Pd@UiO-66(NH_2)	Solvothermal method (180 °C for 1.5 h)	—	300 W Xe lamp with a 420 nm cutoff filter	80% in 1 h (MB) 50% in 1 h (MO)	49
4	UiO-66-NH_2/BiOCl/Bi_2S_3	Solvothermal method (180 °C for 24 h)	2.45 eV	300 W Xe lamp, $\lambda > 400$ nm	98% in 60 min (RhB)	114
5	NH_2-UiO-66/FeOOH	Room temp stirring	2.53 eV	White LED light (60 W)	82.2% in 180 min (MV)	111
6	BiOI@UiO-66(NH_2)@g-C_3N_4	*In situ* solvothermal-hydrothermal approach (120 °C for 12 h)	1.89 eV	300 W Xe lamp, $\lambda > 420$ nm	95% in 80 min (RhB)	110
7	Ag/UiO-66-NH_2	Wet impregnation	2.07 eV	300 W Xe lamp, $\lambda < 400$ nm	96% in 40 min (RhB)	108
8	NH_2-UiO-66/ZnO	Hydrothermal (120 °C for 3 h)	2.86 eV	300 W Xe lamp, $\lambda > 420$ nm	96.7% in 1 h (MB) 98% in 1 h (MG)	112

66(NH_2), and their binary counterparts. This superior activity was ascribed to the Z-scheme charge transfer mechanism, which effectively suppressed recombination and promoted the generation of reactive species, primarily superoxide radicals ($^{\bullet}O_2^-$). The scavengers test in Fig. 11e also supports the mechanism, showing that BQ significantly reduces photocatalytic performance, confirming $^{\bullet}O_2^-$ as the primary active species, whereas the partial inhibition by EDTA and IPA indicates that h^+ and $^{\bullet}OH$ play secondary roles in the photocatalytic system. Additionally, the composite demonstrated excellent stability and reusability after multiple cycles with no significant loss in its activity.

In a recent study, Hosseini *et al.* synthesized NH_2-UiO-66 decorated with FeOOH quantum dots to improve the photocatalytic degradation of organic dyes under exposure to visible light.[111] The FeOOH quantum dots (2–5 nm) were uniformly anchored onto the surface of NH_2-UiO-66 *via* a post-synthetic method. The structural integrity of NH_2-UiO-66 was maintained after functionalization, and the addition of FeOOH quantum dots resulted in a red shift in the UV-absorption spectrum, enhancing visible light harvesting. The optimized composite with 10 wt% FeOOH demonstrated superior photo-Fenton activity, achieving 82.2% methyl violet degradation in H_2O_2. The mechanism of this reaction (Fig. 11f) suggests that this improvement was ascribed to effective charge separation and transfer from the excited NH_2-UiO-66 to FeOOH, which reduced electron–hole recombination. As the mechanism suggests, upon light absorption, the UiO-66-NH_2 generates electron–hole pairs where the FeOOH quantum dots act as electron acceptors from the CB of UNH, which prevents the e^-/h^+ recombination process. These e^-s promotes the reduction process of Fe^{3+} to Fe^{2+} (eqn (20)) and these Fe^{2+} then reacts with H_2O_2, producing hydroxyl radicals ($^{\bullet}OH$) and OH^- *via* a photo-Fenton reaction (eqn (21)). Scavengers trapping experiments also confirms $^{\bullet}OH$ as the reactive species and as eqn (22) indicates the OH^- can be oxidized to form more $^{\bullet}OH$ radicals since the VB of NH_2-UiO-66 (+2.01 V *vs.* NHE) is sufficiently positive to drive this OH^- oxidation process. Interestingly, water cannot form $^{\bullet}OH$ directly due to its higher oxidation potential (2.27 V *vs.* NHE) than UNH. Finally, the highly reactive $^{\bullet}OH$ radicals effectively degrade organic dye molecules (eqn (23)), and simultaneously, the photoinduced holes can also directly oxidize dye molecules (eqn (24)). These synergistic pathways enhance photocatalytic efficiency for organic pollutant degradation. The above-discussed eqn are given below:

$$\text{NH}_2\text{-UiO-66/FeOOH(10\%)} + h\nu \rightarrow \text{electron} + \text{hole} \quad (19)$$

$$\text{Fe}^{3+} + \text{e}^- \rightarrow \text{Fe}^{2+} \quad (20)$$

$$\text{H}_2\text{O}_2 + \text{Fe}^{2+} \rightarrow \text{Fe}^{3+} + \text{OH}^- + {}^{\bullet}\text{OH} \quad (21)$$

$$\text{OH}^- + \text{hole} \rightarrow {}^{\bullet}\text{OH} \quad (22)$$

$$\text{Organic dyes} + {}^{\bullet}\text{OH} \rightarrow \text{degraded products} \quad (23)$$

$$\text{Organic dyes} + \text{hole} \rightarrow \text{degraded products} \quad (24)$$

The composite exhibited excellent stability and reusability, retaining its photocatalytic efficiency over four consecutive cycles with minimal Fe leaching. The synergy between the MOF and FeOOH quantum dots provided more active sites, enhanced electron dynamics, and improved reactive oxygen species generation. This work highlights the potential of integrating MOFs with semiconductor quantum dots to develop robust and efficient photocatalysts for wastewater treatment.

Co–Fe LDH and UiO-66-NH_2 are used to form a hybrid composite, Co–Fe-LDH@UiO-66-NH_2, by Khajeh *et al.* for efficient adsorption of some organic dyes like MB and MR.[115] FT-IR identified the functional groups of both UiO-66-NH_2 (NH_2 stretching at 3417 cm^{-1} and carboxylate coordination at 1571 cm^{-1}) and Co–Fe LDH (OH stretching and nitrate vibrations). This combination improved dye adsorption by leveraging the 2D layered structure of LDH, which facilitated greater accessibility to active sites and minimized UiO-66-NH_2 particle aggregation. Adsorption studies showed high capacities of 555.62 mg g^{-1} for MB and 588.2 mg g^{-1} for MR, with the process fitting the Langmuir model, which indicates monolayer adsorption. Optimal conditions (pH 8.0, 10 minutes extraction time) were determined, showcasing the composite's rapid adsorption kinetics. The synergistic integration of Co–Fe LDH and UiO-66-NH_2 combined the magnetic properties and 2D accessibility of LDH with the high surface area and functional versatility of UiO-66-NH_2, hence it provides a robust and efficient adsorbent for organic dye removal, particularly relevant for wastewater treatment applications.

5.5. Antibiotic degradation

Antibiotics are emerging as a new class of pollutants because they are necessary for everything from plant communities to animals, and they pose a serious threat to both terrestrial and aquatic ecosystems. With a broad visible-light responsive capacity and a low bandgap of around 2.7 eV, UiO-66-NH_2 is a suitable MOF that offers excellent efficiency for the oxidation of various contaminants. Similar to the dye degradation mechanism, upon light exposure on UNH material, the photogenerated electron–hole pairs interact with adsorbed O_2 and H_2O to produce reactive species like hydroxyl ($^{\bullet}OH$) and superoxide ($O_2^{\bullet-}$) radicals. These radicals break down organic pollutants (eqn (25)) into harmless byproducts (CO_2 and H_2O). The process occurs on the catalyst surface, where these antibiotics adsorb, degrade, and desorb, allowing a continuous photodegradation process to occur.

$$\text{Drugs} + {}^{\bullet}OH \text{ or } O_2^{\bullet} \rightarrow CO_2 + H_2O + \text{degradation product} \quad (25)$$

Various types of UNH-based composites have been developed, and among these, Y. Pan *et al.* developed an AgI/UiO-66NH_2 composite using a simple ion-exchange precipitation method for efficient tetracycline photodegradation, achieving an 80.7% photocatalytic efficiency, *i.e.*, over 3.8 times higher than UiO-66(NH_2).[116] The composite exhibited enhanced activity due to its efficient e^-–h^+ separation that can be explained by two charge transfer pathways: a type II heterojunction and a Z-scheme heterojunction. In internal charge transfer, electrons transfer from the CB of UiO-66-NH_2 to AgI's CB, while the holes migrate from AgI's VB to UiO-66-NH_2's VB. Ag^+ ions are reduced to Ag during photocatalysis, forming a bridge that facilitates Z-scheme charge transfer. In this system, photogenerated electrons from plasmonic Ag migrate through AgI and the Ag bridge to UiO-66-NH_2, reducing electron–hole recombination. In external charge transfer, electrons from UiO-66(NH_2) and holes from AgI reach the catalyst's surface, driving redox reactions. Electrons are being used to reduce oxygen to reactive oxygen species ($^{\bullet}O_2^-$, H_2O_2, and $^{\bullet}OH$), and h^+ are used to degrade tetracycline into intermediates, CO_2, and H_2O. These processes enhance light absorption *via* SPR, reduce photo corrosion of AgI, promote efficient charge separation, and boost oxidation–reduction reactions. Table 6 presents the summarization of photocatalytic antibiotic degradation by various UiO-66-NH_2-based photocatalysts.

Compared to other noble metals like Ag and Au with the SPR effect, metallic bismuth (Bi) is a cost-effective alternative for photocatalysis, leveraging its surface plasmon resonance (SPR) effect for enhanced catalytic performance. Therefore, S. Jing and coworkers fabricated a novel photocatalyst, Bi/NH2-UiO-66, using one-step solvothermal synthesis for the degradation of tetracycline.[117] With a degradation efficiency of 95.8% in 2 hours, this composite surpasses pure NH_2-UiO-66 by 2.7 times (Fig. 12a). A tight contact surface is formed between metal Bi and NU in the BNU composite that facilitates the charge carrier transfer. The UV-vis absorption band edge of BNU displayed a red shift compared to pure NU. ESR studies reveal under light conditions, TEMPO-h^+ signals decrease, confirming the presence of h^+ and DMPO-$^{\bullet}O_2^-$ signals of BNU-4 (Fig. 12b) exhibited stronger superoxide radical intensity than NU, highlighting $^{\bullet}O_2^-$ as a key reaction contributor. The high photocatalytic performance of Bi/NH_2-UiO-66 is due to the metal Bi's SPR effect, which further enhances visible light absorption, accelerates carrier transfer, and prevents the electron–hole recombination process. The recycling tests revealed a slight decrease in Bi levels from 49.32% to 46.23% after repeated cycles, indicating that the photocatalyst is stable and active even after continuous use. With another type of Bi-based materials, Xia *et al.* designed a UiO-66-NH_2/BiOCl/Bi_2S_3 double Z-scheme heterojunction photocatalyst that exhibited remarkable efficiency for TC degradation under visible-light irradiation.[114] The combination of UiO-66-NH_2, BiOCl, and Bi_2S_3 created a synergistic system where each component played a critical role: UiO-66-NH_2 offered a high surface area and visible-light activity due to its amino groups, BiOCl provided a layered structure for effective charge separation, and Bi_2S_3 extended the visible-light absorption range due to its narrow bandgap. The optimized composite achieved 93% TC degradation within 120 minutes, significantly outperforming individual and binary counterparts. This superior performance was linked to the double Z-scheme charge transfer mechanism, which promoted efficient e^-–h^+ separation while retaining strong oxidation and reduction potentials for generating active species like h^+ and $^{\bullet}O_2^-$. Characterization studies confirmed the intimate contact between the three materials, facilitating rapid charge transport and

Table 6 Summary of UiO-66-NH_2-based photocatalysts for degradation of antibiotics

Sl no.	Material	Synthesis method	S_{BET} ($m^2\ g^{-1}$)	Band gap	Light source	Photocatalytic activity	Ref.
1	Bi/UiO-66-NH_2	Solvothermal (160 °C for 15 h)	134.10	2.56 eV	Visible light	95.8% in 120 min (TC)	117
2	Ti-doped Zr-UiO-66-NH_2	Solvothermal (120 °C for 48 h)	—	2.70 eV	300 W Xe lamp with $\lambda \leq 400$ nm	99.8% (TC-HCL)	102
3	$MgFe_2O_4$@UiO-66(Zr)–NH_2	Microwave-assisted solvothermal (120 °C for 12 h)	426	2.60 eV	500 W Xe lamp with an optical filter ($\lambda > 420$ nm)	55% in 160 min	118
4	ZnO@BiOBr/UiO-66-NH_2	Hydrothermal	100.8	2.38 eV	LED lamp	93.7% in 30 min (TC)	119
5	$CoTiO_3$/UiO-66-NH_2	Hydrothermal (120 °C for 24 h)	413.027	2.49 eV	250 W lamp with $\lambda > 400$ nm filter	90.13% in 1 h (NFX)	74
6	Bi_2MoO_6	Solvothermal (180 °C for 16 h)	24.26	—	250 W Xe lamp, $\lambda > 400$ nm	72% in 4 h (TC)	120
7	UiO-66-NH_2/BiOCl/Bi_2S_3	Solvothermal method (180 °C for 24 h)	53.8	2.45 eV	300 W Xe lamp, $\lambda > 400$ nm	93% in 120 min (TC)	114
8	BiOI@UIO-66(NH_2)@g-C_3N_4	*In situ* solvothermal-hydrothermal approach (120 °C for 12 h)	123	1.89 eV	300 W Xe lamp, $\lambda > 420$ nm	80% in 180 min (TC)	110
9	AgI/UiO-66(NH_2)	*In situ* ion exchange precipitation	425.88	2.66 eV	300 W Xenon lamp with a cutoff filter of 420 nm	65.6% after 40 min (TC)	116
10	α-MnO_2@UiO-66-NH_2	Solvothermal treatment (12 h at 140 °C)	709.34	—	300 W Xe lamp with $\lambda \geq 420$ nm filter	93.23% in 1 h (O-TCH)	9
11	UiO-66-NH_2@ZIF-67	Sonochemical method	950	—	500 W Hg lamp, $\lambda > 400$ nm	97% in just 60 min (RhB)	121

minimizing recombination. Additionally, the composite displayed excellent photocurrent response and lower resistance for charge transfer, indicating efficient electron transport and reduced recombination rates.

Transition metal-based oxides are often used in photocatalysis and other fields due to their semiconductor-like properties, suitable bandgap, and capacity to absorb visible light effectively. Taking its advantages into consideration, S. Subudhi *et al.* synthesized the CTO-modified UiO-66-NH_2 (UNH) p–n heterojunctions for the degradation of Norfloxacin (NFX) under the exposure of visible light.[74] The smaller arc radius of the composite, as shown in Fig. 12c, indicates its enhanced interfacial charge transfer ability. Data from the transient photocurrent study shows that the heterojunction's charge carriers have a longer lifetime than UNH's, which is explained by effective charge separation and reduced recombination. The foregoing results are also supported by the decrease in PL intensity. When compared to pure MOF, the composite exhibits superior visible light responsiveness from solar light irradiation and outstanding photocatalytic activity because of its active reaction sites, which can be explained by the presence of heteroatoms, which increase the hydrophilicity and give an appropriate contact site between NFX and CTO/UNH. Additionally, the composites maintained stability over four reaction cycles (Fig. 12d), which confirms their suitability for large-scale applications. Due to $MgFe_2O_4$'s magnetic properties and high stability, tetracycline antibiotics in wastewater may be treated with the $MgFe_2O_4$@UiO-66(Zr)–NH_2 catalyst, according to T. K. Vo *et al.*, produced by a microwave-assisted hydrothermal method.[118] FT-IR peaks at 640 cm^{-1} confirm the formation of Zr–O bonds between Zr^{4+} and the carboxylate linker in UiO-66-NH_2, while peaks at 568 cm^{-1} and 440 cm^{-1} correspond to $M_{tetra\text{-}O}$ and $M_{octa\text{-}O}$ bridges, respectively (Fig. 12e), retaining the structures of the pristine materials. With a high TC removal effectiveness of around 92%, the composite MFO@UN outperformed $MgFe_2O_4$ (about 48%) and UiO-66(Zr)–NH_2 (nearly 57%). TGA measurements indicate that the composite has superior thermal stability than the original UiO-66(Zr)–NH_2 since $MgFe_2O_4$ is incorporated. Adding $MgFe_2O_4$ led to a notable decrease in the photoluminescence intensities, suggesting a positive charge transfer in the composite. More TC gets collected on the catalyst's surface due to the combination of UiO-66(Zr)–NH_2 and ferrite, which increased the interfacial charge transfer efficiency and catalyzed the photocatalytic degradation of TC. A ternary ZnO-nanorods/BiOBr/UiO-66-NH_2 heterojunction was constructed by Ghorbani *et al.* by a simple hydrothermal method, and the enhanced efficiency of TC photodegradation was found to be about 98.2%.[119] TEM images in Fig. 12f clearly indicate the formation of the ZnO nanorod and the ternary nanocomposite. The composite's UV-vis DRS has a broad absorption spectrum in the visible light domain. The novel heterojunction exhibits higher photocatalytic activity than pure photocatalysts because of its homogeneous size distribution, large light absorption spectrum, and high surface area. Two possible charge transfer pathways were proposed for the ZBU ternary photocatalyst system under light irradiation (Fig. 12g). In the first scenario, electrons were assumed to

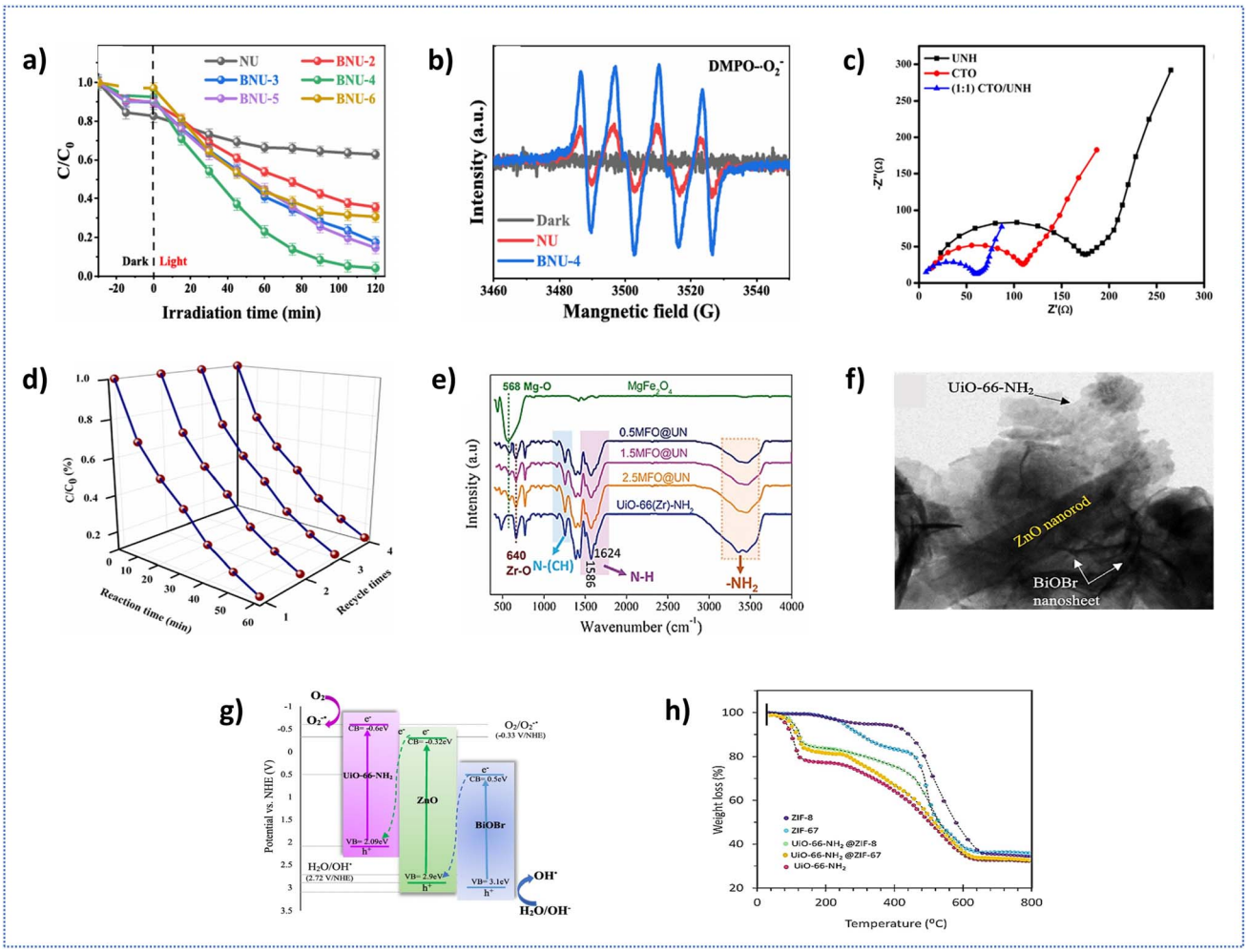

Fig. 12 (a) Photocatalytic degradation of TC by NU and BNU composites under vis-light irradiation, (b) ESR spectra of DMPO-$^{\cdot}O_2^-$ for NU and BNU-4, reproduced with permission from Elsevier. Copyright © 2024.[117] (c) EIS analysis of UNH, CTO, and CTO@UNH (1 : 1), (d) reusability test results of CTO@UNH (1 : 1) composite, reproduced with permission from Elsevier. Copyright © 2020.[74] (e) FTIR spectra of the samples, reproduced with permission from The Korean Institute of Chemical Engineers. Copyright © 2022.[118] (f) TEM images of the ZBU heterojunction, (g) Z-scheme mechanism of ZnO/BiOBr/UiO-66-NH_2 charge transfer on TC degradation, reproduced with permission from Elsevier. Copyright © 2023.[119] (h) TGA curves of pristine UiO-66-NH_2, ZIF-67, ZIF-8, and their composites, reproduced with permission from Wiley. Copyright © 2024.[121]

transfer from the CB of BiOBr to the VB of ZnO and UiO-66-NH_2. However, this contradicts XPS findings, which reveal that ZnO and BiOBr act as electron donors, while UiO-66-NH_2 functions as an electron acceptor. A more consistent mechanism involves a double Z-scheme pathway, wherein electrons from BiOBr's CB recombine with holes in ZnO's VB, and electrons from ZnO's CB recombine with holes in UiO-66-NH_2's VB. This configuration suppresses charge recombination, extends carrier lifetimes, and promotes directional charge separation. The band edge positions support this: UiO-66-NH_2's CB (−0.6 V *vs.* NHE) is negative enough to reduce O_2 to $^{\cdot}O_2^-$ (−0.33 V), while BiOBr's VB (3.1 V) is more +ve than the $^{\cdot}OH$ formation potential (2.72 V). These energetics enable efficient ROS generation, corroborated by scavenger studies where inhibition of h^+, $^{\cdot}OH$, and $^{\cdot}O_2^-$ suppressed TC degradation. Thus, the proposed double Z-scheme aligns with both experimental data and band alignment, explaining the enhanced photocatalytic performance *via* improved charge transfer and ROS-driven degradation. Another metal oxide-based photocatalyst, α-MnO_2@UiO-66-NH_2 (MnU), was synthesized by Dash *et al.*[9] using a solvothermal method, whose morphological analysis shows that the MOF remains intact, and the close contact between α-MnO_2 and the MOF in the composite, *i.e.*, rod-shaped α-MnO_2 embedded within UNH octahedrons. The +ve slope in the Mott–Schottky plot confirms the n-type semiconductor nature of both α-MnO_2 and UNH. EIS with a smaller arc radius reveals reduced charge-transfer resistance and enhanced conductivity. With a 93.23% O-TCH degradation performance, the composite performs nearly 4 times better than the parent UNH MOF due to the improved interfacial contact and efficient charge separation, verified by transient photocurrent and PL intensity reduction.

Jeyhoon *et al.* synthesized a UiO-66-NH_2@ZIF-67 core–shell composite by coating UiO-66-NH_2 with ZIF-67.[121] Morphological study confirms that ZIF-67 forms a uniform shell around the

UiO-66-NH_2 core, enhancing the contact interface for efficient charge transfer. The composite showed a notable boost in visible-light absorption due to the synergy between UiO-66-NH_2 and ZIF-67. This improved light absorption and efficient charge separation from the core–shell structure resulted in a five-fold increase in TC degradation efficiency compared to pure UiO-66-NH_2. Specifically, the composite achieved 97% degradation of TC within 60 minutes, attributed to the generation of ROS such as $^{\bullet}OH$ and $^{\bullet}O_2^-$. The TGA curves in Fig. 12h demonstrate the thermal stability of the pristine MOFs, further indicating that the resulting composite remains stable up to 300 °C. Additionally, the composite displayed remarkable stability and reusability while retaining its photocatalytic efficiency over 5 successive cycles without any significant loss in its activity. This study highlights the potential of MOF-on-MOF composites in addressing antibiotic contamination in wastewater by improving photocatalytic efficiency and long-term durability.

Conductive organic polymers like polypyrrole (PPy) and polyaniline have been widely utilized to enhance photocatalyst performance due to their π-conjugated systems, excellent optical properties, and efficient electron transport. Among them, PPy, a p-type semiconductor with strong visible light absorption, has demonstrated effectiveness in improving semiconductor photocatalytic efficiency. To overcome the limitations of conventional solvothermal synthesis such as long reaction times, toxic solvents, and high energy consumption, Qi Wang's group pioneered a green synthesis approach using ball milling. In this method, a Z-scheme PPy/UiO-66-NH_2 photocatalyst was synthesized by integrating p-type PPy with n-type NH_2-UiO-66 (NU-66).[122] During synthesis, PPy was uniformly dispersed on the surface of the metal–organic framework (MOF). Specifically, PPy and NU-66 were loaded with three large and four small balls in a ball milling tank operating at 30 Hz for 20 minutes, ensuring effective dispersion and interaction. The structural characterization confirmed the uniform distribution of PPy on the MOF surface, which plays a crucial role in modifying its electronic properties. The enhanced photocurrent response of NU-66 upon PPy modification indicates improved carrier separation efficiency. EIS and PL analyses further revealed that PPy incorporation suppresses charge recombination and enhances conductivity, thereby boosting the photocatalytic performance of the composite. Electronic structure analysis *via* the Mott–Schottky curve confirmed that NU-66 exhibits a positive slope, characteristic of n-type semiconductors, while PPy shows a negative slope, confirming its p-type nature. The interaction between these two materials establishes a built-in electric field, facilitating efficient charge separation and transfer. Density functional theory (DFT) calculations further verified significant charge transfer at the PPy/NU-66 interface, leading to a narrowed band gap and enhanced redox capabilities within the Z-scheme heterojunction. These structural and electronic modifications translate into superior photocatalytic activity, and the PPy/UiO-66-NH_2 composite achieved 90% degradation of tetracycline (TC) in 180 minutes. Additionally, quantitative structure–activity relationship (QSAR) analysis using TEST 4.2.1 software confirmed that this photocatalytic system not only degrades TC effectively but also weakens its toxicity. This research paves the way for the development of efficient and stable photocatalytic materials based on NH_2-UiO-66, offering a sustainable approach to environmental remediation.

5.6. N_2 fixation

Ammonia (NH_3) is vital for fertilizers, traditionally produced by N_2 fixation *via* the energy-intensive Haber–Bosch process however because of stronger triple bond it has high dissociation enthalpy (941 kJ mol^{-1}) that requires high temperature and pressure. To avoid this, photocatalysis is an effective strategy, and this photocatalytic nitrogen fixation involves two key pathways: nitrogen reduction (NRR) and nitrogen oxidation (NOR). In case of NRR, the dissociative pathway follows the breakdown of N≡N bond first, associative pathway is preferred where under the sunlight, photogenerated holes oxidize H_2O to O_2 and H^+, while excited electrons and these protons reduce N_2 to NH_3 as shown in below eqn (26)–(28), enabling solar-driven NH_3 production from water and nitrogen.

$$2H_2O + 4h^+ \rightarrow O_2 + 4H^+ \quad (26)$$

$$N_2 + 6H^+ + 6e^- \rightarrow 2NH_3 \quad (27)$$

$$2N_2 + 6H_2O \rightarrow 4NH_3 + 3O_2 \quad (28)$$

Similarly, eqn (29)–(32) explain that during photocatalytic N_2 oxidation, holes oxidize N_2 and H_2O to NO, while electrons reduce O_2 to H_2O. The NO is further oxidized to nitrates, leading to nitric acid formation under sunlight and ambient conditions using N_2, O_2, and H_2O as reactants.

$$N_2 + 2H_2O + 4h^+ \rightarrow 2NO + 4H^+ \quad (29)$$

$$O_2 + 4H^+ + 4e^- \rightarrow 2H_2O \quad (30)$$

$$4NO + 3O_2 + 2H_2O \rightarrow 4HNO_3 \quad (31)$$

$$\text{Overall reaction: } 2N_2 + 5O_2 + 2H_2O \rightarrow 4HNO_3 \quad (32)$$

However, because of their higher surface area, porosity, and tunable structure, MOFs can easily capture the N_2 molecules and start the activation process under light irradiation. Previously a no. of researches have been done on nitrogen reduction process considering MOF as photocatalyst, however UNH MOF is yet to be explored more in this direction. The study by Bariki *et al.* explores the UiO-66-NH_2/$CuInS_2$ (UNH/CIS) heterostructure as a promising photocatalyst for visible-light-driven N_2 fixation, leveraging a synergistic approach to enhance charge separation and catalytic efficiency.[123] The pristine UiO-66-NH_2 MOF, despite its high surface area and amine-functionalized sites facilitating N_2 adsorption, suffers from poor charge mobility and rapid recombination of photogenerated carriers, limiting its efficiency in nitrogen reduction. To address this, the integration of $CuInS_2$ (CIS), a ternary chalcogenide semiconductor, extends light absorption into the visible range and establishes a heterojunction interface that facilitates directional charge migration, crucial for efficient

photocatalysis. The NH_3 production rate for UNH/CIS reaches a remarkable value, significantly outperforming pristine UiO-66-NH_2 and other conventional MOF-based catalysts, highlighting the effectiveness of heterojunction engineering in optimizing nitrogen fixation. This enhancement is primarily driven by the type-II band alignment, where photogenerated e^-s gradually build-up on the CB of CIS while holes remain in UiO-66-NH_2, ensuring a spatial charge separation that minimizes recombination losses. However, while this mechanism is well-supported through spectroscopic and electrochemical analyses, the study lacks a deeper exploration into the exact N_2 activation pathway, leaving ambiguity in whether the reduction follows a direct e^-/h^+ transfer mechanism or involves intermediate species such as N_2H or NH_2. Additionally, although promising, the stability and recyclability tests are conducted over a limited number of cycles, raising concerns about long-term durability and potential structural degradation under continuous irradiation. Another critical aspect overlooked in the study is the role of defect engineering—the presence of oxygen vacancies or coordinatively unsaturated Zr sites in UiO-66-NH_2 could further modulate the electronic structure, potentially enhancing N_2 activation. Similarly, the impact of proton-assisted mechanisms and the presence of residual surface species on catalytic selectivity remains unexplored. Although this work offers insightful information, it also points to the lack of research on UiO-66-NH_2-based photocatalytic N_2 fixation, indicating an underdeveloped but promising area in MOF-based catalysis. With the daunting task of cleaving the N≡N bond (941 kJ mol^{-1}) under mild conditions, additional progress in defect engineering, co-catalyst loading, and mechanistic insight is essential for maximizing efficiency and selectivity. The area continues to be plagued by low quantum efficiency, stability issues, and the interplay between hydrogen evolution and nitrogen reduction, which all require an improved strategy in catalyst design, charge modulation measures, and mechanistic investigations to span the gap between experimental advancements and practical application to sustainable ammonia production.

Although the remarkable progress in UiO-66-NH_2-based photocatalysis has been achieved, some issues remain, mainly regarding scalability, stability, and practical application. The last section critically reviews these drawbacks and outlines future directions on how to further develop the industrial applicability of UiO-66-NH_2 photocatalysts.

6. Conclusion and future outlooks

Zr-based MOFs have gained significant attention in photocatalysis due to their potential to address environmental challenges and meet energy demands using green energy sources. UiO-66 MOFs, composed of Zr clusters and BDC linkers, stand out for their exceptional thermal and chemical stability. However, their limited light absorption (*i.e.*, $E_g = 3.8$ eV) in the visible region restricts their photocatalytic efficiency. However, the NH_2-functionalized UiO-66 variant, UiO-66-NH_2, overcomes this limitation with superior visible-light absorption ($E_g = 2.89$ eV) and enhanced photocatalytic performance. Its adaptable structure supports modifications through functional metal nodes, linker substitutions, and defect engineering, maintaining stability while improving activity. This review provides a comprehensive analysis of UiO-66-NH_2 and its composites, detailing synthesis methods, properties, and applications such as H_2 & O_2 evolution reactions, reduction of CO_2 & Cr(VI), degradation of dye & antibiotics. Functionalization strategies, including metal doping, linker modifications, defect engineering, and integration with nanomaterials, have enhanced its photocatalytic performance by reducing the band gap and improving charge carrier separation. Binary and ternary heterojunctions, along with co-catalysts, further enhance activity by minimizing charge recombination and providing greater stability and recyclability in comparison to pristine UiO-66-MOF. Despite its advantages, such as high porosity, high specific surface area, thermal stability, and abundant active sites, further research is needed to optimize UiO-66-NH_2 for sustainable photocatalysis. Its potential applications still require deeper exploration compared to conventional photocatalytic materials.

For future projects, several key points must be addressed to improve the outcomes, and specific gaps during synthesis and applications need to be resolved to enhance the quality of the work.

(I) UiO-66-NH_2 demonstrates a lower surface area compared to UiO-66, attributed to partial pore blockage by the free ligand. Both materials show a reversible reduction in crystallinity when subjected to high-pressure treatment. To address these limitations, further optimization of the synthesis process is recommended to enhance surface area and stability. Additionally, exploring different BDC – derivatives could offer opportunities to modulate photocatalytic properties. Investigating the mechanical stability and structural behaviours of these materials under various stimuli will also be crucial for broadening the potential applications of MOFs.

(II) Although UiO-66-NH_2 exhibits high stability in aqueous environments, the wide pH variations in wastewater can impact the structural integrity of UNH-based materials. Therefore, further research is essential to assess their resilience under extreme pH conditions and to develop strategies for enhancing their durability in practical wastewater treatment applications.

(III) In some cases, metal substitution in the Zr-cluster of UNH with other metals helps in enhancing the photocatalytic activity by band gap modifications and charge transfer processes. However, the position and no. of metals used in the substitution process aren't explained clearly. Therefore, other modifications like linker functionalization and photosensitization should be done to enhance the overall photocatalytic activity.

(IV) The coordinated structure of UiO-66-NH_2 enables the integration of multifunctional modules into a single framework, promoting collaborative catalysis and facilitating the development of diverse MOF-based composite photocatalysts with multiple functionalities. However, the unclear structural characteristics of many complex UiO-66-NH_2-based materials significantly impede the investigation of the structure–property–performance relationship. Therefore, it is crucial to

thoroughly examine the morphology of the various components and the interface properties between the MOF and secondary materials to enhance understanding and optimize performance.

(V) Direct solvothermal synthesis is the most widely used method for MOF production, but issues such as solvent toxicity, high costs, and energy consumption make it less efficient in some cases. Emerging solvent-free methods like microwave-assisted and mechanochemical techniques show promise for UNH synthesis, but their use in composite formation or modified UNH is still in its early stages. Further research is needed to expand their industrial applications.

(VI) Only a limited number of UNH-based materials have been designed by tailoring morphology during synthesis to create mesoporous structures, nanorods, and nanospheres, which have proven highly effective in enhancing photocatalytic activity. Additionally, thin-layer nanosheets provide a higher surface area and reduced charge migration paths. Therefore, optimizing morphology into nanostructures such as nanosheets, hollow nanospheres, and nanorods can significantly enhance porosity and surface area, leading to improved photocatalytic performance.

(VII) Most modified UNH photocatalysts are typically used in powder form, which presents challenges for large-scale applications due to issues with recovery and stability. In contrast, membrane photocatalysts offer a promising alternative, combining high efficiency with improved recyclability and structural integrity. In the future, research efforts should prioritize enhancing the efficiency of membrane-based photocatalysts, enabling their broader practical application.

(VIII) Noble metals like Pd, Pt, and Au have been widely explored as co-catalysts in photocatalytic systems due to their excellent catalytic properties. However, the high cost and toxicity of these metals pose significant challenges for their large-scale application and commercialization. Consequently, there is a growing need for alternative, metal-free materials that are both cost-effective and environmentally benign. Future research should prioritize the development of such materials to facilitate the sustainable and practical use of photocatalytic technologies.

(IX) In case of defective – UNH MOFs, other than Ti – doping discussed above, other metals like Co, Cu, Ag *etc.* or nonmetals like C, N, O *etc.* can be an effective strategy as they can generate new energy levels and enhance the separation efficiency of charge carriers.

(X) Various sacrificial electron donors are used in modified UiO-66-NH_2 photocatalysts systems. On one side, investigating their impact on photocatalysts' performance is crucial, while selecting cost-effective, abundant, and sustainable agents can enhance these systems' use and scalability.

(XI) UNH-based multifunctional photocatalysts, which facilitate both oxidation and reduction reactions simultaneously, hold significant potential for renewable energy production and environmental remediation. Numerous studies have explored applications such as simultaneous Cr(VI) photoreduction, dye degradation, H_2 generation, and CO_2 reduction within a single system. However, further development of such multifunctional photocatalysts is needed to expand their applicability across a broader range of applications.

(XII) Various sacrificial electron donors are used in modified UiO-66-NH_2 photocatalyst systems. On one side, investigating their impact on photocatalysts' performance is crucial, while selecting cost-effective, abundant, and sustainable agents can enhance these systems' use and scalability.

(XIII) Photocatalytic mechanisms, including water splitting, lack a detailed analysis of reaction pathways and charge

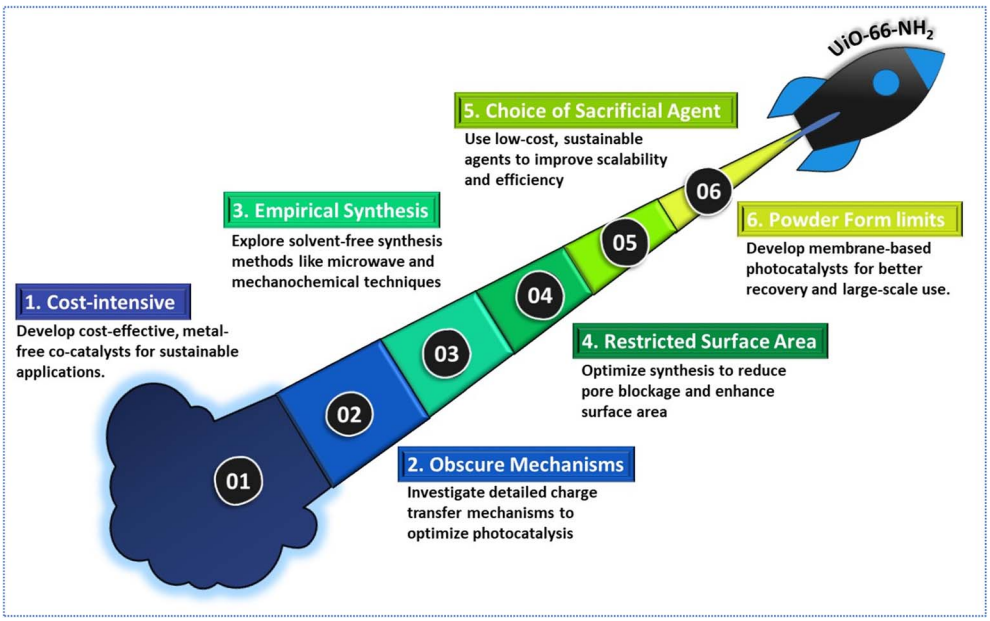

Fig. 13 Future prospects towards the advancements and enhanced photocatalytic performance of the UiO-66-NH_2-based hybrid materials.

transfer. To improve understanding, comprehensive studies are needed to provide direct evidence. Additionally, it is essential to explore the relationship between electronic structure and structural properties in UNH-based composites, optimizing performance and efficiency.

(XIV) UNH-based nanomaterials have yet to be extensively explored despite their potential to enhance our understanding of the fundamental photocatalytic mechanisms. Therefore, further research into these materials is essential to achieve optimal results in both laboratory and industrial-scale photocatalytic applications. Advanced characterization techniques, such as *in situ* analysis, electrodeless flash-photolysis, transient absorption spectroscopy, time-resolved microwave conductivity, and isotopic labelling, alongside density functional theory (DFT) calculations, should be employed to gain deeper insights into the structure–performance relationship.

(XV) In recent years, UNH-based catalysts have shown potential in constructing built-in electric fields when the charge carriers migrate towards different directions because of the incorporation of guest molecules. Moreover, the intrinsic heterogeneous charge distribution within MOF-based catalysts can induce internal electric fields. These insights pave the way for designing internal electric fields for energy storage and advancing supercapacitor technology.

(XVI) The practical application of UiO-66-NH_2-based photocatalysts is limited by challenges related to efficiency, stability, scalability, and cost. While these materials show promise due to their tunability and visible-light responsiveness, most studies have been conducted under controlled laboratory conditions, which do not reflect real-world environments such as exposure to sunlight and complex wastewater. Future research should focus on enhancing their structural stability, reusability, and performance under actual environmental conditions. Additionally, energy-intensive synthesis methods, use of solvents, and issues with crystallinity and reproducibility hinder large-scale production. Efficiency gains through microwave-assisted, mechanochemical, and spray-drying methods are still plagued by issues of crystallinity and batch-to-batch reproducibility. To advance industrial applicability, efforts must be directed toward cost-effective synthesis techniques, metal substitution strategies, and pilot-scale testing to ensure consistent performance in hydrogen production, CO_2 reduction, and environmental remediation.

Fig. 13 represents the the possible future outlooks towads the developments of UNH-based nanohybrids to enhance the photocatalytic activity. Aside from catalysis, other applications like drug delivery, molecule adsorption and separation, electrochemistry, fluorescence sensing, *etc.*, require further detailed investigations. Therefore, more innovative and smart research ideas are urgently needed to utilize UNH-MOFs across various fields.

Data availability

The submitted review article synthesizes and discusses data that have already been published and publicly available from the sources cited in the manuscript. No new data were generated during the preparation timeframe of this review.

Author contributions

Nagma Sultana: conceptualization, writing – original draft, visualization. Priyanka Priyadarshini: conceptualization, writing – original draft, review, and editing. Kulamani Parida: conceptualization, visualization, supervision.

Conflicts of interest

There are no conflicts to declare.

Acknowledgements

The authors express their profound gratitude toward Siksha 'O' Anusandhan (Deemed to be University) for giving all the necessary facilities and financial support to carry out this immense research work.

References

1 H. Liu, M. Cheng, Y. Liu, G. Zhang, L. Li, L. Du, B. Li, S. Xiao, G. Wang and X. Yang, Modified UiO-66 as Photocatalysts for Boosting the Carbon-Neutral Energy Cycle and Solving Environmental Remediation Issues, *Coord. Chem. Rev.*, 2022, **458**, 214428, DOI: 10.1016/j.ccr.2022.214428.

2 C. V. Reddy, K. R. Reddy, V. V. N. Harish, J. Shim, M. V. Shankar, N. P. Shetti and T. M. Aminabhavi, Metal-Organic Frameworks (MOFs)-Based Efficient Heterogeneous Photocatalysts: Synthesis, Properties and Its Applications in Photocatalytic Hydrogen Generation, CO2 Reduction and Photodegradation of Organic Dyes, *Int. J. Hydrogen Energy*, 2020, **45**(13), 7656–7679, DOI: 10.1016/j.ijhydene.2019.02.144.

3 X. Li and Q. L. Zhu, MOF-Based Materials for Photo- and Electrocatalytic CO2 Reduction, *J. Energy Chem.*, 2020, **2**(3), 100033, DOI: 10.1016/j.enchem.2020.100033.

4 A. Chatterjee, L. Wang and P. Van Der Voort, Metal-Organic Frameworks in Photocatalytic Z-Scheme Heterojunctions: An Emerging Technology, *Chem. Commun.*, 2023, 3627–3654, DOI: 10.1039/d2cc05819g.

5 S. Subudhi, S. P. Tripathy and K. Parida, Metal Oxide Integrated Metal Organic Frameworks (MO@MOF): Rational Design, Fabrication Strategy, Characterization and Emerging Photocatalytic Applications, *Inorg. Chem. Front.*, 2021, 1619–1636, DOI: 10.1039/d0qi01117g.

6 H. Luo, Z. Zeng, G. Zeng, C. Zhang, R. Xiao, D. Huang, C. Lai, M. Cheng, W. Wang, W. Xiong, Y. Yang, L. Qin, C. Zhou, H. Wang, Y. Zhou and S. Tian, Recent Progress on Metal-Organic Frameworks Based- and Derived-Photocatalysts for Water Splitting, *Chem. Eng. J.*, 2020, **383**, 123196, DOI: 10.1016/j.cej.2019.123196.

7 P. Behera, S. Subudhi, S. P. Tripathy and K. Parida, MOF Derived Nano-Materials: A Recent Progress in Strategic

Fabrication, Characterization and Mechanistic Insight towards Divergent Photocatalytic Applications, *Coord. Chem. Rev.*, 2022, **456**, 214392, DOI: 10.1016/j.ccr.2021.214392.

8 S. P. Tripathy, S. Subudhi, A. Ray, P. Behera, G. Swain, M. Chakraborty and K. Parida, MgIn2S4/UiO-66-NH2MOF-Based Heterostructure: Visible-Light-Responsive Z-Scheme-Mediated Synergistically Enhanced Photocatalytic Performance toward Hydrogen and Oxygen Evolution, *Langmuir*, 2023, **39**(21), 7294–7306, DOI: 10.1021/acs.langmuir.3c00151.

9 S. Dash, S. P. Tripathy, S. Subudhi, P. Behera, B. P. Mishra, J. Panda and K. Parida, A Visible Light-Driven α-MnO2/UiO-66-NH2 S-Scheme Photocatalyst toward Ameliorated Oxy-TCH Degradation and H2 Evolution, *Langmuir*, 2024, **40**(8), 4514–4530, DOI: 10.1021/acs.langmuir.3c04050.

10 D. Behera, P. Priyadarshini and K. Parida, ZIF-8 Metal–Organic Frameworks and Their Hybrid Materials: Emerging Photocatalysts for Energy and Environmental Applications, *Dalton Trans.*, 2025, **54**(7), 2681–2708, DOI: 10.1039/D4DT02662D.

11 P. Priyadarshini, A. Mishra, S. Nayak and K. Parida, NH2-MIL-125(Ti) and Its Functional Nanomaterials – a Versatile Platform in the Photocatalytic Arena, *Nanoscale*, 2025, **17**, 4906–4957, DOI: 10.1039/D4NR03774J.

12 X. W. Liu, T. J. Sun, J. L. Hu and S. D. Wang, Composites of Metal-Organic Frameworks and Carbon-Based Materials: Preparations, Functionalities and Applications, *J. Mater. Chem. A*, 2016, 3584–3616, DOI: 10.1039/c5ta09924b.

13 S. Subudhi, S. P. Tripathy and K. Parida, Highlights of the Characterization Techniques on Inorganic, Organic (COF) and Hybrid (MOF) Photocatalytic Semiconductors, *Catal. Sci. Technol.*, 2021, 392–415, DOI: 10.1039/d0cy02034f.

14 P. Priyadarshini and K. Parida, Two-Dimensional Metal-Organic Frameworks and Their Derived Materials: Properties, Synthesis and Application in Supercapacitors Field, *J. Energy Storage*, 2024, **87**, 111379, DOI: 10.1016/j.est.2024.111379.

15 A. Ray, S. Subudhi, S. P. Tripathy, L. Acharya and K. Parida, MOF Derived C/N Co-Doped ZnO Modified through Facile In Situ Coupling with NiP toward Photocatalytic H2O2 Production and H2 Evolution Reaction, *Adv. Mater. Interfaces*, 2022, **9**(34), 2201440, DOI: 10.1002/admi.202201440.

16 P. Priyadarshini, A. Mishra, A. Majhi, K. Parida and K. Parida, Engineering RGO–Driven Z-Scheme Charge Dynamics in NH2-MIL-125(Ti)/ZIF-67 for Superior Green Energy Applications, *ACS Appl. Energy Mater.*, 2025, **8**(8), 5067–5081, DOI: 10.1021/acsaem.4c03267.

17 J. H. Cavka, S. Jakobsen, U. Olsbye, N. Guillou, C. Lamberti, S. Bordiga and K. P. Lillerud, A New Zirconium Inorganic Building Brick Forming Metal Organic Frameworks with Exceptional Stability, *J. Am. Chem. Soc.*, 2008, **130**(42), 13850–13851, DOI: 10.1021/ja8057953.

18 J. Winarta, B. Shan, S. M. McIntyre, L. Ye, C. Wang, J. Liu and B. Mu, A Decade of UiO-66 Research: A Historic Review of Dynamic Structure, Synthesis Mechanisms, and Characterization Techniques of an Archetypal Metal-Organic Framework, *Cryst. Growth Des.*, 2020, **20**(2), 1347–1362, DOI: 10.1021/acs.cgd.9b00955.

19 L. Valenzano, B. Civalleri, S. Chavan, S. Bordiga, M. H. Nilsen, S. Jakobsen, K. P. Lillerud and C. Lamberti, Disclosing the Complex Structure of UiO-66 Metal Organic Framework: A Synergic Combination of Experiment and Theory, *Chem. Mater.*, 2011, **23**(7), 1700–1718, DOI: 10.1021/cm1022882.

20 C. G. Silva, I. Luz, F. X. Llabrés I Xamena, A. Corma and H. García, Water Stable Zr-Benzenedicarboxylate Metal-Organic Frameworks as Photocatalysts for Hydrogen Generation, *Chem.–Eur. J.*, 2010, **16**(36), 11133–11138, DOI: 10.1002/chem.200903526.

21 Y. Bai, Y. Dou, L. H. Xie, W. Rutledge, J. R. Li and H. C. Zhou, Zr-Based Metal-Organic Frameworks: Design, Synthesis, Structure, and Applications, *Chem. Soc. Rev.*, 2016, 2327–2367, DOI: 10.1039/c5cs00837a.

22 H. Zhang, P. Xiong, G. Li, C. Liao and G. Jiang, Applications of Multifunctional Zirconium-Based Metal-Organic Frameworks in Analytical Chemistry: Overview and Perspectives, *Trac. Trends Anal. Chem.*, 2020, **131**, 116015, DOI: 10.1016/j.trac.2020.116015.

23 H. M. Zhang, Y. L. Wang, X. F. Zhu, Z. Z. Huang, D. D. Pang, K. Wang, C. H. Wang, Z. X. Song, S. Q. Yin, L. L. Chang and J. H. Zhang, Application of UiO-66 and Its Composites for Remediation and Resource Recovery of Typical Environmental Contaminants: A Review, *Rare Met.*, 2024, 2498–2526, DOI: 10.1007/s12598-023-02591-8.

24 S. Xu, Q. Gao, C. Zhou, J. Li, L. Shen and H. Lin, Improved Thermal Stability and Heat-Aging Resistance of Silicone Rubber via Incorporation of UiO-66-NH2, *Mater. Chem. Phys.*, 2021, **274**, 125182, DOI: 10.1016/j.matchemphys.2021.125182.

25 F. Ahmadijokani, H. Molavi, M. Rezakazemi, S. Tajahmadi, A. Bahi, F. Ko, T. M. Aminabhavi, J.-R. Li and M. Arjmand, UiO-66 Metal–Organic Frameworks in Water Treatment: A Critical Review, *Prog. Mater. Sci.*, 2022, **125**, 100904, DOI: 10.1016/j.pmatsci.2021.100904.

26 K. L. Timofeev, S. A. Kulinich and T. S. Kharlamova, NH2-Modified UiO-66: Structural Characteristics and Functional Properties, *Molecules*, 2023, **28**(9), 3916, DOI: 10.3390/molecules28093916.

27 D. Sun, Y. Fu, W. Liu, L. Ye, D. Wang, L. Yang, X. Fu and Z. Li, Studies on Photocatalytic CO2 Reduction over NH 2-Uio-66(Zr) and Its Derivatives: Towards a Better Understanding of Photocatalysis on Metal-Organic Frameworks, *Chem.—Eur. J.*, 2013, **19**(42), 14279–14285, DOI: 10.1002/chem.201301728.

28 C. L. Luu, T. T. Van Nguyen, T. Nguyen and T. C. Hoang, Synthesis, Characterization and Adsorption Ability of UiO-66-NH2, *Adv. Nat. Sci. Nanosci. Nanotechnol.*, 2015, **6**(2), 025004, DOI: 10.1088/2043-6262/6/2/025004.

29 K. Ahmad, M. A. Nazir, A. K. Qureshi, E. Hussain, T. Najam, M. S. Javed, S. S. A. Shah, M. K. Tufail, S. Hussain, N. A. Khan, H. ur R. Shah and M. Ashfaq, Engineering of Zirconium Based Metal-Organic Frameworks (Zr-MOFs) as

Efficient Adsorbents, *Mater. Sci. Eng., B*, 2020, **262**, 114766, DOI: 10.1016/j.mseb.2020.114766.

30 G. W. Peterson, J. B. Decoste, F. Fatollahi-Fard and D. K. Britt, Engineering UiO-66-NH2 for Toxic Gas Removal, *Ind. Eng. Chem. Res.*, 2014, **53**(2), 701–707, DOI: 10.1021/ie403366d.

31 Y.-H. Fan, S.-W. Zhang, S.-B. Qin, X.-S. Li and S.-H. Qi, An Enhanced Adsorption of Organic Dyes onto NH2 Functionalization Titanium-Based Metal-Organic Frameworks and the Mechanism Investigation, *Microporous Mesoporous Mater.*, 2018, **263**, 120–127, DOI: 10.1016/j.micromeso.2017.12.016.

32 C.-C. Wang, X.-D. Du, J. Li, X.-X. Guo, P. Wang and J. Zhang, Photocatalytic Cr(VI) Reduction in Metal-Organic Frameworks: A Mini-Review, *Appl. Catal., B*, 2016, **193**, 198–216, DOI: 10.1016/j.apcatb.2016.04.030.

33 K. Wang, J. Gu and N. Yin, Efficient Removal of Pb(II) and Cd(II) Using NH2-Functionalized Zr-MOFs via Rapid Microwave-Promoted Synthesis, *Ind. Eng. Chem. Res.*, 2017, **56**(7), 1880–1887, DOI: 10.1021/acs.iecr.6b04997.

34 S. Yang, J. Yu, G. Lu, G. Song, G. Shi, Y. Wang, X. Xie, H. Yuan, X. Ren and J. Sun, Effect of NH2-Functionalization of MIL-125 on Photocatalytic Degradation of o-Xylene and Acetaldehyde, *Chem. Eng. J.*, 2024, **498**, 155251, DOI: 10.1016/j.cej.2024.155251.

35 J. Long, S. Wang, Z. Ding, S. Wang, Y. Zhou, L. Huang and X. Wang, Amine-Functionalized Zirconium Metal–Organic Framework as Efficient Visible-Light Photocatalyst for Aerobic Organic Transformations, *Chem. Commun.*, 2012, **48**(95), 11656–11658, DOI: 10.1039/C2CC34620F.

36 H. N. Rubin and M. M. Reynolds, Functionalization of Metal–Organic Frameworks To Achieve Controllable Wettability, *Inorg. Chem.*, 2017, **56**(9), 5266–5274, DOI: 10.1021/acs.inorgchem.7b00373.

37 Q. Zha, X. Sang, D. Liu, D. Wang, G. Shi and C. Ni, Modification of Hydrophilic Amine-Functionalized Metal-Organic Frameworks to Hydrophobic for Dye Adsorption, *J. Solid State Chem.*, 2019, **275**, 23–29, DOI: 10.1016/j.jssc.2019.04.001.

38 D. V. Mousavi, S. Ahmadipouya, A. Shokrgozar, H. Molavi, M. Rezakazemi, F. Ahmadijokani and M. Arjmand, Adsorption Performance of UiO-66 towards Organic Dyes: Effect of Activation Conditions, *J. Mol. Liq.*, 2021, **321**, 114487, DOI: 10.1016/j.molliq.2020.114487.

39 Y. Tan, W. Zhang, Y. Gao, J. Wu and B. Tang, Facile Synthesis and Supercapacitive Properties of Zr-Metal Organic Frameworks (UiO-66), *RSC Adv.*, 2015, **5**(23), 17601–17605, DOI: 10.1039/C4RA11896K.

40 M. J. Katz, Z. J. Brown, Y. J. Colón, P. W. Siu, K. A. Scheidt, R. Q. Snurr, J. T. Hupp and O. K. Farha, A Facile Synthesis of UiO-66, UiO-67 and Their Derivatives, *Chem. Commun.*, 2013, **49**(82), 9449–9451, DOI: 10.1039/c3cc46105j.

41 L. Shen, R. Liang, M. Luo, F. Jing and L. Wu, Electronic Effects of Ligand Substitution on Metal–Organic Framework Photocatalysts: The Case Study of UiO-66, *Phys. Chem. Chem. Phys.*, 2015, **17**(1), 117–121, DOI: 10.1039/C4CP04162C.

42 B. Zhang, J. Zhang, C. Liu, X. Sang, L. Peng, X. Ma, T. Wu, B. Han and G. Yang, Solvent Determines the Formation and Properties of Metal-Organic Frameworks, *RSC Adv.*, 2015, **5**(47), 37691–37696, DOI: 10.1039/c5ra02440d.

43 G. Demazeau, Solvothermal Processes: Definition, Key Factors Governing the Involved Chemical Reactions and New Trends, *Z. Naturforsch. B*, 2010, **65**(8), 999–1006.

44 W. Zhang, G. Lu, C. Cui, Y. Liu, S. Li, W. Yan, C. Xing, Y. R. Chi, Y. Yang and F. Huo, A Family of Metal-Organic Frameworks Exhibiting Size-Selective Catalysis with Encapsulated Noble-Metal Nanoparticles, *Adv. Mater.*, 2014, **26**(24), 4056–4060, DOI: 10.1002/adma.201400620.

45 Z. U. Zango, N. S. Sambudi, K. Jumbri, N. H. H. Abu Bakar, N. A. F. Abdullah, E. S. M. Negim and B. Saad, Experimental and Molecular Docking Model Studies for the Adsorption of Polycyclic Aromatic Hydrocarbons onto UiO-66(Zr) and NH2-UiO-66(Zr) Metal-Organic Frameworks, *Chem. Eng. Sci.*, 2020, **220**, 115608, DOI: 10.1016/j.ces.2020.115608.

46 N. Priyadarshini, K. Kumar Das, S. Mansingh and K. Parida, Facile Fabrication of Functionalised Zr Co-Ordinated MOF: Antibiotic Adsorption and Insightful Physiochemical Characterization, *Results Chem.*, 2022, **4**, 100450, DOI: 10.1016/j.rechem.2022.100450.

47 G. Lv, J. Liu, Z. Xiong, Z. Zhang and Z. Guan, Selectivity Adsorptive Mechanism of Different Nitrophenols on UIO-66 and UIO-66-NH2in Aqueous Solution, *J. Chem. Eng. Data*, 2016, **61**(11), 3868–3876, DOI: 10.1021/acs.jced.6b00581.

48 L. Rahmidar, D. Gustaman Syarif and N. Suyatman, A Facile Approach for Preparing Zr-BDC and Zr-BDC-NH2MOFs Using Solvothermal Method, *J. Phys.: Conf. Ser.*, 2022, **2243**(1), 012055, DOI: 10.1088/1742-6596/2243/1/012055.

49 L. Shen, W. Wu, R. Liang, R. Lin and L. Wu, Highly Dispersed Palladium Nanoparticles Anchored on UiO-66(NH2) Metal-Organic Framework as a Reusable and Dual Functional Visible-Light-Driven Photocatalyst, *Nanoscale*, 2013, **5**(19), 9374–9382, DOI: 10.1039/c3nr03153e.

50 X. Zhang, S. Zhang, G. Ouyang and R. Han, Removal of Cr(VI) from Solution Using UiO-66-NH2 Prepared in a Green Way, *Korean J. Chem. Eng.*, 2022, **39**(7), 1839–1849, DOI: 10.1007/s11814-021-1015-x.

51 M. Taddei, D. A. Steitz, J. A. Van Bokhoven and M. Ranocchiari, Continuous-Flow Microwave Synthesis of Metal-Organic Frameworks: A Highly Efficient Method for Large-Scale Production, *Chem.—Eur. J.*, 2016, **22**(10), 3245–3249, DOI: 10.1002/chem.201505139.

52 V. Polshettiwar, M. N. Nadagouda and R. S. Varma, Microwave-Assisted Chemistry: A Rapid and Sustainable Route to Synthesis of Organics and Nanomaterials, *Aust. J. Chem.*, 2009, **62**(1), 16–26, DOI: 10.1071/CH08404.

53 A. Huang, L. Wan and J. Caro, Microwave-Assisted Synthesis of Well-Shaped UiO-66-NH2 with High CO2 Adsorption Capacity, *Mater. Res. Bull.*, 2018, **98**, 308–313, DOI: 10.1016/j.materresbull.2017.10.038.

54 R. R. Solís, M. Peñas-Garzón, C. Belver, J. J. Rodriguez and J. Bedia, Highly Stable UiO-66-NH2 by the Microwave-

Assisted Synthesis for Solar Photocatalytic Water Treatment, *J. Environ. Chem. Eng.*, 2022, **10**(2), 107122, DOI: **10.1016/j.jece.2021.107122**.

55 A. Kazemi, F. Moghadaskhou, M. A. Pordsari, F. Manteghi, A. Tadjarodi and A. Ghaemi, Enhanced CO2 Capture Potential of UiO-66-NH2 Synthesized by Sonochemical Method: Experimental Findings and Performance Evaluation, *Sci. Rep.*, 2023, **13**(1), 19891, DOI: **10.1038/s41598-023-47221-6**.

56 L. Zhang, F. Liand and L. Luo, *IOP Conf. Ser.: Earth Environ. Sci.*, 2017, **108**, 042104, DOI: **10.1088/1755-1315/108/4/042104**.

57 M. Kubo, Y. Miyoshi, Y. Uchitomi and M. Shimada, Insights into the Spray Synthesis of UiO-66 and UiO-66-NH2 Metal–Organic Frameworks: Effect of Zirconium Precursors and Process Parameters, *Crystals*, 2024, **14**(2), 116, DOI: **10.3390/cryst14020116**.

58 S. L. James, C. J. Adams, C. Bolm, D. Braga, P. Collier, T. Friščić, F. Grepioni, K. D. M. Harris, G. Hyett, W. Jones, A. Krebs, J. Mack, L. Maini, A. G. Orpen, I. P. Parkin, W. C. Shearouse, J. W. Steed and D. C. Waddell, Mechanochemistry: Opportunities for New and Cleaner Synthesis, *Chem. Soc. Rev.*, 2012, **41**(1), 413–447, DOI: **10.1039/C1CS15171A**.

59 D. Chen, J. Zhao, P. Zhang and S. Dai, Mechanochemical Synthesis of Metal–Organic Frameworks, *Polyhedron*, 2019, **162**, 59–64, DOI: **10.1016/j.poly.2019.01.024**.

60 K. Užarević, T. C. Wang, S. Y. Moon, A. M. Fidelli, J. T. Hupp, O. K. Farha and T. Friščić, Mechanochemical and Solvent-Free Assembly of Zirconium-Based Metal-Organic Frameworks, *Chem. Commun.*, 2016, **52**(10), 2133–2136, DOI: **10.1039/c5cc08972g**.

61 P. M. Bhanderi, A. K. Vyas, D. K. Katariya and R. C. Khunt, Facile Sonochemical Synthesis and Characterization of Amino Acid-Based Metal-Organic Frameworks for Enhanced Dye Adsorption, *J. Mol. Struct.*, 2025, **1326**, 141058, DOI: **10.1016/j.molstruc.2024.141058**.

62 A. S. Eliwa, M. A. Hefnawy, S. S. Medany, R. G. Deghadi, W. M. Hosny and G. G. Mohamed, Ultrasonic-Assisted Synthesis of Nickel Metal-Organic Framework for Efficient Urea Removal and Water Splitting Applications, *Synth. Met.*, 2023, **294**, 117309, DOI: **10.1016/j.synthmet.2023.117309**.

63 J. D. Xiao, Q. Shang, Y. Xiong, Q. Zhang, Y. Luo, S. H. Yu and H. L. Jiang, Boosting Photocatalytic Hydrogen Production of a Metal–Organic Framework Decorated with Platinum Nanoparticles: The Platinum Location Matters, *Angew. Chem., Int. Ed.*, 2016, **55**(32), 9389–9393, DOI: **10.1002/anie.201603990**.

64 S. Dash, S. P. Tripathy, S. Subudhi, L. Acharya, A. Ray, P. Behera and K. Parida, Ag/Pd Bimetallic Nanoparticle-Loaded Zr-MOF: An Efficacious Visible-Light-Responsive Photocatalyst for H2O2 and H2 Production, *Energy Adv.*, 2024, **3**(5), 1073–1086, DOI: **10.1039/d3ya00597f**.

65 J. Zhang, T. Bai, H. Huang, M. H. Yu, X. Fan, Z. Chang and X. H. Bu, Metal–Organic-Framework-Based Photocatalysts Optimized by Spatially Separated Cocatalysts for Overall Water Splitting, *Adv. Mater.*, 2020, **32**(49), 2004747, DOI: **10.1002/adma.202004747**.

66 X. Ma, L. Wang, Q. Zhang and H. L. Jiang, Switching on the Photocatalysis of Metal–Organic Frameworks by Engineering Structural Defects, *Angew. Chem., Int. Ed.*, 2019, **58**(35), 12175–12179, DOI: **10.1002/anie.201907074**.

67 X. Hou, L. Wu, L. Gu, G. Xu, H. Du and Y. Yuan, Maximizing the Photocatalytic Hydrogen Evolution of Z-Scheme UiO-66-NH 2 @Au@CdS by Aminated-Functionalized Linkers, *J. Mater. Sci.: Mater. Electron.*, 2019, **30**(5), 5203–5211, DOI: **10.1007/s10854-019-00819-x**.

68 S. Sk, R. Madhu, D. S. Gavali, V. Bhasin, R. Thapa, S. N. Jha, D. Bhattacharyya, S. Kundu and U. Pal, An Ultrathin 2D NiCo-LDH Nanosheet Decorated NH2-UiO-66 MOF-Nanocomposite with Exceptional Chemical Stability for Electrocatalytic Water Splitting, *J. Mater. Chem. A*, 2023, 10309–10318, DOI: **10.1039/d3ta00836c**.

69 S. Subudhi and K. Parida, Zr-Based MOF: An Enhanced Photocatalytic Application towards H2evolution by Consequence of Functional Group and LSPR Effect, *Mater. Today: Proc.*, 2021, **35**, 198–202, DOI: **10.1016/j.matpr.2020.04.252**.

70 S. Prakash Tripathy, S. Subudhi, S. Das, M. Kumar Ghosh, M. Das, R. Acharya, R. Acharya and K. Parida, Hydrolytically Stable Citrate Capped Fe3O4@UiO-66-NH2 MOF: A Hetero-Structure Composite with Enhanced Activity towards Cr (VI) Adsorption and Photocatalytic H2 Evolution, *J. Colloid Interface Sci.*, 2022, **606**, 353–366, DOI: **10.1016/j.jcis.2021.08.031**.

71 S. Subudhi, G. Swain, S. P. Tripathy and K. Parida, UiO-66-NH2Metal-Organic Frameworks with Embedded MoS2Nanoflakes for Visible-Light-Mediated H2and O2Evolution, *Inorg. Chem.*, 2020, **59**(14), 9824–9837, DOI: **10.1021/acs.inorgchem.0c01030**.

72 Z. Qian, R. Zhang, H. Hu, Y. Xiao, H. Li, X. Sun and T. Ma, Decoration of Defective Sites in Metal–Organic Frameworks to Construct Tight Heterojunction Photocatalyst for Hydrogen Production, *Sol. RRL*, 2023, **7**(22), 2300547, DOI: **10.1002/solr.202300547**.

73 Y. Su, Z. Zhang, H. Liu and Y. Wang, Cd0.2Zn0.8S@UiO-66-NH2 Nanocomposites as Efficient and Stable Visible-Light-Driven Photocatalyst for H2 Evolution and CO2 Reduction, *Appl. Catal., B*, 2017, **200**, 448–457, DOI: **10.1016/j.apcatb.2016.07.032**.

74 S. Subudhi, L. Paramanik, S. Sultana, S. Mansingh, P. Mohapatra and K. Parida, A Type-II Interband Alignment Heterojunction Architecture of Cobalt Titanate Integrated UiO-66-NH2: A Visible Light Mediated Photocatalytic Approach Directed towards Norfloxacin Degradation and Green Energy (Hydrogen) Evolution, *J. Colloid Interface Sci.*, 2020, **568**, 89–105, DOI: **10.1016/j.jcis.2020.02.043**.

75 L. Biswal, S. P. Tripathy, S. Dash, S. Das, S. Subudhi and K. Parida, Aggrandized Photocatalytic H2O2 and H2 Production by a TiO2/Ti3C2-TiC/Mixed Metal Ce-Zr MOF Composite: An Interfacial Engineered Solid-State-

Mediator-Based Z-Scheme Heterostructure, *Adv. Mater.*, 2024, **5**(10), 4452–4466, DOI: **10.1039/d3ma01176c**.

76 X. Wang, Y. Wang, G. chai, G. Yang, C. Wang and W. Yan, Poly (Triphenylamine)-Decorated UIO-66-NH2 Mesoporous Architectures with Enhanced Photocatalytic Activity for CO2 Reduction and H2 Evolution, *J. CO_2 Util.*, 2021, **51**, 101654, DOI: **10.1016/j.jcou.2021.101654**.

77 G. Swain, S. Sultana and K. Parida, One-Pot-Architectured Au-Nanodot-Promoted MoS2/ZnIn2S4: A Novel p–n Heterojunction Photocatalyst for Enhanced Hydrogen Production and Phenol Degradation, *Inorg. Chem.*, 2019, **58**(15), 9941–9955, DOI: **10.1021/acs.inorgchem.9b01105**.

78 J. Wang, Z. Sun, X. Jiang, Q. Yuan, D. Dong, P. Zhang and Z. Zhang, Uniform Decoration of UiO-66-NH2nanooctahedra on TiO2electrospun Nanofibers for Enhancing Photocatalytic H2production Based on Multi-Step Interfacial Charge Transfer, *Dalton Trans.*, 2021, **50**(18), 6152–6160, DOI: **10.1039/d1dt00743b**.

79 C. Zhao, Y. Zhang, H. Jiang, J. Chen, Y. Liu, Q. Liang, M. Zhou, Z. Li and Y. Zhou, Combined Effects of Octahedron NH2-UiO-66 and Flowerlike ZnIn2S4 Microspheres for Photocatalytic Dye Degradation and Hydrogen Evolution under Visible Light, *J. Phys. Chem. C*, 2019, **123**(29), 18037–18049, DOI: **10.1021/acs.jpcc.9b03807**.

80 M.-J. Choi and D.-H. Cho, Research Activities on the Utilization of Carbon Dioxide in Korea, *Clean*, 2008, **36**(5–6), 426–432, DOI: **10.1002/clen.200700176**.

81 J. E. T. Houghton, Y. Ding, D. Griggs, M. Noguer, P. van der Linden, X. Dai, M. Maskell and C. Johnson, Climate Change 2001: The Scientific Basis, in *Contribution of Working Group I to the Third Assessment Report of the Intergovernmental Panel on Climate Change (IPCC)*, 2001, vol. 881, p. 881.

82 H. Khatib, IEA World Energy Outlook 2011—A Comment, *Energy Policy*, 2012, **48**, 737–743, DOI: **10.1016/j.enpol.2012.06.007**.

83 A. Crake, K. C. Christoforidis, A. Gregg, B. Moss, A. Kafizas and C. Petit, The Effect of Materials Architecture in TiO 2/MOF Composites on CO 2 Photoreduction and Charge Transfer, *Small*, 2019, **15**(11), 1805473, DOI: **10.1002/smll.201805473**.

84 K. A. Adegoke, K. G. Akpomie, E. S. Okeke, C. Olisah, A. Malloum, N. W. Maxakato, J. O. Ighalo, J. Conradie, C. R. Ohoro, J. F. Amaku and K. O. Oyedotun, UiO-66-Based Metal-Organic Frameworks for CO2 Catalytic Conversion, Adsorption and Separation, *Sep. Purif. Technol.*, 2024, **331**, 125456, DOI: **10.1016/j.seppur.2023.125456**.

85 X. Wang, Y. Su, G. Yang, G. Chai, Z. Xu, M. S. Nasir, X. Zheng, C. Wang and W. Yan, Synthesis of Au/UiO-66-NH2/Graphene Composites as Efficient Visible-Light Photocatalysts to Convert CO2, *Int. J. Hydrogen Energy*, 2021, **46**(21), 11621–11635, DOI: **10.1016/j.ijhydene.2021.01.024**.

86 G. Wang, C. T. He, R. Huang, J. Mao, D. Wang and Y. Li, Photoinduction of Cu Single Atoms Decorated on UiO-66-NH2for Enhanced Photocatalytic Reduction of CO2to Liquid Fuels, *J. Am. Chem. Soc.*, 2020, **142**(45), 19339–19345, DOI: **10.1021/jacs.0c09599**.

87 X. Zhao, L. Sun, X. Jin, M. Xu, S. Yin, J. Li, X. Li, D. Shen, Y. Yan and P. Huo, Cu Media Constructed Z-Scheme Heterojunction of UiO-66-NH2/Cu2O/Cu for Enhanced Photocatalytic Induction of CO2, *Appl. Surf. Sci.*, 2021, **545**, 148967, DOI: **10.1016/j.apsusc.2021.148967**.

88 P. Zhu, H. Cao, H. Yang, M. Geng, S. Qin, L. Tan, X. Gao and C. Wang, One-Pot Synthesis of Ni(II)-Doped UiO-66-NH2 for Enhanced Photocatalytic CO2 Reduction to CO with Efficient Charge Transfer, *Appl. Surf. Sci.*, 2024, **652**, 159348, DOI: **10.1016/j.apsusc.2024.159348**.

89 J. Meng, Q. Chen, J. Lu and H. Liu, Z-Scheme Photocatalytic CO 2 Reduction on a Heterostructure of Oxygen-Defective ZnO/Reduced Graphene Oxide/UiO-66-NH 2 under Visible Light, *ACS Appl. Mater. Interfaces*, 2019, **11**(1), 550–562, DOI: **10.1021/acsami.8b14282**.

90 Y. Wang, L. Guo, Y. Zeng, H. Guo, S. Wan, M. Ou, S. Zhang and Q. Zhong, Amino-Assisted NH2-UiO-66 Anchored on Porous g-C3N4 for Enhanced Visible-Light-Driven CO2 Reduction, *ACS Appl. Mater. Interfaces*, 2019, **11**(34), 30673–30681, DOI: **10.1021/acsami.9b04302**.

91 S. Wan, M. Ou, Q. Zhong and X. Wang, Perovskite-Type CsPbBr3 Quantum Dots/UiO-66(NH2) Nanojunction as Efficient Visible-Light-Driven Photocatalyst for CO2 Reduction, *Chem. Eng. J.*, 2019, **358**, 1287–1295, DOI: **10.1016/j.cej.2018.10.120**.

92 Y. Cao, H. Zhang, F. Song, T. Huang, J. Ji, Q. Zhong, W. Chu and Q. Xu, UiO-66-NH2/GO Composite: Synthesis, Characterization and CO2 Adsorption Performance, *Materials*, 2018, **11**(4), 589, DOI: **10.3390/ma11040589**.

93 A. Crake, K. C. Christoforidis, A. Kafizas, S. Zafeiratos and C. Petit, CO2 Capture and Photocatalytic Reduction Using Bifunctional TiO2/MOF Nanocomposites under UV–Vis Irradiation, *Appl. Catal., B*, 2017, **210**, 131–140, DOI: **10.1016/j.apcatb.2017.03.039**.

94 X. Li, C. Fang, L. Huang and J. Yu, Enhanced Carbon Dioxide Adsorption and Carrier Separation over Amine Functionalized Zirconium Metal Organic Framework/Gold/Indium Oxide for Boosting Photocatalytic Carbon Dioxide Reduction, *J. Colloid Interface Sci.*, 2024, **655**, 485–492, DOI: **10.1016/j.jcis.2023.11.028**.

95 P. X. Li, X. Y. Yan, X. M. Song, J. J. Li, B. H. Ren, S. Y. Gao and R. Cao, Zirconium-Based Metal-Organic Framework Particle Films for Visible-Light-Driven Efficient Photoreduction of CO2, *ACS Sustain. Chem. Eng.*, 2021, **9**(5), 2319–2325, DOI: **10.1021/acssuschemeng.0c08559**.

96 W. Zhang, L. Wang and J. Zhang, Preparation of Ag/UiO-66-NH2 and Its Application in Photocatalytic Reduction of Cr(VI) under Visible Light, *Res. Chem. Intermed.*, 2019, **45**(10), 4801–4811, DOI: **10.1007/s11164-019-03865-6**.

97 Z. Zhang, S. Wang, M. Bao, J. Ren, S. Pei, S. Yu and J. Ke, Construction of Ternary Ag/AgCl/NH2-UiO-66 Hybridized Heterojunction for Effective Photocatalytic Hexavalent Chromium Reduction, *J. Colloid Interface Sci.*, 2019, **555**, 342–351, DOI: **10.1016/j.jcis.2019.07.103**.

98 N. Khosroshahi, M. D. Goudarzi, M. E. Gilvan and V. Safarifard, Collocation of MnFe2O4 and UiO-66-NH2: An Efficient and Reusable Nanocatalyst for Achieving High-Performance in Hexavalent Chromium Reduction, *J. Mol. Struct.*, 2022, **1263**, 132994, DOI: 10.1016/j.molstruc.2022.132994.

99 M. B. Hussain, R. Mehmood, U. Azhar, J. Wang and L. Song, BiOCl-Coated UiO-66-NH2Metal-Organic Framework Nanoparticles for Visible-Light Photocatalytic Cr(VI) Reduction, *ACS Appl. Nano Mater.*, 2021, **4**(4), 4037–4047, DOI: 10.1021/acsanm.1c00380.

100 H. He, X. Wang, Q. Yu, W. Wu, X. Feng, D. Kong, X. Ren and J. Gao, In Situ Growth of Ti3C2/UiO-66-NH2 Composites for Photoreduction of Cr(VI), *Catalysts*, 2023, **13**(5), 876, DOI: 10.3390/catal13050876.

101 C. Xu, M. Bao, J. Ren and Z. Zhang, NH2-MIL-88B (FeαIn1−α) Mixed-MOFs Designed for Enhancing Photocatalytic Cr(vi) Reduction and Tetracycline Elimination, *RSC Adv.*, 2020, **10**(64), 39080–39086, DOI: 10.1039/D0RA07487J.

102 Y. Gao, Y. Huang, M. Bao, X. Zhang, X. Zhou, L. Liu, Z. Zhang, L. Zeng and J. Ke, Ti-Doped Zr-UiO-66-NH2 Boosting Charge Transfer for Enhancing the Synergistic Removal of Cr (VI) and TC-HCl in Wastewater, *Process Saf. Environ. Prot.*, 2023, **172**, 857–868, DOI: 10.1016/j.psep.2023.02.090.

103 J. Ren, S. Lv, S. Wang, M. Bao, X. Zhang, Y. Gao, Y. Liu, Z. Zhang, L. Zeng and J. Ke, Construction of Efficient G-C3N4/NH2-UiO-66 (Zr) Heterojunction Photocatalysts for Wastewater Purification, *Sep. Purif. Technol.*, 2021, **274**, 118973, DOI: 10.1016/j.seppur.2021.118973.

104 K. Yuan, B. Gong, C. Peng, Y. Feng, Y. Hu, K. Chen, D. Chen and D. Hao, Porphyrin Modified UiO-66-NH2 for Highly Efficient Photoreduction of Cr(VI) under Visible Light, *Catalysts*, 2023, **13**(7), 1073, DOI: 10.3390/catal13071073.

105 S. Zheng, H. Du, L. Yang, M. Tan, N. Li, Y. Fu, D. Hao and Q. Wang, PDINH Bridged NH2-UiO-66(Zr) Z-Scheme Heterojunction for Promoted Photocatalytic Cr(VI) Reduction and Antibacterial Activity, *J. Hazard. Mater.*, 2023, **447**, 130849, DOI: 10.1016/j.jhazmat.2023.130849.

106 R. Al-Tohamy, S. S. Ali, F. Li, K. M. Okasha, Y. A.-G. Mahmoud, T. Elsamahy, H. Jiao, Y. Fu and J. Sun, A Critical Review on the Treatment of Dye-Containing Wastewater: Ecotoxicological and Health Concerns of Textile Dyes and Possible Remediation Approaches for Environmental Safety, *Ecotoxicol. Environ. Saf.*, 2022, **231**, 113160, DOI: 10.1016/j.ecoenv.2021.113160.

107 Q. Chen, Q. He, M. Lv, Y. Xu, H. Yang, X. Liu and F. Wei, Selective Adsorption of Cationic Dyes by UiO-66-NH 2, *Appl. Surf. Sci.*, 2015, **327**, 77–85, DOI: 10.1016/j.apsusc.2014.11.103.

108 L. L. Zhang, M. Liu, K. A. Wang and H. B. Zhu, Assembling Ag/UiO-66-NH2 Composites for Photocatalytic Dye Degradation, *J. Inorg. Organomet. Polym. Mater.*, 2022, **32**(5), 1896–1901, DOI: 10.1007/s10904-022-02232-0.

109 L. Wang, P. Zheng, X. Zhou, M. Xu and X. Liu, Facile Fabrication of CdS/UiO-66-NH 2 Heterojunction Photocatalysts for Efficient and Stable Photodegradation of Pollution, *J. Photochem. Photobiol., A*, 2019, **376**, 80–87, DOI: 10.1016/j.jphotochem.2019.03.001.

110 Q. Liang, S. Cui, J. Jin, C. Liu, S. Xu, C. Yao and Z. Li, Fabrication of BiOI@UIO-66(NH2)@g-C3N4 Ternary Z-Scheme Heterojunction with Enhanced Visible-Light Photocatalytic Activity, *Appl. Surf. Sci.*, 2018, **456**, 899–907, DOI: 10.1016/j.apsusc.2018.06.173.

111 M. S. Hosseini, A. Abbasi and M. Masteri-Farahani, Decoration of NH2-UiO-66 with FeOOH Quantum Dots for Improving Photo-Degradation of Organic Dyes upon Visible Light Irradiation, *Appl. Surf. Sci.*, 2022, **604**, 154514, DOI: 10.1016/j.apsusc.2022.154514.

112 D. Teng, J. Zhang, X. Luo, F. Jing, H. Wang, J. Chen, C. Yang, S. Zang and Y. Zhou, Remarkably Enhanced Photodegradation of Organic Pollutants by NH2-UiO-66/ZnO Composite under Visible-Light Irradiation, *J. Renew. Mater.*, 2022, **10**(5), 2378–2391, DOI: 10.32604/JRM.2022.019209.

113 J. Yoo, J. Lee and J. Kim, A Floating Photocatalytic Fabric Integrated with a AgI/UiO-66-NH2 Heterojunction as a Facile Strategy for Wastewater Treatment, *RSC Adv.*, 2024, **14**(3), 1794–1802, DOI: 10.1039/d3ra07534f.

114 Z. Xia, L. Wang, W. Tan, L. Yuan, X. He, J. Wang, L. Chen, S. Zeng, S. Lu and Z. Jiao, Boosting Visible-Light Photocatalytic Degradation Efficiency of Tetracycline and Rhodamine B Using Double Z-Shaped Heterojunction Catalyst of UiO-66-NH2/BiOCl/Bi2S3, https://ssrn.com/abstract=4789591.

115 M. Khajeh, A. R. Oveisi, A. Barkhordar and Z. Sorinezami, Co-Fe-Layered Double Hydroxide Decorated Amino-Functionalized Zirconium Terephthalate Metal-Organic Framework for Removal of Organic Dyes from Water Samples, *Spectrochim. Acta, Part A*, 2020, **234**, 118270, DOI: 10.1016/j.saa.2020.118270.

116 Y. Pan, X. Yuan, L. Jiang, H. Wang, H. Yu and J. Zhang, Stable Self-Assembly AgI/UiO-66(NH2) Heterojunction as Efficient Visible-Light Responsive Photocatalyst for Tetracycline Degradation and Mechanism Insight, *Chem. Eng. J.*, 2020, **384**, 123310, DOI: 10.1016/j.cej.2019.123310.

117 S. Jing, H. Wang, A. Wang, R. Cheng, H. Liang, F. Chen, A. Brouzgou and P. Tsiakaras, Surface Plasmon Resonance Bismuth-Modified NH2-UiO-66 with Enhanced Photocatalytic Tetracycline Degradation Performance, *J. Colloid Interface Sci.*, 2024, **655**, 120–132, DOI: 10.1016/j.jcis.2023.10.149.

118 T. K. Vo, M. T. Nguyen, V. C. Nguyen and J. Kim, Microwave-Assisted Synthesis of MgFe2O4-Decorated UiO-66(Zr)-NH2 Composites for Collaborative Adsorption and Photocatalytic Degradation of Tetracycline, *Korean J. Chem. Eng.*, 2022, **39**(9), 2532–2541, DOI: 10.1007/s11814-022-1131-2.

119 M. Ghorbani, A. R. Solaimany Nazar, M. Frahadian and S. Tangestaninejad, Fabrication of Novel ZnO@BiOBr/UiO-66-NH2 Core-Shell Heterojunction for Improved Tetracycline Degradation, *Appl. Surf. Sci.*, 2023, **612**, 155819, DOI: 10.1016/j.apsusc.2022.155819.

120 Q. Hu, T. Zhou, Z. Wang, Y. Liu, M. Ye, H. Zhang, X. Zhu, J. Yi and Y. Xu, Decoration of Bi2MoO6 Nanosheets with NH2-UiO-66 for Boosting Visible-Light Photocatalytic Activities, *Inorg. Chim. Acta*, 2024, **565**, 121979, DOI: **10.1016/j.ica.2024.121979**.

121 B. Jeyhoon and V. Safarifard, Stable Core-Shell UiO-66-NH2@Zeolitic Imidazolate Frameworks Composite as a Favorable Photocatalyst for Tetracycline Degradation, *ChemistrySelect*, 2024, **9**(3), e202304515, DOI: **10.1002/slct.202304515**.

122 Q. Wang, S. Zheng, W. Ma, J. Qian, L. Huang, H. Deng, Q. Zhou, S. Zheng, S. Li, H. Du, Q. Li, D. Hao and G. Yang, Facile Synthesis of Direct Z-Scheme PPy/NH2-UiO-66 Heterojunction for Enhanced Photocatalytic Cr(VI) Reduction, Industrial Electroplating Wastewater Treatment, and Tetracycline Degradation, *Appl. Catal., B*, 2024, **344**, 123669, DOI: **10.1016/j.apcatb.2023.123669**.

123 R. Bariki, S. K. Pradhan, S. Panda, S. K. Nayak, A. R. Pati and B. G. Mishra, Hierarchical UiO-66(-NH2)/CuInS2S-Scheme Photocatalyst with Controlled Topology for Enhanced Photocatalytic N2Fixation and H2O2Production, *Langmuir*, 2023, **39**(22), 7707–7722, DOI: **10.1021/acs.langmuir.3c00519**.

